Workability optimisation of the Stella Synergy

during monopile installation with a motion-compensated gripper and using its DP-system

J. Verbruggen

Thesis report

TU Delft Delft University of Technology

Delft Center for Offshore and Dredging

Workability optimisation of the Stella Synergy

during monopile installation with a motion-compensated gripper and using its DP-system

Thesis report

J. Verbruggen

14-7-2021

Faculty of Mechanical, Maritime and Materials Engineering (3mE) · Delft University of Technology

The work in this thesis is supported by Jumbo Maritime. Their cooperation is hereby gratefully acknowledged.

Abstract

It is essential to shift to a decarbonised energy supply by producing renewable energy on a large scale to stop climate change. Wind energy is one of the most promising renewable energy sources, and most wind turbines use a monopile as support structure. Using a floating vessel operating on its Dynamic Positioning (DP)-system and using a motion-compensated pile gripper to install monopiles could be the installation method of the future. Therefore, this thesis focuses on this method. Jumbo Maritime is currently building the Stella Synergy, a heavy lift vessel capable of installing monopile using this new method. The company is interested in the capability and workability of the vessel during such an installation operation. The main objective of this thesis project is to build a model that accurately describes the motions of the Stella Synergy, the monopile, and the motion-compensated gripper, depending on the environmental conditions.

This model is built in aNySIM, which is a time-domain simulation software program of MARIN based on the Runge-Kutta2 (RK2) numerical method. The model considers the early pile driving phase because this phase is governing in terms of risk. The monopile acts as an inverted pendulum in this phase, and the motion-compensated pile gripper must guarantee the stability of the monopile. No soil-monopile interaction is assumed because the monopile's penetration depth is low, and when the soil stability force is considered, it contains significant uncertainties. The vessel uses its DP-system for station keeping. The DP-system contains a position reference system, a filter, a control system, and a thruster allocation algorithm. Although the DP-gains are optimised for one specific critical sea condition, they are used for each simulated sea condition. The vessel's motion could be reduced by optimising the DP-gains for each simulation, but this is a very time-consuming process that is beyond the scope of this thesis.

The model describes the wind, current and wave forces on the monopile and vessel. The environmental conditions are assumed to be collinear, and wave spreading is added to the model for some simulations. The wave forces on the vessel are determined with diffraction calculations in Ansys AQWA. The diffraction calculation for the vessel is verified with a diffraction calculation of MARIN, and the diffraction calculation for the monopile considers the shielding effect and is verified with a calculation with the Morison equation.

A motion-compensated pile gripper with two Proportional Derivative (PD)-controllers is built in Python. One PD-controller is used to determine the force to compensate the vessel's motion, and the other controller is used to determine the force to keep the monopile vertical. The gripper considers static and dynamic friction forces and a maximum delta force per numeric timestep to model the pressure build-up time of the hydraulic cylinders. The gripper is capable of compensating the vessel's motion for 60% to 95%, depending on the sea condition it is operating in.

After verifying every single element of the model, multiple 3-hours simulations are run to generate results. These simulations, which considers each a different sea condition, are tested by the six limitations of the model. First, the preferable incoming angle of environmental conditions is determined. The workability of the Stella Synergy is calculated operating at the North Sea using this preferable incoming angle of attack. Then, two adaptations to the model are tested to increase the workability. Using fast-rotating thrusters or changing the DP-gains result in the workability of 96.4%. The governing limitation is the pitch motion of the vessel.

It is tested if using mooring lines in combination with the DP-system results in a footprint reduction. It is concluded that adding mooring lines could result in a footprint reduction, but it is crucial to gain insight into the optimal axial stiffness of the mooring lines. The monopile's influence on the vessel's motion is also tested. It is concluded that the vessel's surge, sway, roll and yaw motion increases significantly due to the environmental forces on the monopile, which are passed through the gripper to the vessel. Finally, the workability of the vessel during the worst-case single failure is determined. After improving the DP-gains for particular sea conditions, the workability for the worst-case single failure was 96.0%. The failure results thus in a minor difference in the workability.

Table of Contents

List of Figures

List of Tables

Preface

This thesis research is conducted at Jumbo Maritime to obtain a Master degree in Offshore and Dredging Engineering at the Delft University of Technology (TU Delft). This assignment is a consequence of the need for new technologies to increase the productivity of the installations of wind farms.

Unfortunately, during this research, I could not go to the office of Jumbo Maritime in Schiedam due to the Covid-19 virus. Although the meetings with my daily supervisor Kasper van der Heiden were all online, they helped me enormously during this research. Therefore, my sincerest appreciation goes to Kasper.

I would also thank my supervisor, Pim van der Male, for the inspirational meetings and discussions. Sometimes Pim pushed me to do things outside my comfort zone, which was very valuable.

Furthermore, I would like to thank the chairman of my committee Andre van der Stap for his critical attitude during my progress meetings. Due to his on-point questions, I knew which subjects needed some extra attention.

Chapter 1

Introduction to monopile installation

This chapter gives an introduction to monopile installation. It explains how most monopiles are currently installed and explains why research on this object is needed and interesting. At the end of the chapter, an overview of the following chapters is given.

1-1 Background information

To stop global climate change, the Paris agreement, which is an agreement within the United Nations Framework Convention on Climate Change (UNFCCC), was signed by 196 parties in 2016 [5]. The agreement's primary goal was to keep the global temperature rise below 2 degrees Celsius, preferably 1.5 degrees Celsius, compared to the pre-industrial level. One of the main solutions to this problem is to shift to a decarbonised energy supply by producing large-scale renewable energy, this causes a reduction in fossil fuel use and greenhouse gas emissions [6]. According to [7], the world needs to increase the share of renewable energy production in total energy production from 19% in 2017 to 67% in 2050, mostly through the growth in solar and wind power generation. In this literature review, the focus lies on wind energy, one of the most promising renewable energy sources, and it has been growing since the first wind turbine was installed [8]. Especially the offshore wind farms are promising since space scarcity, visual pollution, and noise disturbance problems arise onshore. Next to that, the wind blows stronger and more consistently at sea than at land [9], [10]. In 2009 the total installed offshore wind capacity in Europe was 2.5 GW, this grew exponentially to 22.4 GW in 2019 [11]. The average offshore wind farm size and number of parks keep on increasing [11]. And yet, this is far from what is needed. If Europe wants to meet the Paris agreements' targets, it should raise the North Sea's installed offshore wind capacity to 150 GW in 2040. In the last three years, the average wind deployment rate was 3.6 GW/year, this should be raised to 7 GW/year for the next 20 years to meet the targets [11].

According to the same report, 63% of the current installed offshore wind turbines uses a monopile as support structure. Monopiles are still the favourite support structure because the production facilities are extensive, they are easy to transport, and frequently there is no need to prepare the sea bed. Alternatives for the monopile are tripod structures, lattice structures, gravity-based structures, and floating structures [12]. Wind turbines, and thereby also monopiles, have been increasing in size enormously in the last years. This is mainly due to reducing the costs per produced GW [13] and the increasing water depths at installation sites. The average rated capacity of turbines installed in 2010 was 3.0 MW, and in 2019 it was 7.8 MW. The average water depth of wind farms under construction in 2014 was 22 m, this was in 2019 already 33 m [11]. Due to the simple tubular design of a monopile, it is possible to build them in enormous sizes. The new 14 MW offshore wind turbine of General Electrics will be 260 meters tall, and the monopile will have a diameter of 10 m [14].

Currently, the majority of the monopiles are installed by jack-up installation vessels [15]. A jack-up vessel sails to the installation site, lowers its legs, and jacks up the entire vessel to provide a stable working platform during the installation. Using this method, the installation of a single monopile takes approximately 19 hours, of which approximately 18% of the installation time is spent on the jacking operation [16]. Although using a jack-up vessel for the installation of monopiles is a proven concept, it might not be the most cost-efficient method.

1-2 Motivation

The current installation costs of offshore wind turbines are approximately 100,000 €/MW, which is 20% of the total construction costs [17]. Because the installation costs contribute a significant amount to the total costs, a reduction in installation costs could lead to an increase in the deployment rate of offshore wind turbines. Decreasing the monopile installation costs and while the monopile size keeps increasing opens the discussion about the best installation method. The current method, in which a jack-up vessel is used, seems not to be able to deal with future challenges. Most existing jack-ups do not have long enough legs for the future water depths and do not have the lifting capacity for the future monopile foundation weights. The soil conditions also become more challenging for jack-ups at the future installation sites, and they might not be able to do the job [15]. Above all, according to [18], many second world war bombs are lying down at the sea bottom of the North Sea, those bombs could damage the legs of jack-ups, and this could be very dangerous for the vessel.

This pays attention to an upcoming alternative, using a floating vessel for the installation activities. This could reduce the installation time because no jacking operation is needed, and the second world war bombs are not so dangerous for a floating vessel. Besides that, a floating installation vessel is independent of soil conditions and water depths, and it has by average more deck space than a jack-up vessel [15]. But, environmental forces that act on a floating vessel will cause motions of the vessel. This brings great challenges in terms of station keeping and motion reduction of the vessel during installation operations. Currently, two methods for station keeping of a floating vessel are known, using mooring lines and using Dynamic Positioning (DP). Even if these methods are used properly, the vessel will have small vessel motions causing a particular footprint. A motion-compensated gripper could be used to counter the small vessel motions, but the gripper has certain limitations in terms of the vessel's footprint, and it has limited excitation force to keep the monopile upright during the installation [19]. Monopile installation using a floating vessel and a motion-compensated gripper seems a promising installation technique. Even a first monopile installation test using this technique is already executed successfully by Subsea7 [20].

In this literature review, research is done on the challenges that arise during the installation of a XXL-monopile using a floating vessel and a motion compensated gripper. The goal is to search for the main challenges and a way to deal with them.

1-3 Overview

Chapter 2 describes the essential elements of the installation process. Here the pile gripper, the different installation phases, the shielding effect, and two station keeping systems will be discussed. Chapter 3 elaborates on the environmental forces that act on the vessel and the monopile during installation. These environmental forces are caused by waves, wind, and current. Chapter 2 and 3 together are the of the literature survey for this thesis project. In Chapter 4 is explained step by step how the model is built and verified. Firstly the vessel, then the monopile, and finally the motion-compensated pile gripper will be discussed. In figure 1-1 the Stella Synergy is shown, which is the vessel that is considered in this research. After building and verifying the model, simulations are run, and results are generated, which is shown in Chapter 5. Last but not least, Chapter 6 describes the conclusions and recommendations of this thesis project.

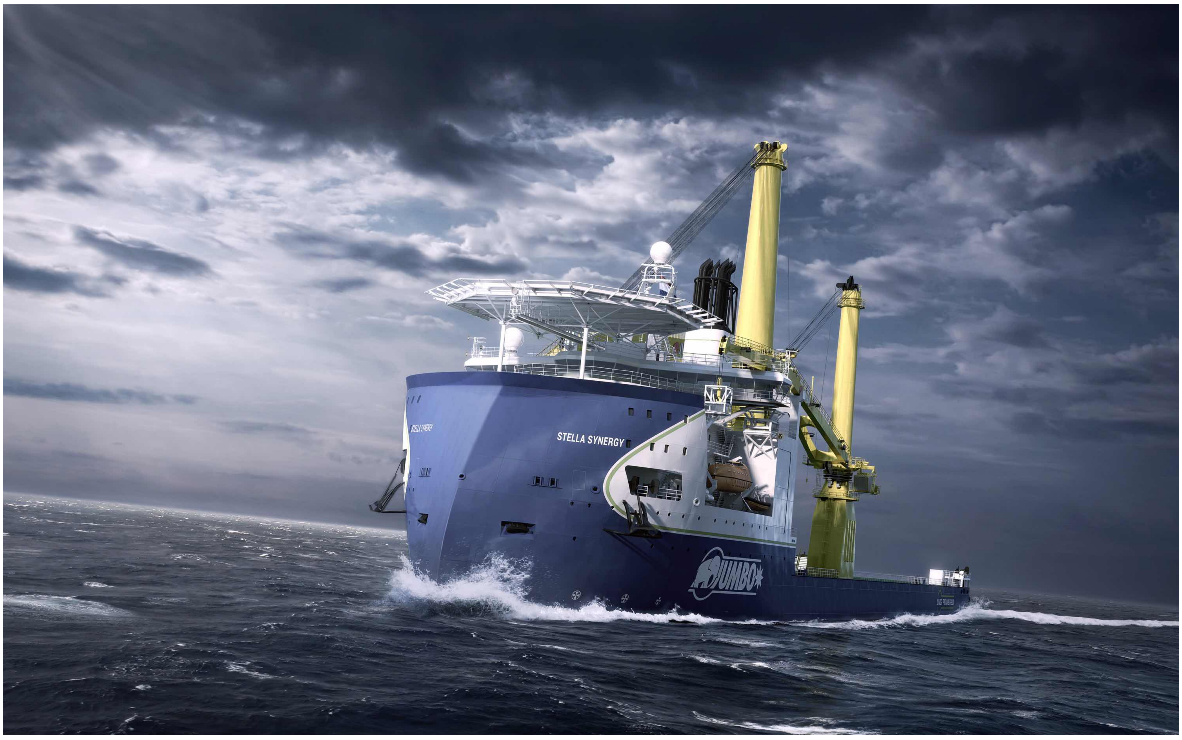

Figure 1-1: Stella Synergy

Chapter 2

Installation process

During the installation of a monopile, many elements play a role. Environmental forces cause vessel motion, a Dynamic Positioning (DP) or mooring system is used for station keeping, and the pile gripper counters the vessel motion and guides the monopile during the pile driving. Each installation phase is different, and all phases must be executed safely. Before starting with the installation, an angle of attack must be chosen, which greatly influences the possible shielding effect. This chapter elaborates on the different elements that play a significant role during a floating monopile installation.

2-1 Installation phases

The offshore installation of monopiles consists of multiple phases. The forces that act on the monopile and vessel differ for each phase, and each phase gives specific challenges. Generally, the installation of a monopile with a floating vessel comprises the following phases [21], [1]:

1. Transport the monopile to the location of the new wind farm. The monopile can be transported by the installation vessel, on top of a barge, or towed to the desired location.
2. Upend the monopile from a horizontal position to a vertical position.
3. Lower the monopile through the wave zone until it reaches the sea bed.
4. Activate the motion-compensated gripper to keep the monopile's upright position and remove the crane connection with the monopile. This phase is known as the early pile driving phase. The forces in the vertical direction are fully countered by the sea bed.
5. Driving the monopile into the sea bed until it reached the desired penetration depth.

It is preferable to transport the monopile on top of a barge to the installation site in most cases. But, the way of transporting the monopiles strongly depends on the upending method. This is further explained in subsection 2-1-1. Sections 2-1-1 to 2-1-4 focus on phases 2-5 and the different sub-phases that are involved during the installation.

2-1-1 Phase 2: Upending

The monopile arrives at the installation site in a horizontal position. Firstly, the monopile is rotated to a vertical position, this process is called upending. Nowadays, four upending methods are known; Upending using a separate upending frame, upending using multiple hooks, upending with a gripper frame, and upending in water [22]. The methods are briefly discussed here.

Upending with upending frame The monopile is placed in a separate upending frame, which only supports the monopile during the rotation. Afterward, the monopile, which is now in a vertical position, is placed in the gripper. This method is not preferable since it is a time-consuming process, and extra deck space is needed for the upending device.

Upending with multiple hooks The monopile is lifted with multiple separately controlled hooks. Although this is a fast upending process, it has two considerable disadvantages. The maximum crane capacity cannot be reached because the lifting cables are under an angle during the rotation, and the operation is less controlled.

Upending with gripper frame The main crane places the monopile directly in the rotating gripper. The Internal Lifting Tool (ILT) of the crane is attached to the monopile's upper end and lift it. The gripper only guides the rotation and acts as a hinge. This is a fast process since it only requires one lifting operation, and it is a safe process because the monopile is guided during rotation. The downside is that the gripper frame must be strengthened to cope with the monopile's large weight, and it must allow rotation. This results in a more expensive gripper.

Upending in water The monopile is towed to the installation site and is upended in the water. During the transportation of the monopile, it needs waterproof end-caps to remain buoyant. The ILT is connected to one end of the monopile and lifts it, and automatically the monopile is rotated. When the monopile is in a vertical position, it is placed in the gripper frame. A huge advantage of this method is that a monopile with a larger weight than the max safe working load of the crane can be upended due to the buoyant force [23]. The disadvantages are that the monopile needs end-caps, which must be removed carefully, and that the monopile must be towed to the installation site.

Optimal method The best option for the Stella Synergy is to upend with the gripper frame. It is a safe and fast process. It only requires an extra investment for a more advanced gripper frame. But, it has some limitations. The Stella Synergy's main crane has a maximum lifting height of 87 meters and a maximum lifting capacity of 2500 tonnes [24]. If the Stella Synergy wants to install larger or heavier monopiles than its crane limitation, it must use the upending in water method. Clearly, the way of transporting depends on the method of upending.

The monopile touches the seawater for the first time during the monopile rotation with the gripper frame. This means that hydrodynamic forces will act on the monopile. These forces could result in instabilities in certain sea conditions. In the study of [22], the focus lies on the workability of an installation vessel during six different sub-phases of the upending of the monopile with a gripper frame. The first phase is when the monopile is located in the gripper in a horizontal position. The last sub-phase, which is considered, is when the monopile is in a vertical position, and it is ready to be lowered. In sub-phase 1-2, the monopile is not submerged at all, and in sub-phase 3-6, the monopile is partly submerged. In the study of [22] is concluded that sub-phase 3, where the monopile is rotated 30 degrees from a horizontal position, is the most critical sub-phase during the upending process. During this sub-phase, the distance between the submerged part of the monopile and the vessel's center of rotation is large. This results in big moments due to hydrodynamic forces. Also, the horizontal forces acting on the gripper are the largest during this sub-phase.

2-1-2 Phase 3: Lowering

After the upending, the monopile is lowered to the sea bed. During the lowering of the monopile, it gains a larger buoyancy force. The vertical gravitational minus the buoyancy force acts entirely on the ILT until it touches the sea bed. During the lowering process, wind and hydrodynamic forces act on the monopile. These forces could lead to instabilities in certain sea states, although this phase is not expected to be the most critical one [22]. At the moment of touchdown, the monopile self penetrates the seafloor roughly half the pile diameter due to its weight [25]. Of course, this depends on the soil characteristics in place and the monopile characteristics. The exact location where the monopile will be installed is now determined. The study of [26] focused on lowering the monopile in the water without getting in contact with the seafloor. He simulated a continuous lowering process of the monopile. It this study is concluded that for the lowering phase the shielding effect could be crucial for the stability. Some explanation about the shielding effect can be found in section 2-4.

2-1-3 Phase 4: Early pile driving phase

After the penetration of the seafloor due to the weight of the monopile, some actions need to be taken before the pile driving phase can start. Firstly, the motion-compensated gripper frame is activated. This means that there is no rigid connection between the gripper and monopile anymore. The gripper frame compensates small vessel motion, and the gripper maintains the upright position of the monopile [19]. If the vessel loses position, it may damage the gripper and the monopile. After activating the motion-compensated gripper frame, the ILT is detached for the monopile, which results in a risky situation because the monopile can not be lifted anymore. According to [16], the maximum inclination angle during the installation of the monopile depends on the penetration depth of the monopile. A too large inclination angle could result in plastic deformation of the soil. Therefore, it is crucial to control the monopile's inclination angle during the early pile driving and the pile-driving phases.

The soil has only limited interaction with the monopile due to the low penetration depth. This means that the monopile acts like an inverted pendulum supported by the gripper frame. If a dangerous situation occurs now, for example, a storm is coming, it is not easy to lift the monopile back on deck and abort the installation. The next step is to connect the vibro drill to the main crane and lift it on top of the monopile. The study of [1] focuses on the workability of the installation vessel Stella Synergy during the early pile driving phase. For station keeping, mooring lines were used in this study, and he assumed no soil-monopile interaction. The study of [21] also focuses on the early pile driving phase, but here soil-monopile interaction is assumed. This interaction is modeled with the lateral soil resistance-deflection relationship, or better known as the PY-curve. In this study is concluded, it is better to assume no interaction, because the stability force gained by the monopile-soil interaction has large uncertainties and it is better to take the worst-case scenario.

2-1-4 Phase 5: Pile driving

After finishing the early pile driving phase, the vibro drill is connected and the motion-compensated gripper frame is activated, thus the pile driving can start. The vibro drill drives the pile to a certain depth, and the gripper ensures the pile's vertical position. At a certain depth, the soil-monopile interaction is large enough to ensure the stability of the monopile [16]. Now, the motion-compensated gripper frame is detached to avoid large mooring forces of the monopile. After the inclination angle is measured and corrected, the pile driving can continue to the final penetration depth. The driving of monopiles is conventionally done using a hydraulic hammer, this process is known as piling [27]. This conventional way of pile driving causes high noise levels, which damages marine life. Therefore, a vibro drill, which is less noisy, is used for driving the pile. The study of [16] focused on the installation of monopiles considering multiple penetration depths. In this paper, it is concluded that if the gripper is modelled to be rigid, the gripper should release the pile at a certain penetration depth. This is to avoid a resonance situation of the combined ship-monopile interaction. Notice that the inclination angle of the monopile must be controlled during the pile driving phase to avoid plastic deformation of the soil. According to [16], the maximum inclination angle at delivery is 0.25 deg to 0.5 deg, depending on the connection of the transition piece. A bolted connection requires a maximum inclination angle of 0.25 deg and a grouted connection of 0.5 deg.

2-1-5 Critical installation phase

In the study of [1], research is done on which installation phase is governing in terms of risk. Here is concluded that this is the early pile driving phase. During this phase, the monopile has limited soil stability due to the low penetration depth. Thus the gripper must be capable of keeping the vertical position of the monopile. If the gripper fails or the vessel is not capable of station-keeping, it could damage material and people. Also, in this phase, it is impossible to lift the monopile and abort the installation because the ILT is not attached anymore. Therefore, the early pile driving phase is the critical installation phase.

2-2 Pile gripper

When monopile's are installed by a floating vessel, a motion-compensated pile gripper is needed. In this section is explained why a motion-compensated gripper is needed and what it main tasks are. Afterwards is explained what the main characteristics are and how the gripper could be modelled.

2-2-1 Main tasks

During the pile driving phase, the monopile must be assisted by the gripper frame. Otherwise, it will be unstable. An analogy with a man that is hammering a nail into the wood can be made. If the man does not support the nail with his finger, it will fall. If the nail penetrates the wood far enough, he can continue hammering without using his fingers. The same holds for the installation of a monopile. After a certain penetration depth, the gripper can be detached, and the pile-driving can continue [16]. Multiple fixed pile gripper frames are produced, such as the two arm gripper, the four-arm gripper, and the subsea frame [22]. With those grippers, jack-up rigs have successfully installed lots of monopiles. But, in the future, floating vessels will be used more frequently [15]. Doing the installation operation using a floating vessel could be less time-consuming, and it is better capable of installing in deeper waters. A big downside of installing with a floating vessel is that the vessel will have a certain footprint during the installation [15]. If a floating vessel uses a fixed pile gripper, it is restricted by a limited sea state, and the workability is low. Therefore, the motion-compensated gripper frame is developed. The early pile driving phase is the phase where the motion-compensated pile gripper is activated. It has two essential tasks; Compensate for the vessel's surge and sway motion and keeping the monopile in a vertical position [19]. The gripper compensates the vessel's horizontal translation motions, by creating a countering motion with the centre of the gripper relative to the vessel's location. The gripper keeps the monopile in a vertical position by acting a restoring force at the monopile when it is inclined.

2-2-2 Characteristics

A motion-compensated pile gripper has a frame that can move in surge and sway direction, the frame has a limited motion envelope depending on the gripper dimensions. Most frames consist of two rotational arms and a ring which can be translated relative to the vessel's hull. The vessel's motion and the monopile's inclination angle are measured continuously, these signals are sent to the control system [19]. The gripper in figure 2-1 has four hydraulic cylinders which are controlled by the gripper's control system. Two hydraulic cylinders are used to rotate the gripper's arms, these rotation mainly cause a motion in surge direction. The two other hydraulic cylinders are used to translate the ring in sway direction. The ring acts a force at the monopile via its four contact points, to keep the monopile in a vertical position.

In the study of [21] research is done on minimum gripper dimensions and minimum force applied by the gripper. Here a significant wave height of 2.5 meters, 2.5 knots current speed, and 19 knots winds speed are assumed. These environmental conditions are approximately the maximum sea conditions during an offshore installation [21]. The gripper frame's limitations in this study are as follows: Envelope in surge direction of +/- 1.8 meters, envelope in sway direction of +/- 2.6 meters, and a gripper force of 3.6 MN. There are multiple ways how to model a motion-compensated gripper, which is explained in the next part.

2-2-3 Model of the gripper

A simple way to model the gripper frame is shown in figure 2-2. This simple representation of the gripper is used in the study of [25]. If the monopile has a displacement or velocity, it is pushed back toward the middle of the gripper. A realistic spring constant and damping coefficient must be chosen. In this model is assumed that the motion of the vessel is perfectly compensated.

In the study of [1], the motion-compensated gripper is modeled as a single Proportional Integral Derivative (PID) controller to control monopile's inclination angle. He used two boundary conditions. The monopile inclination angle is maximum 0.5 degrees, and the maximum force must not exceed a certain limit to maintain monopile's integrity. Just as the previously described model, in this model is assumed that the motion of the vessel is perfectly compensated.

A similar method to model the motion-compensated gripper is used by [21]. Instead of one, in this study, two PID controllers are used. The first controller controls the inclination angle, and the second one compensates for the vessel's motion. Although one of the gripper's main tasks is to compensate for the motion of the vessel, it does not succeed fully on it. According to Temporarily Work Design (TWD) [19], one of the developers of motion-compensated grippers, the gripper compensates for 95% of the surge and sway motion of a vessel. Thus, the motion of the vessel will still have a small effect on the monopile. Therefore, to model the gripper correctly, it is important to use a second control system to control the motion compensation of the vessel. In this case, a second PID controller is used.

to use a second PID controller for the vessel's motion.

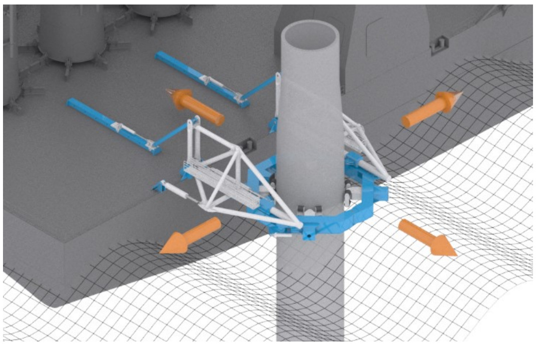

Figure 2-1: Example of a motion compensated pile gripper

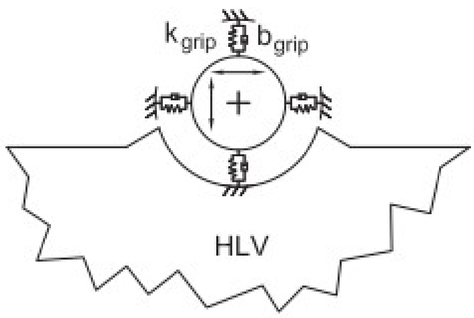

Figure 2-2: Gripper, modelled as 4 dampers and 4 springs

2-3 Station-keeping systems

As explained in section 2-2, the acceptable footprint of a vessel is limited by the motion-compensated gripper. To keep the vessel's footprint as small as possible a station-keeping system is needed. Two station keeping systems are frequently currently used, a DP-system and a mooring system. This section elaborates on these two station keeping systems.

2-3-1 DP-system

In the 1960s, the first DP system was introduced which compensated in 3 Degrees of Freedom (DoF). The horizontal surge, sway, and yaw motions were controlled by a single-input single-output PID control algorithm [28]. In 1977, the first DP-system that applies modern control theory using a Kalman filter was produced [29]. A small group of engineers and scientists produced this DP-system with the Kalman filter. They are now known as the Kongsberg DP. Nowadays, Kongsberg DP still contains the majority of the grown DP market [29]. Every DP-system contains multiple position reference systems, a (Kalman) filter, a control system, and a thruster allocation algorithm. These different components are elaborated in this section.

Reference systems The goal of a DP-system during the installation of a monopile is to have zero velocity at a prescribed position and heading. The DP-system needs input about the vessel's current position and heading to achieve this goal. This input is delivered by multiple reference systems. A DP system relies on more than one reference system to get an accurate and reliable input [29], [30]. In this paragraph, some of the frequently used reference systems are explained.

The Differential Global Positioning System (DGPS) is the most used reference system [31]. DGPS is an enhancement of the well known Global Positioning System (GPS) system. Similar to GPS, it uses multiple satellites to estimate the vessel's position. A difference to the GPS system is that DGPS uses ground-based fixed reference stations to broadcast the difference between positions indicated by the satellites and the known ground-locations . This results in an accuracy that is in the order of a few decimeters [31].

The Hydro acoustic Position Reference (HPR) system uses a transponder present on the seabed in combination with a transducer located on the vessel [31]. The transponder sends acoustic pulses to the transponder. Because the velocity of sound through the water is known, it is possible to calculate the distance between the transponder and the transducer. There are three HPR-systems developed, all used for other water depths. The long-baseline uses at least three transponders and one transducer. It operates at water depths of more than 100 meters. The short baseline uses one transponder and multiple transducers, and it operates at depths of 20 to 100 meters. The third system, with an ultra-short baseline, uses only one transponder and one transducer. Besides the distance between the transponder and transducer, the angle to the transponder is determined as well. This is only used in shallow water depths.

The taut wire is a mechanical position reference system [31]. A wire with a depressor weight is lowered until it reaches the seabed, now the sea depth is known. During the vessel's movement, constant pressure of the wire is maintained, and the angle of the wire where it is leaving the vessel is measured. With the measured angle and the known water depth, the vessel's distance to the lower part of the taut wire is calculated. Simultaneously, the vessel's roll and pitch angles are measured to correct the measured wire angle. The taut wire is only used in shallow water depths. If it is used at larger depths, the wire will deform due to its weight, and the incoming angle cannot lead to an accurate position estimation.

The inertial reference system determines the positions relative to a starting point. Due to small inaccuracies of measuring the vessel's velocity and heading, inaccuracies of position arise over time [31]. The deviations will grow rapidly over time. Thus, the inertial reference system is only accurate over a short period and will never be used as an autonomous system.

The Stella Synergy will be equipped with multiple systems described above. The following systems will be used: A DGPS system, two HPR systems, a taut wire system, and an inertial reference system [32]. The HPR system can be used as a long baseline, short baseline, and ultra-short baseline to cope with varying water depths. The taut wire can be used up to a water depth of 500 meters.

Kalman Filter For a vessel operating on DP, it is essential to identify the vessel's velocity and position. The Kalman filter plays a crucial role here. The Kalman filter is an estimator of vessel state based on noisy measurements from the reference system and sensors [30]. The amount of noise in the measurements depends on the sort reference system and sensor which are used. The Kalman filter determines for every reference system in place the accuracy of the measurements. Depending on the accuracy of the measurements, it gives different gains to them. Higher gains are given to measurements with higher accuracy. Based on the vessel's model, the forces acting on the vessel, the previous vessel state estimation, and the Kalman filter, the DP-system determines the new vessel state. If only the vessel model would be present and no reference system would be active, only a tiny error in the model will result in a large error over time. That is why it is crucial for a vessel that is operating on a DP-system always to have at least one reference system active [31]. Another important role of the filter is to remove the wave frequency of the vessel's motion signal [33]. Only the low frequency motion is sent to the DP-control system. A Kalman filter is a recursive data processing algorithm, which means that it does not need to store all the previous data [30]. All the previous data is already stored in the most recent state estimation of the vessel.

DP-control system The DP-control system is, in most cases, a PID-controller, which uses the estimated vessel state as input [31]. This input is compared with the goal of the vessel. In the case of installing a monopile, the goal is to have zero velocity at a given position and heading of the vessel. The PID-controller determines the control action by summing the calculated proportional, integral, and derivative parts. This control action is the demanded thrust in a specific direction. This thrust demand is sent to the thruster allocation algorithm.

Thruster allocation algorithm The thruster allocation algorithm has as input a thrust demand in a particular direction, and it contains information about the thruster configuration and maximum power of each thruster. The output of the algorithm will be the individual thrust for each thruster and the azimuth direction. Here an optimisation problem arises, in which multiple options will give the demanded thrust in that particular direction. A quadratic cost function is used to minimize the consumed power, resulting in the lowest fuel consumption [34]. Of course, the maximum thrust of each thruster must be implemented as a limitation in the thruster algorithm. Otherwise, it could be that a thruster is not able to deliver the thrust which is demanded.

For the DP system, it is also essential to determine the forbidden zones of the azimuth thrusters [35]. Those are the angles where an azimuth thruster is not allowed to deliver thrust. The forbidden zones could be determined to avoid thruster-thruster interaction. The forbidden zones could be implemented as limitations for the thruster algorithm.

Instability problems with external loads DP-systems are designed to operate in certain modes. The most common modes are auto heading mode, auto-positioning mode, joystick mode, and green DP mode [31]. Although the Stella Synergy's DP-system has a heavy lift mode [32], which is optimised for lifting heavy structures, it is still possible that instabilities occur due to the fast-changing forces of a heavy lift operation [35]. For example, lifting an enormous structure such as an XXL-monopile could lead to fast-changing external forces. If this leads to instabilities, it could cause damage to monopile, gripper, or even human people.

In the study of [36] five solutions to this problem are proposed, in which the external forces are countered. According to this study, the best option is to feed the estimated external forces into the Kalman filter. This results in a more reliable state estimation, and the damping of the DP-system is increased. In the study of [21], research is done on the footprint of a vessel operating on DP during lifting of a monopile compared to the same vessel without a lifting operation. In this study, the focus lies on two monopile sizes: the FB16 and the FB24. The FB16 weighs 870 tonnes and a length of 67 meters. The FB24 has a weight of 1653 tonnes and a length of 97 meters. The FB16 resulted in an enlargement footprint of 16%, and the FB24 resulted in an enlargement of 87%. Thus, the monopile's size and weight are quite important for the footprint of a vessel during installation. Also, in this study, it is concluded that the external forces should be fed forward into the Kalman filter for better results.

2-3-2 Passive mooring line system

Besides using a DP-system for station-keeping, there is the more classical way, using a passive mooring line system. Using mooring lines in combination with an anchoring system has been used for ages. Mooring passive systems are the most reliable and common devices to obtain the required position and control [37]. Today, there are three mooring line types. A mooring line consists of chained lines, wired lines, or synthetic fiber ropes. The chain mooring line is the most common type. It has low elasticity, a high breaking load, and a large weight. Due to the large weight, the chain mooring lines are only used for relatively small depth. The wire mooring line is made from multiple steel wires, which are entangled as a spiral. It has a larger elasticity and is lighter than the chain mooring line. The synthetic fibre rope is very elastic and very light, it can even be buoyant. Synthetic fibre ropes are made from lots of different materials. Nowadays, multi-components mooring lines are made to make use of the different advantages of multiple mooring line types. The cost of a mooring line can also be decreased through the appropriate combination between multi-components [38]. Together with the vessel's shape, the mooring lines determine the motion's stiffness.

2-3-3 Best station-keeping system for installing monopiles

Using a mooring-system compared to a DP-system during the installation of a monopile, gives some advantages and disadvantages. A disadvantage of using mooring lines is that it is a very time-consuming process due to the need for tug boats to put the mooring lines in place. The heavy-lift vessels which will be used in the monopile installation business are enormous and they have a very high day-rate [39]. Therefore, the installation time must be reduced as much a possible. Another disadvantage: weather vaning is not an option when a vessel is using its mooring lines, and this is possible if a vessel is operating on DP. When the angle of attack of the environmental conditions is changing direction during the installation, it could be that the installation must be aborted when mooring lines are used. Using a mooring system also brings some advantages. A mooring line system is a passive system, which means that it does not require thrusters for station keeping. This saves fuel during the installation activities. The thruster configuration does not need to be as sophisticated as when a DP system is used. It is not yet known if the vessel's workability is higher when a mooring system or when a DP-system is used. It would be very interesting to find out which system would optimise the workability because the time period that the vessel is not workable is very expensive.

Cost reduction is the main driver to choose between a DP-system and a mooring system. The day rate of heavy lift vessels is enormous. Reducing the installation time and increasing the workability of the vessel is crucial. The installation time is minimal when the vessel is operating on DP, but it is not yet known if the workability is also higher when the vessel is operating on DP. Therefore, it is not yet known what the best station keeping system is. The study of [1] focuses on the workability of the Stella Synergy during the installation of monopiles using a mooring system. Thus, it would be very interesting to research the workability of the Stella Synergy while it is operating on DP.

2-4 Shielding effect

For installing a monopile with a floating vessel, it could be interesting to make use of the shielding effect. The shielding effect occurs when the incoming waves are diffracted by the vessel, before they can reach the monopile. The vessel literally protects the monopiles for the waves. In this section is explained how the wave length and the angle of attack of the environmental conditions influences the shielding effect and monopile's response.

2-4-1 RAO reduction

The study of [26] focuses on lowering the monopile through the water without getting in contact with the seafloor. In this study the shielding effect is investigated. A significant reduction in extreme responses of the monopile due to environmental conditions is found due to the shielding effect. This can be measured in terms of response Response Amplitude Operator (RAO) reduction. A response RAO describes the vessel's or the monopile's response depending on the wave amplitude. The shielding effect only occurs when the operations are performed on the leeward side of the vessel, assuming that the waves are coming from the windward direction. According to the study of [26], the shielding effect is larger in short waves (+50% RAO reduction) than in long waves (+30% RAO reduction). This is because the response RAO's in short waves are dominated by waves on the monopile, and the shielding effect is essential. While in long waves, the RAO 's are dominated by the vessel and crane motion, and shielding is less important. In the study of [26] is concluded that it is better to use a floating vessel in short waves, and in long waves, it is better to use a jack-up vessel. Although, if a floating vessel in long waves is operating in head waves, it could still be favourable over a jack-up vessel.

2-4-2 Angle of attack

Unfortunately, the angle of incoming waves are not represented the same in each study which is considered. Therefore, an overview of how the incoming waves are represented in this literature review is shown in figure 2-3. The ideal angle of incoming waves to optimise the shielding effect is investigated in short and long waves by [26]. This is investigated by looking to the minimum extreme response of monopile rotation, considering different incoming waves angles. It is concluded that in short waves, the ideal angle is between 225-240 degrees, and in long waves, it is between 195-210 degrees. It is important to note that a gripper with bumpers is used during this study, which is a non-motion compensated gripper.

Also, in the study of [21], some research is done on the preferable angle of attack. Here the shielding effect is not considered. The preferable angle of attack is measured by looking at the footprint of the vessel operating on DP. It is concluded that the footprint with incoming waves of 210 degrees is smaller than in head waves. This is because less rotation of thrusters is required when the environmental load continually acts on the same side of the vessel. The thrusters only have to change their delivered thrust depending on the changing environmental load and do not have to change the thrusters' direction dramatically. Changing the direction of a thruster costs some time, and during this rotation, the vessel's footprint is increasing.

Thus, according to [21], to increase the shielding effect and to reduce the vessel's footprint during DP-station keeping, it is beneficial to keep the vessel at a certain angle to the incoming environmental loads. Jumbo Maritime usually keep the leading wind direction at angle angle of 195 degrees [22] during installation activities.

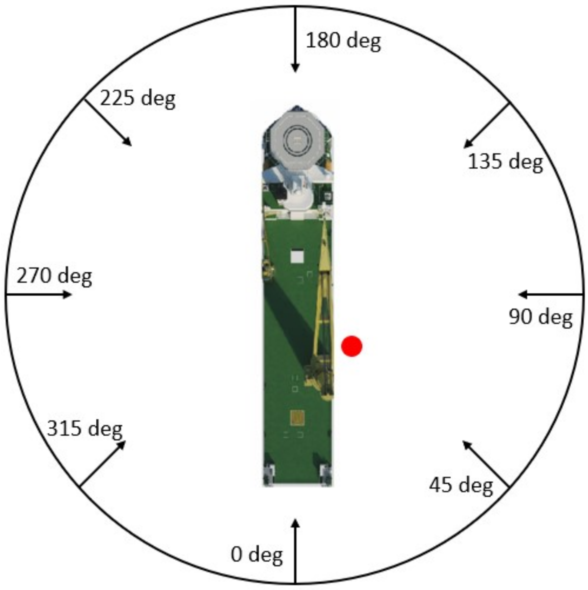

Figure 2-3: Overview of incoming angle of attack

Chapter 3

Environmental forces

Environmental conditions and, thereby, environmental forces play an essential role in offshore installation operations. During most installation operations, a vessel must keep its position as good as possible to ensure a safe workplace. The vessel can only guarantee a safe working place if it is able to counter the environmental forces. The higher the sea state is, the more challenging it is to counter the forces. Also, as already explained in section 2-4, the angle of attack could be crucial to decide if the operation can continue. The workable sea conditions for a vessel multiplied by the change that the particular sea conditions occur determine the vessel's workability. This chapter explains how the environmental forces and moments on a vessel and monopile can be calculated. First, the wave forces are explained extensively. Later the wind and current forces are discussed shortly.

Table 3-1: Description of symbols needed for this chapter

Symbol	Units	Description
H_s	m	Significant wave height
T_p	s	Wave peak period
Φ_r	m^2/rads	Radiation potential
Φ_w	m^2/rads	Undisturbed wave potential
Φ_d	m^2/rads	Diffraction potential
h	m	Water depth
g	m/s^2	Gravitational acceleration
k	rad/m	Wave number
ω	rad/s	Circular wave frequency
ω_p	rad/s	Circular frequency at spectral peak

3-1 Wave forces

Of all the environmental conditions, the waves have the largest impact on the vessel and monopile. Therefore, it could be interesting to know how to calculate the forces on the vessel and the monopile. This section explains how to calculate the wave forces and which theories could be used. It is assumed that the reader already has some knowledge about wave theory. All the symbols used in this section are explained in table 3-1.

3-1-1 Wave force on the vessel

Potential flow theory can be used to calculate the wave forces on a vessel. In potential flow theory, a non-viscous model is used to describe the fluid dynamics [40]. In this theory, it is assumed that the flow is homogeneous, irrotational, and incompressible. This potential flow theory is used to derive the first and second-order wave forces on the vessel. The vessel is assumed to be a rigid body floating in an ideal fluid with harmonic waves. The water depth of the North Sea can be assumed to be finite, which is a valid assumption for the installation of monopiles in the North sea since the average water depth of wind farms under construction in 2019 was 33m [11].

The waves are split up into three types of waves to be able to derive the wave forces on the vessel; Undisturbed incoming waves, radiation waves, and diffracted waves [4]. These three wave types are translated into velocity potentials with the use of potential flow theory. Together these potentials are called the linear fluid velocity potential, $\Phi(x, y, z; t)$. The linear fluid velocity potential is split into a radiation potential, an undisturbed wave potential, and a diffraction potential. The radiation potential, Φ_r, describes the fluid dynamics formed due to the vessel's motion in still water. The undisturbed wave potential, Φ_w, describes the incoming undisturbed waves. The diffraction potential, Φ_d, describes the waves diffracted by the vessel. These are the result of the undisturbed waves that hit the vessel's hull and change in direction. How these potentials are derived and which assumptions and boundary conditions are used can be found in Appendix A-1-2.

The wave forces are split up in different orders. The velocity potentials can be used to calculate the 0th, 1st, and 2nd order wave forces [4]. The 0th order force is the hydrostatic fluid force and can be calculated by integrating the hydrostatic pressure over the mean wetted surface of the vessel. The 1st order force can be calculated by linear wave theory. Using linear wave theory means here that harmonic displacements, velocities, accelerations of the water particles, and the harmonic pressures will have a linear relation with the wave surface elevation [41]. The 2nd order wave forces can be calculated by using the direct integration method. In this method, the hydrodynamic pressures, calculated by using the velocity potentials, are integrated over the vessel's hull. The second-order wave forces play an important role for a Dynamic Positioning (DP)-system. DP-systems filter the slow varying second-order wave forces, and only the second-order wave forces will be countered. An extensive explanation about how the wave forces can be derived is shown in Appendix 3-1.

The formula's to calculate the second-order wave forces, founded by the direct integration method, can be used to calculate Quadratic transfer functions (QTF)'s for the vessel. With the use of QTF's, the 2nd order wave forces on the vessel can be calculated based on the frequency of the incoming waves [4]. Some software programs, such as aNySIM, use QTF's in their calculations [1]. More explanation about how to derive QTF's is shown in Appendix A-1-4. QTF's can also be calculated using the software program Ansys AQWA [42].

3-1-2 Wave forces on the monopile

As shown earlier in this section, the first-order wave forces on a vessel are calculated with linear wave theory. The second-order wave forces are calculated with the direct integration method. These sophisticated and time-consuming methods can be used to calculate the wave forces on the monopile as well. But, if some simplifications for the monopile are assumed, a much easier method could be used to calculate the monopile's wave load. If a motion-compensated gripper is used, which compensates 95% of vessel's horizontal motions [19], it can be assumed that the monopile has almost zero velocity. This means that radiation waves caused by the monopile are not present. The shape of a monopile is much easier to describe than the hull shape of a vessel. If it is assumed that the monopile exists of cylindrical segments with a particular diameter, the Morison equation can be used [12]. The Morison equation has a limitation. It is only used for slender structures with a diameter to a wavelength of less than 1/5. To verify if the condition of a monopile installation in the North sea is not beyond this limitation, the dispersion relation, shown in equation 3-1 [4], is used.

$$\omega^2 = kg \cdot \tanh kh \tag{3-1}$$

According to this equation, if a water depth of 40 meters and a monopile diameter of 10 meters is assumed, all waves with a wave period of 5.7 seconds or more fulfil the requirements to use the Morison equation. The North Sea wave conditions and their chance of occurrence are shown in Appendix D. Here can be seen that approximately only 10.9 % of the waves have a smaller wave period than 5,7 seconds. According to the study of [1], only sea conditions with larger wave periods could be limiting for the workability of installing a monopile. Thus, the Morison equation, shown in equation 3-2, can be used to calculate the wave load on a monopile [12]. The Morison equation consists of a drag force and an inertia force.

$$F_{\text{Morison}} = 0.5\rho_{\text{seawater}}\, C_D \cdot Du|u|dz + \rho_{\text{seawater}}\, C_M \cdot D\dot{u}dz \tag{3-2}$$

With the following parameters:

$F_{Morison}$ = The force per unit length 'dz' [N]

u = The wave induces particle velocity [m/s]

$\dot{u}$ = The wave induced particle acceleration [m/s^2]

D = Cylinder diameter [m]

C_m = Hydrodynamic mass coefficient or inertia coefficient [-]

C_D = Hydrodynamic drag coefficient [-]

ρ_{seawater} = Sea water density [kg/m^3]

The spatial derivatives of the velocity potential of a harmonic wave, shown in equation A-9, are equal to the particle velocity components at a time and position. This is shown in equation A-3 [41]. The time derivatives of the particle velocity components result in the particle acceleration. The particle velocity and acceleration are needed to calculate the wave load according to the Morison equation.

3-1-3 JONSWAP wave spectrum

Wave spectra are used to describe the wave energy the ocean has for a certain wave frequency range [22]. Spectral analysis is based on the superposition principle of waves, which states that an irregular sea state can be observed as a summation of different linear waves with different height, period, shape, and direction [1], [21]. The two most commonly used wave spectra are the Pierson-Moskowitz spectrum and the Joint Northsea Wave Project (JONSWAP) spectrum. The JONSWAP spectrum is based on a large database of measurements on the North sea. Therefore this spectrum is the best choice for this research. These measurements are transformed into a spectrum with the Fourier transform. The shape of the JONSWAP spectrum for a given significant wave height, H_s, and peak period, T_p, is given by equation 3-3 [4].

$$S_{\text{JONSWAP}}\left(\omega\right) = \frac{320 H_s^2}{T_p^4} \omega^{-5} \exp\left(\frac{-1950}{T_p^4} \omega^{-4}\right) \gamma^A \tag{3-3}$$

With the following parameters:

$\gamma = 3.3$, which is the peakedness factor

$A = \exp\left(-\left(\frac{\frac{\omega}{\omega_p}-1}{\sigma\sqrt{2}}\right)^2\right)$

$\sigma = 0.07$ when $\omega \leq \omega_p$

$\sigma = 0.09$ when $\omega \geq \omega_p$

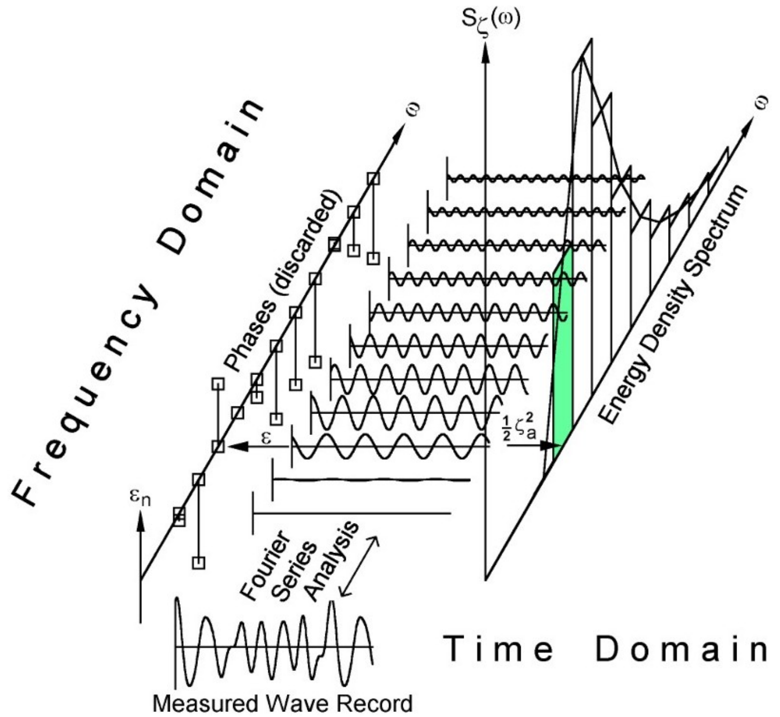

Figure 3-1: Wave record analysis and regeneration

With the inverse Fourier Transform, the wave spectrum is translated into a series of sinusoidal regular waves. The superposition of these waves will generate a wave elevation plot constructed in the time domain. How measurement of wave elevation form the JONSWAP spectrum, and how the JONSWAP spectrum can form a wave elevation plot is shown in figure 3-1.

Directional spreading The JONSWAP wave spectrum shown in equation 3-3 is unidirectional. This means that all the waves are coming from exactly the same direction. In reality, the waves have a certain spreading. This spreading depends on the local weather situation during that moment and the weather situation in the whole ocean in the recent past [4]. There are multiple methods to account for directional spreading. In Appendix A-1-5 these methods are elaborated.

3-2 Wind and current forces

In this section is explained how the wind and current forces on the vessel and and monopile can be calculated.

The aerodynamic load depends on the wind velocity and the frontal and sideways areas of the considered body. The wind speed varies over the z-axis and varies over time [12]. In Appendix A-2 is explained how the average wind velocity can be calculated depending on the 10 minutes average wind speeds at the height of 10 m. Additionally, it is explained how the wind speed varies over time depending on the chosen wind spectrum. The current speed consists of a wind-generated current and a tidal current. Both of them vary over depth z [12]. In Appendix A-3 is explained how the current velocity can be calculated.

If the wind and current velocities are known, the wind and current forces that act on a vessel and monopile can be calculated. The wind and current will only have a significant impact on the horizontal motions [42]. The wind and the current forces in x- and y-direction on the vessel and the monopile can be calculated with equation 3-4 [1]. This equation can also calculate the moment around the z-axis for the vessel caused by wind and current. The moment around the z-axis for a monopile can be assumed to be zero due to its cylindrical shape. For the wind forces, the frontal and sideways area's above the waterline should be used, and for the current forces, the frontal and sideways area's below the waterline should be used.

$$F_x = \frac{1}{2} C_x \rho U_{w/c}^2 \cdot A_F \qquad F_y = \frac{1}{2} C_y \rho U_{w/c}^2 \cdot A_S \qquad M_z = \frac{1}{2} C_\psi \rho U_{w/c}^2 \cdot A_S \cdot L_{pp} \tag{3-4}$$

With the following parameters:

A_F = Frontal area

A_S = Sideways area

$C_{x/y}$ = Wind or force coefficient in direction x or y

L_{pp} = Length between perpendiculars

The wind and current coefficients of the Stella Synergy are shown in C-1. In general, the aerodynamic forces are small compared to the hydrodynamical forces. The aerodynamic forces can even be neglected in many cases [21].

Frequently, during time-domain simulations, a specific significant wave height and wave period are chosen. After that, the corresponding wind and current velocities are taken using table 3-2 [43]. The peak wave period shown in this table is the most common peak wave period for this significant wave height. Frequently also other wave peak periods are tested. When the sea conditions are determined with this table, the wind and current velocities are not calculated.

Table 3-2: Environmental conditions

Beaufort number	**Beaufort description**	**Wind speed [m/s]**	**Significant wave height [m]**	**Peak wave period [s]**	**Current speed [m/s]**
0	Calm	0	0	Na	0
1	Light air	1.5	0.1	3.5	0.25
2	Light breeze	3.4	0.4	4.5	0.5
3	Gentle breeze	5.4	0.8	5.5	0.75
4	Moderate breeze	7.9	1.3	6.5	0.75
5	fresh breeze	10.7	2.1	7.5	0.75
6	Strong breeze	13.8	3.1	8.5	0.75
7	Moderate gale	17.1	4.2	9.0	0.75
8	Gale	20.7	5.7	10.0	0.75
9	Strong gale	24.4	7.4	10.5	0.75
10	Storm	28.4	9.5	11.5	0.75
11	Violent storm	32.6	12.1	12.0	0.75
12	Hurricane force	NA	NA	NA	NA

Chapter 4

Simulation setup and verification

This chapter describes step by step how the model is built. First, a model overview is shown, and some information about the used software programs is given. Then, it is explained which reference systems are used in the model, followed by the modelling of the vessel, the monopile, and the gripper. For each implementation step in the last three sections is explained how the model is verified.

4-1 Model overview

In this section, the model that is used to calculate the workability of the vessel during the installation of a monopile is elaborated. The model overview is shown in figure 4-1. The coloured dashed lines show the software programs that are used for modelling. The essential software program is the time domain simulation programs aNySIM. This program is used to do numerical simulations of the installations. More explanation about aNySIM is found in section 4-1-2. As input, aNySIM requires the HYD-files of the bodies present in aNySIM, the vessel and the monopile. An HYD-file describes how a body responds to incoming waves with a particular frequency, amplitude, and incoming angle of attack. These HYD-file of the vessel and the monopile are generated with the software program Ansys AQWA. More about how these HYD-files are formed and how Ansys AQWA is used is explained in section 4-1-1. The motion-compensated gripper, which is the connection between the vessel and the monopile, is also modelled in aNySIM. Python calculates the force to move the gripper and the force to keep the monopile vertical for each simulation step. This model aims to describe the vessel's motion, the gripper's motion's and the monopile's motion, considering the environmental conditions, the DP-system, and all the limitations. These motions and limitations represent the total workability of the installation activity.

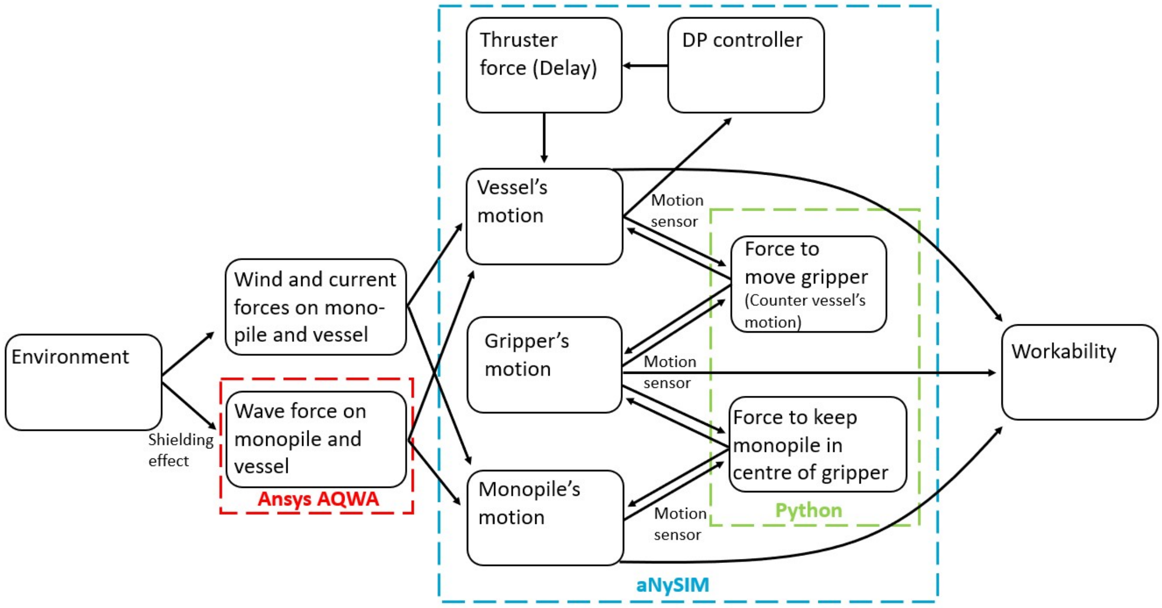

Figure 4-1: Model overview

4-1-1 Diffraction calculations with Ansys AQWA

Ansys AQWA is a software program that is capable of doing diffraction calculations by using the panel method. The panel method splits up the hull of the body that is considered in many small panels. These panels have a certain mesh size. Ansys AQWA calculates the force that acts on the panel for a particular incoming wave for each panel. These incoming waves vary in frequency, amplitude, and incoming angle of attack. The forces of all these panels combined determined the body's response to a particular incoming wave. The vessel's and monopile's response is calculated for every incoming wave and combination of incoming waves. Therefore, an enormous amount of calculations are made with Ansys AQWA. Only the submerged parts are important for these calculations.

Characteristics of the runs Ansys AQWA uses a 3D model of the vessel and the monopile as input. The 3D model of the monopile is designed in the program DesignModeler. Section 4-4-1 explains more about the monopile's design and its characteristics. Jumbo Maritime delivers the 3D model of the Stella Synergy. It does not contain the thrusters because it will not substantially influence the diffraction calculation, and it increases the computational effort. The viscous damping of the thrusters is estimated and added to the model. The merged 3D models are shown in figure 4-2.

The diffraction calculations are split up into waves with different frequencies with a frequency step of 0.025 rad/s. For each frequency step, Ansys AQWA calculates the added mass matrix and the added damping matrix. The incoming angles of attack are split up into 37 directions, with angle steps of 10 degrees. For verification reasons, calculations are made for 0 and 360 degrees. The vessel and the monopile can move in 6 degrees of freedom. For each frequency step, each incoming angle step, and for each degree of freedom, the force Response

Amplitude Operator (RAO)'s and its phase angles are calculated. Notice that there is a difference between a force RAO and a motion RAO. A force RAO describes the force per wave amplitude on a body, and a motion RAO describes the translation or rotation of a body per wave amplitude. More explanation about motion RAO's and how to derive them is explained in Appendix B-1.

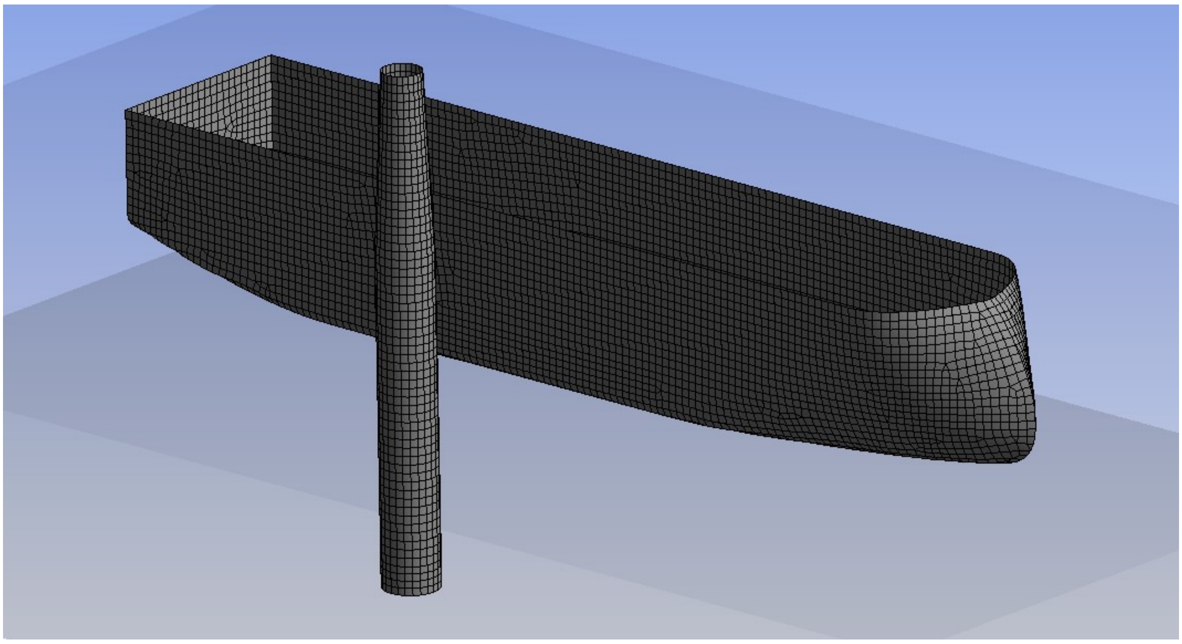

Figure 4-2: 3D model of the vessel and monopile in Ansys AQWA

The low-frequency second-order wave forces are calculated using real and imaginary Quadratic transfer functions (QTF)'s. In Appendix A-1-4 some explanation about QTF's is given. Here is explained that QTF's are formed by the difference of frequency pairs. For each incoming angle step, for each degree of freedom, and for each frequency step, seven QTF's are calculated. The seven difference frequencies that are near the particular frequency step are determined. An example for the used frequency pairs is shown in table 4-1. The first three rows of frequency pairs are shown for a particular degree of freedom and a particular incoming angle.

row 1	$\omega_1 - \omega_1$	$\omega_1 - \omega_2$	$\omega_1 - \omega_3$	$\omega_1 - \omega_4$	$\omega_1 - \omega_5$	$\omega_1 - \omega_6$	$\omega_1 - \omega_7$
row 2	$\omega_2 - \omega_2$	$\omega_2 - \omega_3$	$\omega_2 - \omega_4$	$\omega_2 - \omega_5$	$\omega_2 - \omega_6$	$\omega_2 - \omega_7$	$\omega_2 - \omega_8$
row 3	$\omega_3 - \omega_3$	$\omega_3 - \omega_4$	$\omega_3 - \omega_5$	$\omega_3 - \omega_6$	$\omega_3 - \omega_7$	$\omega_3 - \omega_8$	$\omega_3 - \omega_9$

Table 4-1: The first three rows of frequency pairs used to calculate QTF's at a particular angle of attack and degree of freedom

Three diffraction calculations are made with Ansys AQWA. The first calculation considers the vessel alone, the second calculation considers the monopile with shielding effect, and the last calculation considers the monopile without the shielding effect. This means that for the second diffraction calculation, the vessel lays still next to the monopile. Due to the vessel next to the monopile, the shielding effect is considered. The first and the third diffraction calculation are done with the vessel and monopile solely. For all the runs, a water depth of 40 meters is chosen.

For diffraction calculations of the monopile, it is assumed that the structure is not free to move. The monopile standing on the bottom of the seafloor without gripper support is an unstable situation. When Ansys AQWA runs a diffraction calculation of an unstable body that is free to move, it gives an error. Thus, the assumption that the monopile is not free to move is made. This means that the monopile's added mass and added damping matrices are full of zero's. Since the gripper strongly limits the monopile's motion, the effect of non-zero added mass and damping matrices will not be significant. Thus the assumption that the matrices are full of zero's is valid.

Decreasing the maximum element size in a diffraction calculation gives in a more accurate result. But, it also results in a more time-consuming run. In the study of [22], a diffraction calculation is made with Ansys AQWA for the Stella Synergy. According to this study, the accuracy of the heave RAO remains more or less constant for a maximum element size of 2.0 m and smaller. This means that the chosen maximum element size of 1.6 m for the vessel is accurate enough. The maximum element size of the monopile with shielding effect is 2.5 m, which is slightly larger. Unfortunately, due to the large submerged part of diffraction calculation 2 and a lack of computational power, a maximum element size of larger than 2.0 m is chosen. According to the study of [22], this maximum element size difference would results in a heave RAO with a difference of approximately 0.6 per cent. This difference is still acceptable. The maximum element size for the diffraction calculation of the monopile without shielding effect is chosen to be also 2.5 m. This is done to generate good comparable outputs of diffraction calculation 2 and 3.

Run:	**Vessel**	**Monopile (shielding)**	**Monopile (No shielding)**	**Units**
Structure is free to move	Yes	No	No	
Maximum element size	1.6	2.5	2.5	m
Lowest frequency	0.025	0.025	0.025	rad/s
Highest frequency	2.5	2	2	rad/s
Frequency interval	0.025	0.025	0.025	rad/s
Number of frequencies	100	80	80	–
Incoming angle interval	10	10	10	degrees
Number of incoming wave angles	37	37	37	–

Table 4-2: Characteristics of the Ansys AQWA runs

Convert Ansys AQWA output to Anysim input After the diffraction calculations are successfully finished, Ansys AQWA generates a couple of enormous output files with the results. Unfortunately, aNySIM is not capable of using these output files. The program needs a HYD-file with a specific format as input. The needed format differs a lot from the delivered format, and the number of RAO's and QTF's are enormous. In equation 4-1 and 4-2 is shown how many RAO's and QTF's are calculated for the first diffraction calculation.

$$N_{RAO} = N_\omega \cdot N_{winddir} \cdot N_{degFree} = 100 \cdot 37 \cdot 6 = 22200 \tag{4-1}$$

$$N_{QTF} = N_\omega \cdot N_{WindDir} \cdot N_{DegFree} \cdot N_{DifFreq} = 100 \cdot 37 \cdot 6 \cdot 7 = 155400 \tag{4-2}$$

With the following parameters:

N_ω = Number of wave frequencies

$N_{winddir}$ = Number of wind directions

$N_{degFree}$ = Number of degrees of freedom

$N_{DifFreq}$ = Number of frequency pairs per frequency

A Matlab file is written and used to transfer the output from Ansys AQWA to input for aNySIM in the correct format. More about the results of the diffraction calculations is explained in sections 4-3-3 and 4-4-4.

4-1-2 aNySIM

The comprehensive model that is made for the installation of monopiles with a vessel operating on Dynamic Positioning (DP) using a motion-compensated gripper is built in the program aNySIM. This software program, provided by Maritiem Research Instituut Nederland (MARIN), is capable of doing time-domain simulations. A second-order accurate explicit numerical method is used during these simulations. aNySIM advises using the Runge-Kutta2 (RK2) method for simulations with timesteps smaller than 0.3 sec. Since a timestep of 0.02 sec is used in the model, this second-order numerical method is chosen. RK2 is a robust method that is not too time-consuming at small timesteps. A small timestep of 0.02 sec is chosen because the monopile is modelled as a stiff system. Numerical stability issues could arise when a larger time step is chosen at stiff systems. In subsection 4-4-2 is explained why the monopile is modelled as a stiff system.

As explained in subsection 4-1-1, aNySIM needs an HYD-file that describes how the modelled bodies respond to incoming waves. In Appendix B-1 is explained how the vessel's motions can be calculated. aNySIM uses a slightly different method based on the change of momentum of a body. aNySIM requires the vessel's characteristics, the monopile and the gripper, and the environmental conditions for each simulation as input. As explained in subsection 3-1-3, the Joint Northsea Wave Project (JONSWAP) wave spectrum is during the simulations. aNySIM provides the options to add a filter, a Proportional Integral Derivative (PID)-controller and a thruster allocation algorithm. With these elements, a DP-system is built and tuned. More explanation about tuning the DP-system is found in subsection 4-3-4. It is up to the aNySIM user what the model's output variables are. In this research, the most important output is the vessel's, monopile's, and gripper's motions and the forces that act on these bodies.

The model is built up step by step in aNySIM. First, the vessel and the environmental conditions are implemented. Then, the thrusters with the propeller curves and the DP-system is added. Finally, the monopile and the gripper are added. These steps can be split up into many smaller steps, which is explained in the following sections. After each implementation step, it is checked if the implementation is correct by running small simulations. The more extensive the model gets, the longer the simulation time gets. Especially when the spreading of waves is added, the simulation time increases tremendously. This is because aNySIM must calculate for each separate angle of attack how the vessel and monopile respond. As the model is built up step by step, this chapter explains how the model is build-up and verified. First, the model of the vessel, then the model of the monopile, and afterwards, the model of the gripper is elaborated. In the chapter 5 is explained how these elements of the model influence each other.

4-2 Coordinate systems

The next three chapters explain how the vessel, the monopile, and the gripper are modelled. Of course, a critical element for these chapters is the reference systems. Multiple reference systems are used in the model. The most important one is the global earth fixed reference system, which is shown in figure 4-3. The origin of this reference frame is exactly at the waterline. The vessel has 6 degrees of freedom in which it moves. Surge, sway and heave are the translational motions. Roll, pitch and yaw are the rotational motions. A ship-fixed reference system is added to determine positions and motions relative to the ship's position. The ship-fixed frame's original position is at the vessel's hull, -8 m in z-direction below the global fixed reference frame. The monopile and the motion-compensated pile gripper both have a local reference system and earth fixed reference system to simplify the calculations. More about these reference systems is explained in sections 4-4 and 4-5.

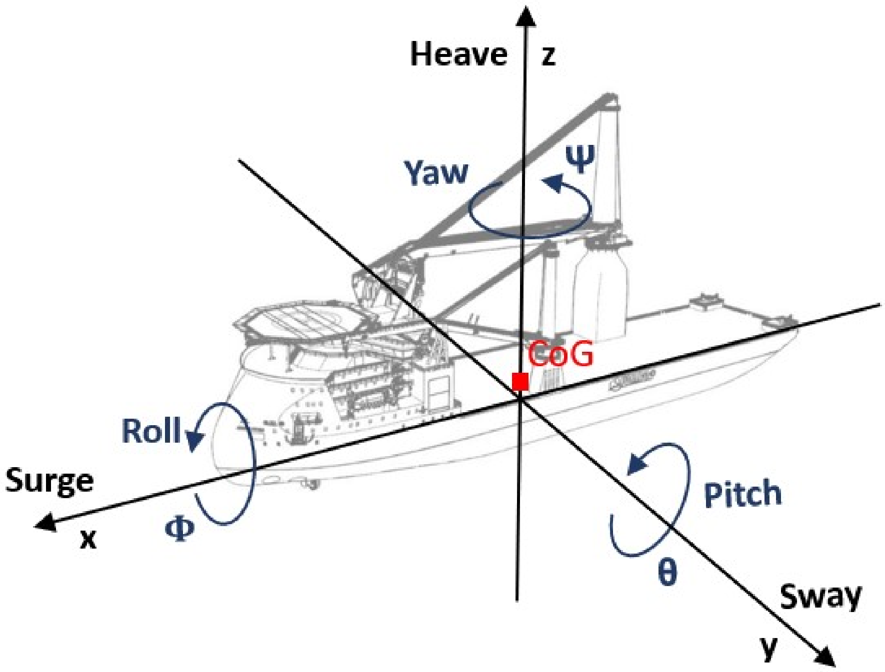

Figure 4-3: Global earth fixed reference system

4-3 Vessel

Jumbo Maritime plans to do monopile installations with the vessel 'Stella Synergy', which is currently under construction. Therefore, Jumbo Maritime is interested in the capabilities of the ship during such operations. This study is done to calculate the vessel's workability during the installation of monopiles. It is essential to model the ship as correctly as possible to get accurate results. This section explains how this is achieved.

4-3-1 Stella Synergy

In this subsection is explained what the characteristic of the Stella Synergy are, and how they are modelled. The thrusters capabilities and characteristics are discussed as well.

Characteristics of the Stella Synergy In this model, a heavy loading condition is assumed, which results in a Transverse metacentric height (GMt) of 7.01 m. Some other characteristics of the vessel are shown in table 4-3. The vessel is equipped with a DP-class 2 system. This means that it is capable of maintaining position and heading during any single fault in the DP-system, excluding loss of a compartment. The vessel is equipped with two Huisman cranes; The main crane of 2500 mt and an auxiliary crane of 600 mt.

Description	Symbol	Magnitude	Units
Length on waterline	LWL	185.44	m
Breadth on waterline	B	36.00	m
Draught	T	8.00	m
Mass	M	43898	tonnes
Displacement volume	∇	42785	m^3
COG at position from aft	LCG	90.24	m
Vertical position centre of gravity	KG	11.61	m
Vertical position centre of buoyancy	KM	18.61	m
Transverse metacentric height	GMt	7.01	m
Longitudinal metacentric height	GMl	347	m
Mass radius of gyration around X-axis	K_{xx}	13.7	m
Mass radius of gyration around Y-axis	K_{yy}	51.9	m
Frontal area, above waterline	A_F	1697	m^2
Sideways area, above waterline	A_S	3544	m^2
Frontal area, submerged	A_{Fs}	195	m^2
Sideways area, submerged	A_{Ss}	1288	m^2

Table 4-3: Characteristics of the Stella Synergy

Thrusters and propeller curves The Stella Synergy is equipped with five Rounds Per Minute (RPM)-controlled thrusters, meaning that the thrusters have a variable RPM and a fixed pitch over time. The vessel has two tunnel thrusters at the bow. These thrusters can only vary their delivered RPM and can not change the thruster's direction. It also has an azimuth thruster at the bow, which is capable of changing direction 360 degrees. In the aft of the ship, it has two main azimuth thrusters. These are also capable of changing direction. According to Schottel, which is the producer of the thrusters and engines, the maximum rotation speed of each azimuth thruster is 12 degrees per second. Maximum rotation speed means here the maximum rate of changing the direction of an azimuth-thruster. This thruster specification is also considered in the aNySIM model. The thruster configuration of the Stella Synergy is given in figure 4-4, and some information about the thrusters is given in table 4-4.

Figure 4-4: Thruster configuration

It is not possible to stop and start the engine of the thrusters unlimited. This is a time-consuming process that is only possible a few times per hour. Since it is hard to model this in aNySIM, it is assumed that the tunnel thrusters can deliver thrust in only one direction. Tunnel thruster 1 delivers thrust in portside direction and tunnel thruster 2 in starboard direction.

Table 4-4: Thruster information

Thruster	T1	T2	T3	T4	T5
Type	Tunnel	Tunnel	Azimuth	Azimuth	Azimuth
Thruster x-position [m]	77.5	72.0	66.3	-89.3	-89.3
Maximum thrust [kN]	354	354	519	895	895
Maximum RPM [-]	216	216	208	151	151

Every thruster type needs its own propeller curve to model a thruster correctly. A propeller curve is a curve that describes the thrust and torque coefficient C_T and C_Q depending on the propeller blade advance angle β. The blade advance angle is described by $atan2(v_a, v_p)$. v_a is the ambient water velocity, and v_p is the tangential velocity of the propeller at a distance of 0.7 times the radius from the propeller axis. More about the propeller curves can be found in [44]. Knowing the propeller curve and the RPM of the propeller, the delivered thrust and torque can be calculated. aNySIM provides standardised propeller curves for each propeller type; these are used and factored to get the requested thrust and torque. According to Schottel, for each thruster, it takes 10 seconds to reach the maximum RPM. Increasing the RPM of a thruster to the maximum RPM over time follows the same pattern as a function that is increasing its value to its asymptote. In the first seconds, the RPM increases rapidly, but the closer the thrusters RPM gets to its maximum value, the slower the increment goes. In aNySIM, this is solved by assuming that 99% of its maximum thrust is delivered in 10 seconds. In aNySIM, each thruster is modelled in the following way:

- Adapt engine power to reach the maximum RPM.
- Factor the deliver propeller curves to meet the requested maximum thrust with it's maximum RPM.
- Adapt the inertia of the thruster to reach 99% of it's maximum RPM in 10 seconds.

4-3-2 Natural periods and viscous damping

The damping matrices calculated in Ansys AQWA contain the radiation damping. It does not consider viscous damping effects. Viscous damping is generated by bilge keel damping, lift damping, eddy making damping, friction damping, and wave damping [4]. More information about the viscous roll damping of a vessel is found in Appendix B-1. Since it is very hard to calculate the damping elements separately, it is more convenient to determine the total viscous damping by decay tests. In this subsection, the natural periods for roll, surge, sway, and yaw direction are determined and verified. Then, the linear and quadratic viscous damping is calculated for these degrees of freedom. Linear viscous damping is linear with velocity and amplitude, while quadratic viscous damping is non-linear with velocity and amplitude B-5 [45]. The viscous damping for pitch and heave are neglected.

Roll decay Before the viscous roll damping is calculated, the natural period of roll must be determined. MARIN did some roll decay tests for the Stella Synergy on model scale. Based on these tests, the natural period of roll of the Stella Synergy is 12.14 seconds, which equals a natural frequency of 0.518 rad per second. The linear roll stiffness is determined with equation 4-3. The added mass for rolling at a frequency of 0.518 rad per second is calculated in Ansys AQWA. The natural roll period is calculated by filling in the mass of the vessel, the mass-radius of gyration around the X-axis, the added mass for roll motion, and the linear roll stiffness in equation 4-4.

$$C_{44} = g \cdot \nabla \cdot GMt \tag{4-3}$$

$$T_{\text{roll}} = 2\pi\sqrt{\frac{M \cdot k_{xx}^2 + a_{44}}{C_{44}}} = 12.13 \text{ s} \tag{4-4}$$

Some decay tests in aNySIM are done to verify the vessel's natural period in the model and calculate the viscous roll damping. In these decay tests, a roll moment is build-up that results in a roll angle. After a certain period of constant roll moment, it is removed suddenly. From that moment on, the vessel decays back to its initial roll angle of 0 degrees. The result of a roll decay test without added viscous damping is visible in figure 4-5. Considering the time period of the first 16 oscillations divided by the amount of oscillates gives a natural period of roll of 12.14 seconds. Now, the roll natural period in the model is verified since it is practically the same result as shown by equation 4-4 and by the model scale tests of MARIN.

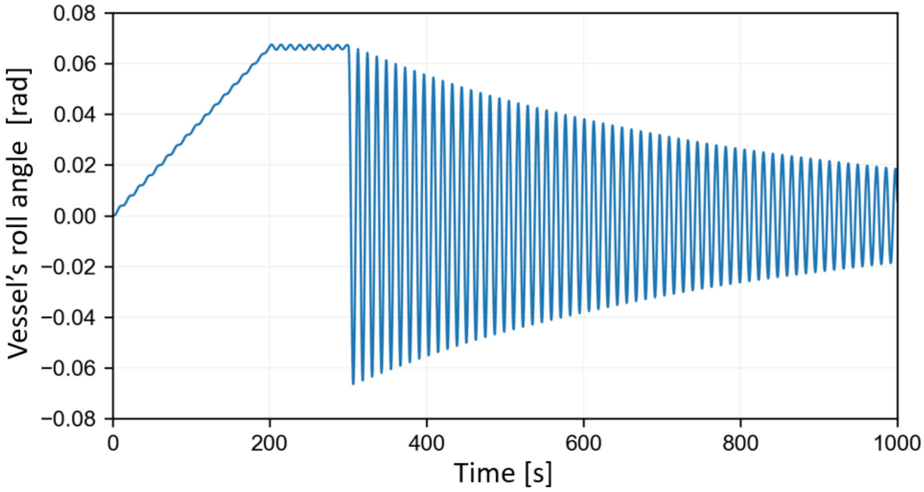

Figure 4-5: Roll decay test without viscous damping

The PQ-analysis is used to determine the linear and quadratic viscous roll damping. This analysis is applied to the roll decay tests on model scale of MARIN. The method is shown in figure 4-6. Every dot in the figure is based on the amplitudes of two successive peaks of the decay test. For the y-axis, the two amplitudes of the successive peaks are subtracted and divided by the average. The x-axis is the average of the two amplitudes of the successive peaks. The characteristics of the trend line give the P and Q values. With these values, the vessel's mass, added mass, and the natural period, the linear and quadratic damping is calculated. This is shown in equations 4-5 and 4-6.

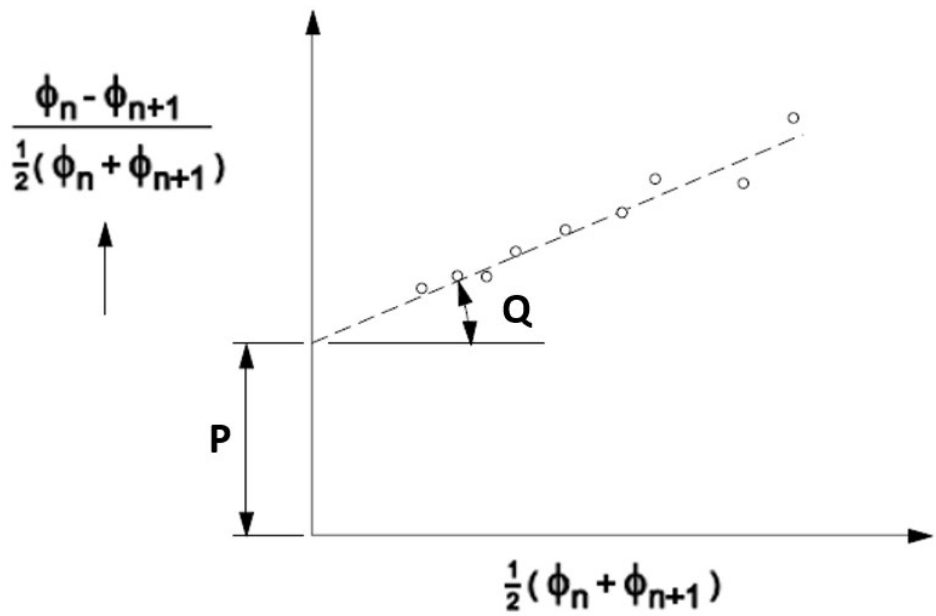

Figure 4-6: PQ-analysis

$$B_{ii-lin} = 2 \cdot \mathrm{P} \cdot \frac{\mathrm{M} + a_{ii}}{T_N} \tag{4-5}$$

$$B_{ii-qua} = \frac{3}{8} \cdot \mathrm{Q} \cdot (\mathrm{M} + \mathrm{a}_{ii}) \tag{4-6}$$

With the added linear and quadratic viscous damping, a new decay test is done. This decay test is compared with the decay test done by MARIN. Figure 4-7 is the superimpose decay test of the model on MARIN's decay test. The difference between the two decay tests is hardly visible. Therefore, the red lines are added. The part between the two red lines is MARIN's decay test, and the decay line that is visible over the entire figure is the decay test made with the model. Since the decay of the two tests is very comparable, the calculated linear and quadratic damping are verified.

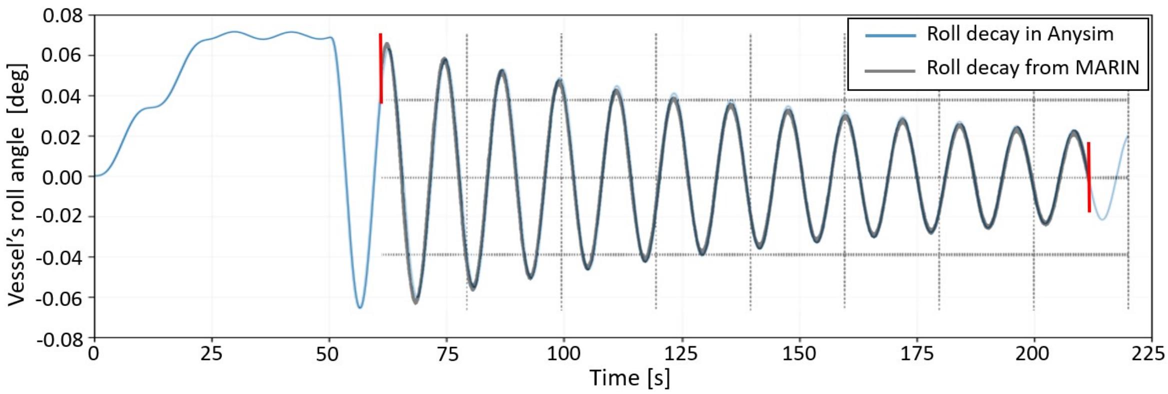

Figure 4-7: Comparison of two decay tests

Surge, sway, and yaw decay In surge, sway and yaw direction, some viscous damping needs to be added to build a realistic model. The vessel has no natural stability in these directions, thus doing a decay test does not work. For example, if the vessel experiences a force build-up in surge direction, it will sail away from its original position. Therefore, mooring lines are added to create a restoring force. The mooring lines arrangement is shown in figure 4-8. As explained in section 2-3-2, multiple mooring line types exist. Some mooring lines combine multiple mooring line types, and the chosen mooring lines are an example of this. They consist of a chained and a synthetic fibre rope called HMPE. Together with a Marine engineer of Jumbo Maritime, the mooring lines are selected. The chains are needed for extra weight near the seafloor, and the synthetic fibre rope is chosen for its elasticity and low price. The characteristics of the chosen mooring lines are shown in table 4-5.

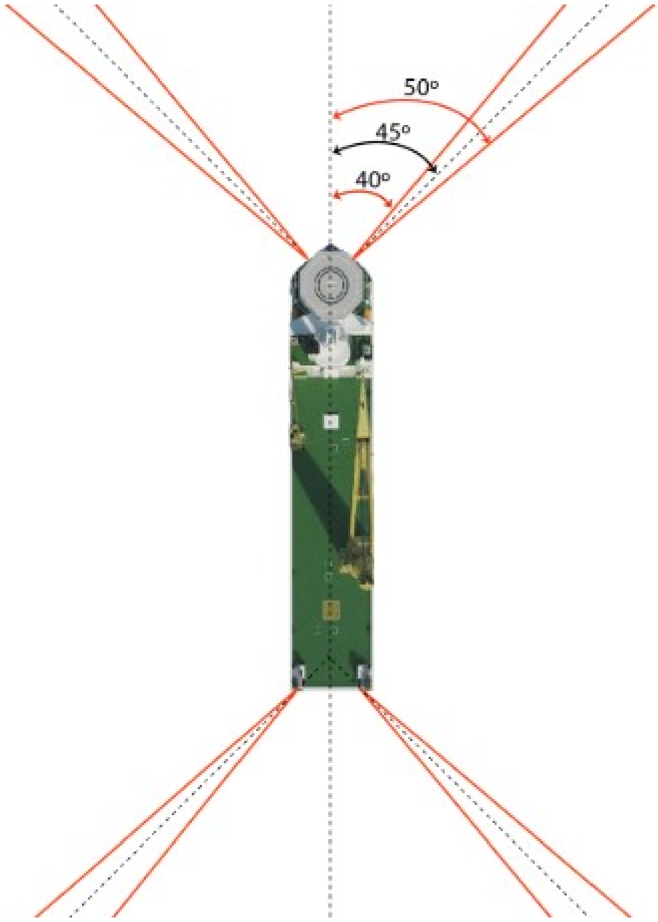

Figure 4-8: Mooring lines arrangement [1]

MARIN added some horizontal soft springs that act as a mooring system to their scale model. They did some decay tests in surge, sway and yaw direction to measure the naturals period and decay rates. In aNySIM, decay tests without added viscous damping are done with the mooring lines in place. The natural periods of these decay tests are compared. The natural periods for surge and sway were less than 3% off and are thus comparable. The calculated natural period in yaw direction was 22% larger than the measured natural period at MARIN. This difference could be due to scale effects or differences in mooring lines. For example, it could be that the vessel responds differently to the horizontally placed soft springs and the inclined mooring lines.

Table 4-5: Characteristics of the mooring lines

Description	Chains	HMPE	Unit
Section length	50	580	m
Diameter	76	52	mm
Weight in air	115	1.5	kg/m
Weight in water	100	-0.03	kg/m
Axial stiffness	493270	72200	kN
Minimum Breaking Load	4294	1970	kN

The PQ-analysis, which is explained in figure 4-6, is used to determine the viscous linear and quadratic damping for surge, sway, and yaw. Just as the viscous roll damping, these viscous damping components are added to aNySIM and decays tests are done. These decay tests are compared with the decay results of MARIN. For surge, the results are very comparable. Thereby, the calculated surge viscous damping is verified. Unfortunately, the results for sway and yaw were too far off. Again, this could be due to a difference in the natural period, a difference in mooring line system, model scale test errors, or the scaling effect. The used linear and quadratic viscous damping for sway and yaw are determined based on an iterative method. The decay results are comparable based on this method, and the calculated viscous damping is added to the model. The results of the superimposed decay tests and the chosen viscous damping components are shown in Appendix F.

4-3-3 Environmental forces on vessel

In chapter 3, some theory about the wave, wind and current forces is explained. Ansys AQWA uses this theory to do diffraction calculations, as described in subsection 4-1-1. In this subsection, the generated HYD-file of the Stella Synergy is analysed and verified. The wind and wave forces on the vessel are calculated in aNySIM and are also verified with the theory of chapter 3.

Diffraction calculation and wave forces As explained in 4-1-1, an HYD-file for the vessel is made. This HYD-file contains RAO's, QTF's, added mass and added damping matrices. With this HYD-file as input, it is possible in aNySIM to calculate the vessel's wave forces and the vessel's responds to those wave forces. But, the HYD-file must be verified before it can be used. MARIN made a similar HYD-file for the Stella Synergy, which is perfect for comparison.

For comparing the two HYD-files, it is important to know which part of the HYD-files the most relevant is. As shown in the scatter diagram of Appendix D, the wave periods of the North Sea wave conditions vary between 2 and 14 seconds. The study of [1] explains that the wave conditions that are critical for the workability of the Stella Synergy have a wave period of 7 seconds or more. Therefore, the focus lies on waves with a wave period between 7 and 14 seconds. Using the dispersion relation shown in 3-1 and a water depth of 40 m results in a wave frequencies range of focus between 0.45 and 0.90 rad/s. The studies of [1], [21], and [25] consider monopile installation activities from a floating vessel. These studies conclude that the preferable angle of attack during installations is between 180 and 210 degrees. A wave spreading range of 30 degrees is assumed in this study. Thus waves with an incoming angle between 165 and 225 degrees are relevant. In figure 2-3, the overview of the incoming angle of attack is given.

In figure 4-9 and 4-10, the force RAO's in x and y-direction from the two different HYD-files are shown, with an incoming angle of attack of 190 degrees. Any incoming angle between 165 and 225 degrees, except for 180 degrees, could have been chosen. All those plots give similar results; after a quick increment, the RAO-value drops over the increasing frequency, with small peaks and troughs. The force RAO in the y-direction with an incoming angle of 180 degrees is an exception because it is nearly zero for this angle.

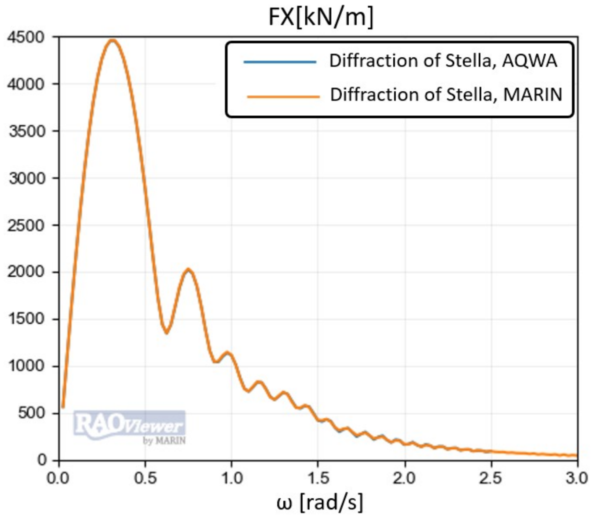

Figure 4-9: Force RAO in x-direction, incoming angle of 190 deg

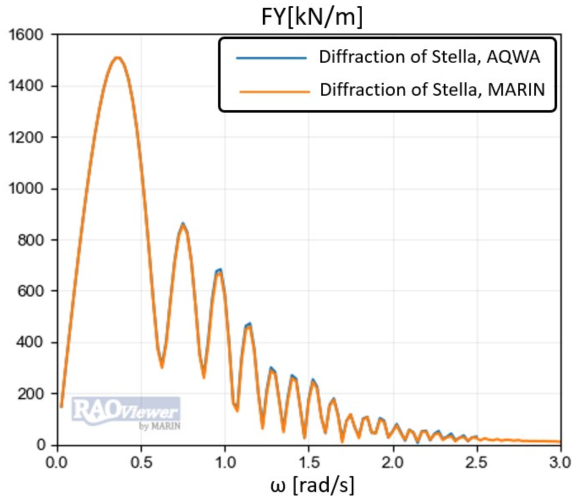

Figure 4-10: Force RAO in y-direction, incoming angle of 190 deg

The peaks and troughs of the other RAO-plots are probably caused by the following phenomenon: When the hull length is exactly n times the wavelength, it will cause at the same moment a peak (or trough) at the bow and the stern of the ship. The peaks (or troughs) will cancel each other, resulting in a trough in the force RAO. When the hull length is exactly (n+0.5) times the wavelength, it will cause at the same moment a peak at the bow and a trough at the stern of the ship (or reversed). The peak and through will strengthen each other and will cause a peak in the force RAO. The average diagonal hull length below water has to be considered for this phenomenon. When the waves attack the vessel not exactly from the front but under an angle, the hull length that the waves have to pass is larger than the hull length in the x-direction. Therefore, the diagonal hull length has to be considered. The averaged diagonal hull length of a wave coming at an angle of 190 degrees is approximately 163 m. For this hull length and the first four peaks of figure 4-9, this phenomenon is explained in table 4-6. The last row shows the ratio between the hull length and the wavelength. As explained, the ratio is approximately (n+0.5) for the peaks. The first peak differs probably because a wave with such a wavelength in a water depth of 40 m can not be considered as deep water.

Table 4-6: Force RAO peaks in x-direction for an incoming angle of 190 degrees. The averaged diagonal hull length is 190 m for this incoming angle.

	peak 1	peak 2	peak 3	peak 4
Wave frequency [rad/s]	0.3	0.75	0.975	1.15
Wave frequency [1/s]	0.048	0.119	0.155	0.183
Wave period [s]	20.94	8.38	6.44	5.46
Wave length [m]	406.0	108.5	64.8	46.6
Hull length/wave length ratio [-]	0.40	1.50	2.52	3.50

It is clearly visible in figure 4-9 and 4-10 that the plots of the different HYD-files are almost identical in the frequency range of focus. For most of the plots of force RAO's, QTF's, added mass matrices and added damping matrices, this is the case. Big relative differences occur when the results are close to zero. A good example is visible in figure 4-11, here the force RAO in the y-direction is shown for an incoming angle of attack of 180 degrees. It is essential to notice that the relative differences are large, but the absolute differences are small. Although the relative difference is large, the difference can be neglected.

Although the QTF-plots of MARIN and self-generated QTF-plots are always following the same trend, the QTF's plots give the largest absolute differences. An example of an QTF-plot with a big difference is shown in figure 4-12. Here the QTF for yaw is shown, with an incoming angle of 190 degrees. It is important to notice that the largest absolute differences occur out of the frequency zone of focus. Thus, it will not affect the vessel's response dramatically.

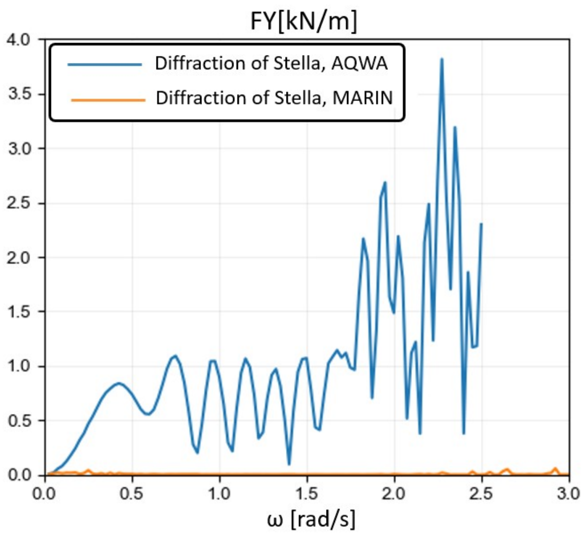

Figure 4-11: Force RAO in y-direction, incoming angle of 180 deg

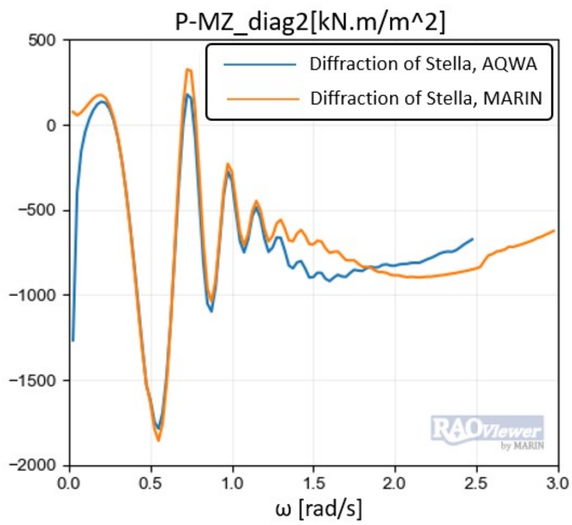

Figure 4-12: QTF for yaw, incoming angle of 190 deg

Unfortunately, it is not possible to show all the results of the generated HYD-files. But, all the results are analysed and considered to be comparable with the results of MARIN. The overall response of the vessel with the two different HYD-files is analysed and tested with multiple sea conditions, and it is concluded that the vessel responds similarly for both HYD-files. The self-generated HYD-file in Ansys AQWA is used for the model.

Wind and current forces In sections 3-2, some theory about the wind and current forces is explained. In aNySIM, the NPD wind spectrum is applied, with a constant wind speed over height. The wind coefficients for the Stella Synergy are determined by wind-tunnel tests at the company Ulstein Design & Solutions B.V. The results of the wind-tunnel tests are found in Appendix C-1.

The frontal and sideways area's above water of the Stella Synergy are given in table 4-3. The application position for the wind forces is assumed to be precisely above the Centre of Gravity (CoG) of the vessel. The height of the application position above the waterline is calculated by the sideways area above water divided by the length on the waterline. In aNySIM, multiple simulations with varying wind speed and incoming angle are done while the wind forces and moments are measured. During these simulations, the vessel's motion is frozen, and the wind speed is kept constant to get accurate results. No extra wind force is assumed due to structures placed on top of the deck of the vessel. Calculations are made with equation 3-4 to verify the measurements in aNySIM. The measured forces and moments in aNySIM are exactly the same as the calculated forces for each simulation.

Except for two differences, the current forces are modelled, calculated, and verified similarly. The current coefficients are determined by model scale tests at MARIN, and no current spectrum is applied. This means that the current is kept constant during all simulations. The current coefficients can be found in Appendix C-1. Again, the measurements of current forces and moments are exactly the same as the calculated forces.

4-3-4 DP-system

As explained in subsection 2-3-1, every DP-system contains multiple reference systems, a filter, a control system, and an allocation algorithm. In aNySIM, those separate elements are also available. In reality, a reference system gives noisy measurement, while a reference system in aNySIM gives a clear and correct output signal of the vessel's motion. The filter does not have to estimate the vessel's state. It only has to remove the wave frequency of the vessel's motion signal. The left-over signal is sent to the DP-control system. The control system consists of three PID-controllers to control the surge, sway, and yaw motion. Each PID-controller contains three gains. More explanation about tuning the gains is found in the next paragraph. The output of the three controllers is the demanded thrust in x- and y-direction and the demanded moment around the z-axis. The demanded thrust in x-, and y-direction and the moment around the z-axis are sent to the thruster allocation algorithm, which divides the demanded thrust over the thrusters. The thruster allocation algorithm demands a particular thrust and direction of each thruster. Still, due to the inertia of the propellers and a maximum rotation speed, the demanded thrust and direction is not delivered directly.

PID-controller gains Tuning the PID gains is very important for the DP-capability of the vessel. First, some standardised PID-gains are determined based on the vessel's mass and the vessel's added mass matrix for low frequency. The vessel was capable of station-keeping in relative low sea states when its DP-system uses these standardised gains. Then, the gains are tuned based on waves with a significant wave height of 3.0 m and a peak period of 9.0 s. This sea state is chosen because this is the critical wave condition with the highest probability of occurrence in the study of [1]. This is visible in figure 4-13. The sea conditions close to this sea condition also have a relatively high probability of occurrence. If the gains are optimised for this particular condition, the gains are also relative good tuned for the conditions close to this sea condition in the scatter diagram. This could result in a large workability of the vessel. According to [24], the expected preferable angle of attack of the installation is 195 degrees. Therefore, this angle is chosen to optimise the gains.

Hs [m] \ Tp [s]	3	4	5	6	7	8	9	10	11	12	13	14
0.25		0.18	0.05	0.02	0.07	0.08	0.01					
0.50	0.05	0.62	1.98	0.58	0.63	0.34	0.43	0.25	0.19	0.10	0.11	0.02
0.75		0.54	2.34	2.06	1.18	0.79	0.77	0.39	0.19	0.15	0.07	0.04
1.00		0.30	2.99	5.37	3.74	1.94	1.76	1.06	0.33	0.26	0.15	0.10
1.25			1.24	3.06	2.82	1.90	1.05	0.81	0.32	0.11	0.07	
1.50			0.41	3.75	4.30	2.43	1.44	1.23	0.61			
1.75			0.05	1.23	2.55	1.59	0.86	0.67	0.42			
2.00				0.72	3.32	2.39	1.34	0.74				
2.25				0.12	1.56	1.68	0.87					
2.50				0.03	1.32	2.17	1.09					
2.75					0.30	1.07	0.65					
3.00					0.16	1.05	1.14					
3.25					0.05	0.39						
3.50												
3.75												
4.00												
4.25												
4.50												
4.75												
5.00												
5.25												
5.50												

Figure 4-13: Scatter diagram of the workability of the Stella Synergy in the study of [1]

First, the surge gains, then the sway gains and afterwards, the yaw gains are optimised. Figure 4-14 gives an excellent example of the first steps of optimization of the PID gains for sway. Increasing the Proportional gain results in a faster response on the DP-system, but can results in instabilities. Increasing the Derivative gain decreases the overshoot of the DP-system. And increasing the Integral gain will push the average output value to the desired value.

Simulations with a relatively low time duration are done to decrease the simulation time. For every simulation, only one gain is adapted to see the result of changing that particular gain. Unfortunately, the surge, sway, and yaw gains influence each other. Therefore, after optimising the sway and yaw gains, the surge gains are not optimised anymore. Thus, these gains must be optimised again. Finally, this results in an optimisation loop. After going through the loop multiple times, the gains are considered optimised. With these gains, multiple 3-hours runs with varying sea conditions run to ensure stability over a longer time period. The results were promising.

With these founded gains, the monopile and the gripper are added to the model. After finalising the model, simulations are run to determine the preferable incoming wave angle. More about these simulations is explained in 5-2-1. These simulations showed that the preferable incoming angle is 180 degrees, which differs from the expectation of 195 degrees. Therefore, some extra optimising loops are executed with the same critical conditions and an incoming angle of 180 degrees. Again, the newfound gains, which are shown in table E-1, are tested extensively with varying sea conditions. The DP-gains shown in this table are called the original DP-gains.

It is crucial to keep in mind that the founded gains are not optimal for each sea condition. The DP capability of the vessel could be better when the gains are optimised for each individual sea state. Unfortunately, this is a very time-consuming process. When the Stella Synergy is in operation, there are always six staff members of Kongsberg DP on board to optimise the DP-system for each sea condition. It is clearly out of the scope of this thesis project to find the correct gains for each sea state.

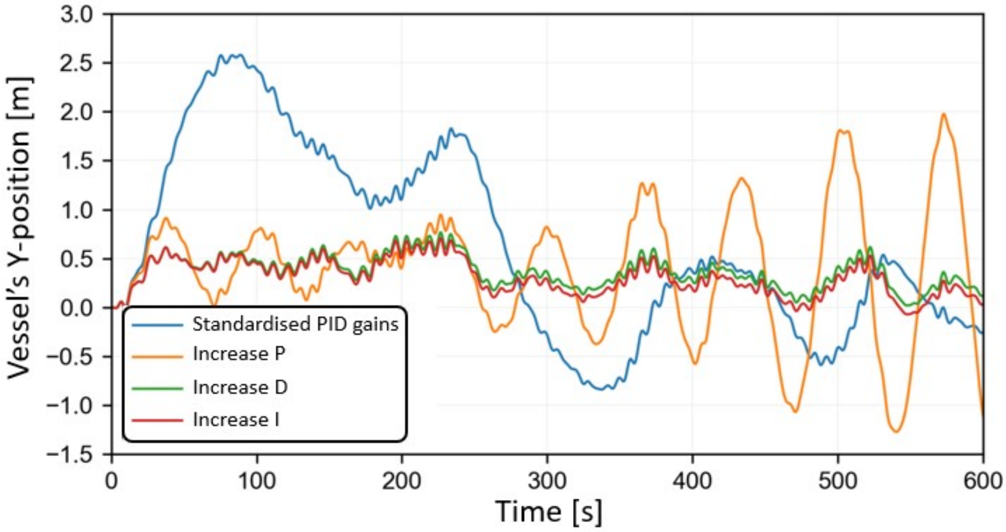

Figure 4-14: First steps of tuning the PID gains for sway

4-4 Monopile

As explained in section 1-1, the new 14 MW offshore wind turbine of General Electrics will be 260 meters tall, and the monopile will have a diameter of 10 m [14]. This is approximately the size of the monopiles that will be installed in the near future. This section explains how a similar monopile is designed and how it is modelled in aNySIM. Also, the location of installation relative to the vessel's location is determined.

4-4-1 Design

For each wind farm, a new monopile is designed based on the water depth, the soil conditions, the environmental conditions, and many other elements. The Stella Synergy does not focus on the installation of one specific wind farm. Therefore a general monopile is designed based on some assumptions. The 3D model of the monopile is designed in the program DesignModeler, which is a sub-program of Ansys AQWA.

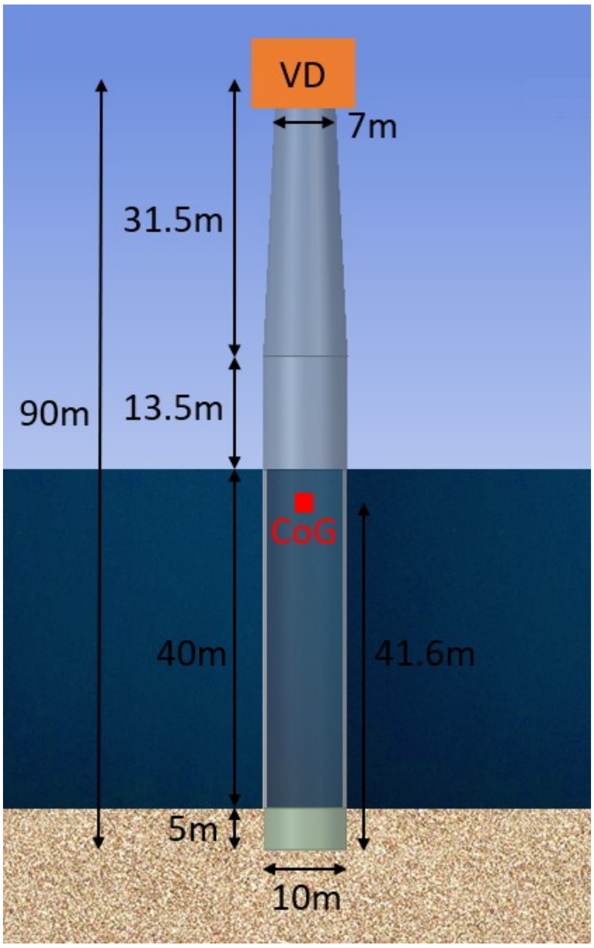

Figure 4-15: Design of the monopile, early pile driving phase

Characteristics Just as the new monopile of General Electric, the designed monopile has a diameter of 10 m. The length of the monopile is assumed to be 90 m, which is approximately the maximum length the main crane can lift if the monopile is upended in the gripper frame. The wall thickness is assumed to be constant over the monopile's height. It is assumed to be 1/100 times the monopile's base diameter, which results in 10 cm. The lower 58.5 meters of the monopile have a cylindrical shape, and the upper 31.5 meters are conical. This is to reduce the monopile's mass. The mass of the monopile with the chosen dimensions is 2068 tonnes, which is lower than the maximum lifting capacity of the main crane.

As explained in subsection 2-1-5, the most critical installation phase is the early pile driving phase. Therefore, in this thesis research, the focus lies on this phase. As preparation for the pile driving phase, a vibro-drill with an assumed weight of 1000 tonnes is placed on top of the monopile. The monopile's self penetration depth is assumed to be 0.5 times the monopile's diameter, see subsection 2-1-2. The design of the monopile, while it is in the early pile driving phase, is shown in figure 4-15. During the early pile driving phase, the submerged part of the monopile is filled with water. The water inside the monopile has a large volume and weight. When the monopile moves, the water has to move with it. The CoG shown in figure 4-15 is the combined CoG of the monopile, the vibro-drill and the trapped water in the monopile. The main characteristics of the monopile and the vibro drill are shown in table 4-7.

Table 4-7: Monopile's characteristics

Description	Symbol	Magnitude	Units
Length monopile	L_{mp}	90	m
Outer diameter monopile's base	$D0_{base}$	10	m
Outer diameter monopile's top	$D0_{top}$	7	m
Wall thickness	t	0.1	m
Mass monopile	M_{mp}	2068	tonnes
Mass vibro drill	M_{vd}	1000	tonnes
Mass trapped water	M_{tw}	3093	tonnes
Total mass	M_t	6160	tonnes
Radii of gyration x/y	$Rg_{x/y}$	28.5	m
Radius of gyration z	Rg_z	3.82	m

The radii the monopile's radii of gyration are essential to describe the motion of the monopile. The radius of gyration is the distance from the x-, y-, or z-axis of the monopile's local reference system to the point where the mass of a body is assumed to be concentrated. At this point, the moment of inertia is equal to the moment of inertia of the actual mass about the chosen axis. The monopile's local reference system is located at the combined CoG of the monopile, the vibro drill and the trapped water. The x-,y-, and z-axis are pointing in the same direction as the global reference system.

To determine the radii of gyration, first, the moments of inertia of the separate elements are calculated. The moment of inertia about the z-axis of a hollow cylinder is shown in equation 4-7. The moment of inertia about the x- and y-axis of a hollow cylinder is shown in equation 4-8. The lower part of the monopile is assumed to be a hollow cylinder; thus, these equations are used. The moment of inertia of the conical part of the monopile is assumed to be the average of the moment of inertias of two cylinders with outer diameters of 10 and 7 m. The trapped water and the vibro drill are assumed to act as solid cylinders. The moments of inertia of solid cylinders can be calculated with the same formulas with R_1 is zero. The moments of inertia about the same axis of different bodies can be added, as shown in equation 4-9. Finally, the radii of gyration are calculated with equation 4-10.

$$I_z = \frac{1}{2} \cdot M \cdot (R_0^2 + R_1^2) \tag{4-7}$$

$$I_{x/y} = \frac{1}{4} \cdot M \cdot \left(R_0^2 + R_1^2\right) + \frac{1}{12} \cdot M \cdot l^2 + M \cdot D^2 \tag{4-8}$$

$$\mathrm{I_t} = \mathrm{I_{mp}} + \mathrm{I_{vd}} + \mathrm{I_{tw}} \tag{4-9}$$

$$Rg_{\mathrm{t}} = (I_{\mathrm{t}} / M_{\mathrm{t}})^{1/2} \tag{4-10}$$

4-4-2 Model

Two reference systems are used to model the monopile. As explained before, the monopile's local reference system is located at the combined CoG of the monopile, vibro drill, and trapped water. The earth-fixed reference system is located at the bottom of the monopile. The axes are pointing in the same direction as the global reference system.

The monopile acts as an inverted pendulum during the early pile driving phase. This results in a very in-stable situation when the gripper would not be active. Although the self-penetration depth is 5 m, no monopile-soil interaction is assumed. Due to the large uncertainties of the soil stability force, it is better to neglect it [21]. Also, the worst-case scenario is considered when this assumption is used. The soil does deliver the vertical force to counter the weight of the monopile, and it restricts the monopile's translation. Only small rotations about the x-, and y-axis of monopile's earth-fixed reference system are allowed. In aNySIM, this is modelled by using a joint connected to the bottom of the monopile, located precisely at the monopile's earth-fixed reference system. The joint contains very high linear damping and spring coefficients for surge, sway, heave, and yaw direction. A minimal translation or rotation over the z-axis results in a force or moment that brings the bottom of the monopile back at its original position, except for the rotation around the x- and y-axis. The model of the monopile is a stiff system due to the high damping and spring coefficient of the joint. A small time step of 0.02 seconds is chosen to avoid numerical issues in aNySIM as results of the stiff system,

4-4-3 Installation location

For the monopile installation, it is important to determine the optimal monopile's position relative to the vessel. This subsection explains where the monopile is located and why this is the preferable position. For the determination of this position, it is essential to know the position of the main crane. The main crane is located at [-34.24,-13] in the global reference system. The main crane can use its maximum lifting capacity between the radii of 13.5 and

20 m relative to this position. The more the monopile's position is near the CoG of the vessel, the less influence the pitch and roll motion have on the location of the vibro-drill and gripper. Thus, the monopile is positioned as far as possible in positive x-, and y-direction and within the 20 m of the crane's centre to stay within the maximum lifting capacity. First, the minimum y-distance to the vessel's hull is determined. The motion-compensated gripper can compensate for 3 m of horizontal displacement. Considering enough space for the gripper's envelope and 1 m for safety reasons, the minimum distance from the monopile to the ship's port side is 4 meters. Adding half of the monopile's diameter of 10 m, the monopile's centre is at -9 m relative to the hull. The hull at the port side of the vessel is positioned at -18 m. Thus the monopile will be installed at -27 m in the y-direction. Keeping in mind that the monopile's position should be within 20 m of the crane's centre and placing the monopile maximum forwardly, the monopile is positioned at [-20.24,-27] in the global reference system. This is visualised in figure 4-16.

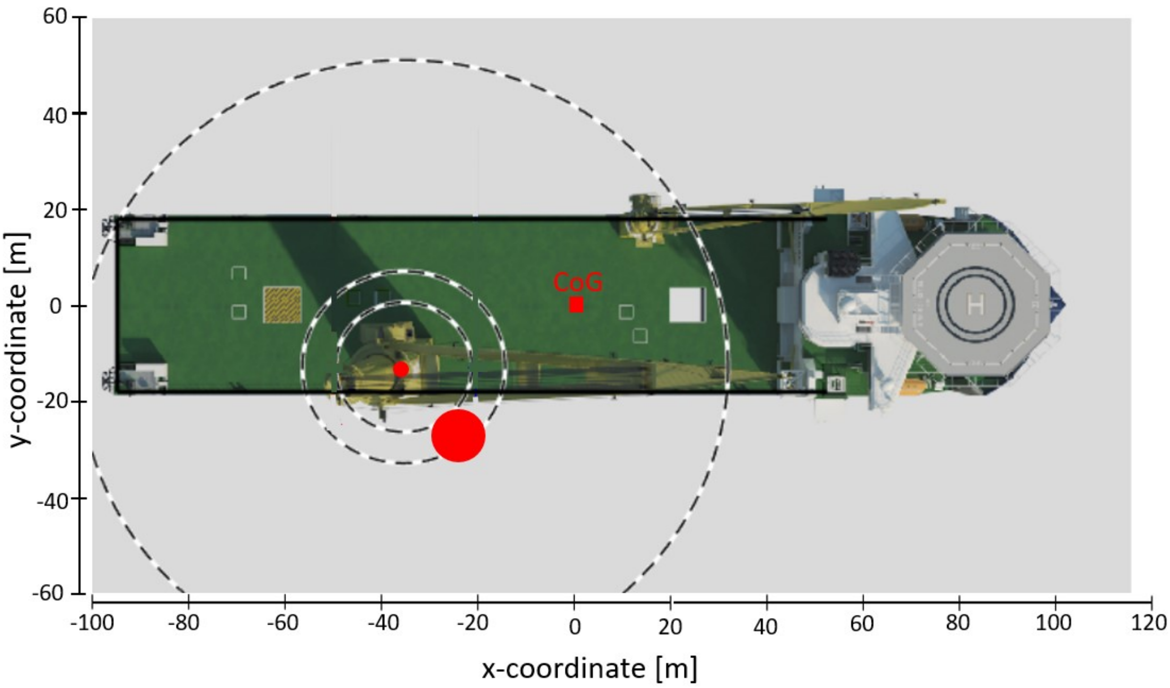

Figure 4-16: Monopile's position relative to the vessel's position

4-4-4 Environmental forces on monopile

The environmental forces that act on the monopile will result in monopile rotation. The gripper tries to counter the environmental forces and keeps the monopile as vertical as possible to avoid a too large inclination angle. For the determination of the workability, the environmental forces must be modelled correctly. This section explains how this is done.

Wave forces with diffraction calculation vs Morison equation As explained in section 4-1-1, two diffraction calculations are executed for the monopile in Ansys AQWA. One calculation does consider the shielding effect, and the other does not. Unfortunately, there is no diffraction calculation available to verify the diffraction calculation made in Ansys AQWA. In subsection 3-1-2 it is explained that the wave force on a monopile can also be calculated with the Morison equation. One of the crucial RAO's of the diffraction calculation is the force RAO in surge direction with an incoming wave angle of 180 degrees. To verify the diffraction calculation, this force RAO is calculated with the Morison equation in Excel. The Morison equation is shown in equation 3-2, it contains a drag and an inertia force. This equation can only be used for slender structures. A cylindrical structure can be called slender when the diameter divided by the wavelength is smaller than 0.2 [12]. In figure 4-17, the slenderness ratio versus wave period is shown. The scatter diagrams of the North-Sea, shown in Appendix D, shows that waves with wave periods between the 2 and 14 seconds occur in the North-Sea. The study of [1] shows that only waves with wave periods larger than 6 seconds will influence the workability of the 'Stella-Synergy'. The structure can be called slender, and the Morison equation shown in 3-2 can be used when only these waves are considered.

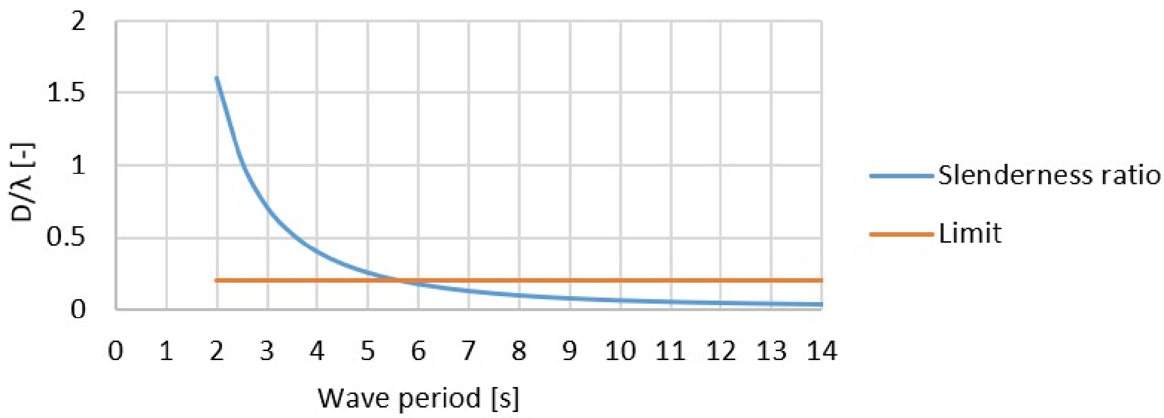

Figure 4-17: Slenderness-ratio

The Keulegan-Carpenter (KC)-number describes if the drag or the inertia part of the Morison equation is dominant [46]. When the KC-number is lower than 3, the inertia part is dominant. Using the extreme values of the scatter diagram of Appendix D and filling these in into equation 4-12, the larges water particle velocity occurring in the North Sea is calculated. Filling in this particle velocity in equation 4-11 results in a KC-number of 1.8. This means that for all the sea conditions in the North Sea, the inertia force on the monopile is dominant in the Morison equation.

$$KC = \frac{u \cdot T}{D_0} \tag{4-11}$$

Although the drag force on the monopile is not important according to the KC-number, the drag force is still calculated for validation. The water particle velocity and acceleration are needed in the Morison equation, but they vary in the water depth. Therefore, the monopile is split up into slices with a height of 0.5 m. For each slice, the drag and inertia force is calculated. The data-points for the force RAO are calculated following the next steps:

- Choose a wave frequency between 0.1 and 1.6 rad/s and a logical wave height. For each wave frequency in this range with step sizes of 0.1 rad/s, the calculation is made.

- Calculate for the chosen wave frequency the wave number k and the wavelength with the dispersion relation, shown in equation 3-1.

- Calculate the amplitude of the wave-particle velocity and acceleration in the middle of the slice with equations 4-12 and 4-13 [46]. The last part of these equations, comprising the sin and cos function, must be removed to calculate the amplitude of wave-particle velocity and acceleration.

$$u = \omega \cdot a \cdot \frac{\cosh(k \cdot (z+h))}{\sinh(k \cdot h)} \cdot \cos(kx - \omega t) \tag{4-12}$$

$$\dot{u} = -\omega^2 \cdot a \cdot \frac{\cosh(k \cdot (z+h))}{\sinh(k \cdot h)} \cdot \sin(kx - \omega t) \tag{4-13}$$

- Determine the drag and inertia coefficients C_D and C_M. For the determination of the drag coefficient, the focus lays on a wave with a wave height of 3.0 m and a period of 9.0 s, in section 4-3-4 is explained why the focus lies here. The average particle velocity amplitude is calculated for the upper 10 m of the monopile's submerged part for this wave. Approximately 70% of the drag force on the monopile acts at the upper 10 m, so the focus lies here. This particle velocity is used to calculate the Reynolds number, which is $4.4 \cdot 10^6$. Using this Reynolds number while zooming in into figure 4-18 results in a drag coefficient of approximately 0.68. This drag coefficient is assumed to be constant over wave frequency. The inertia coefficient C_M is read from figure 4-19, it is dependent on the slenderness ratio. For each wave frequency, a new inertia coefficient is determined.

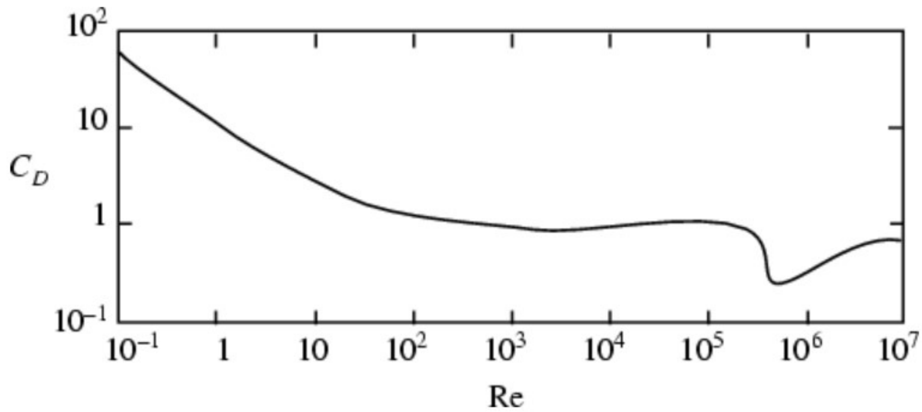

Figure 4-18: Drag-coefficient of a cylinder [2]

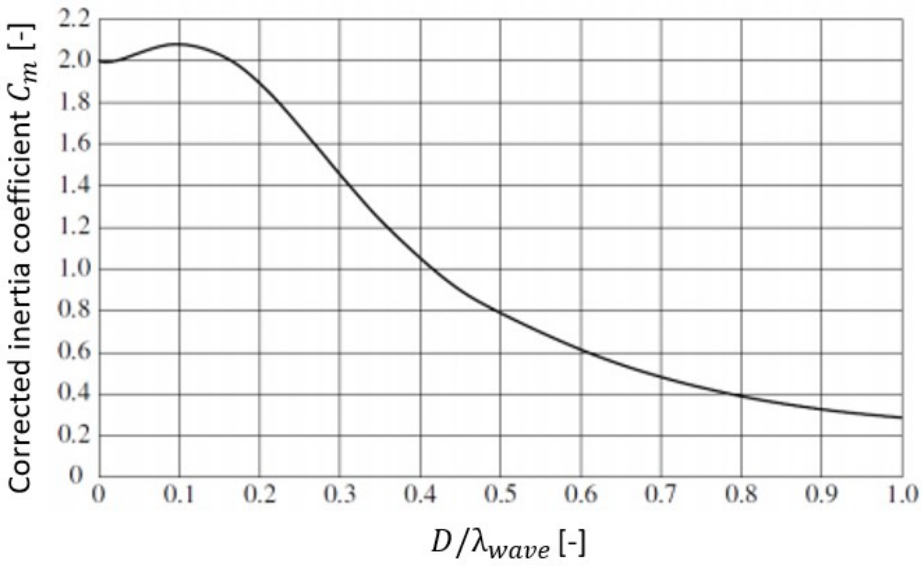

Figure 4-19: Inertia-coefficient of a cylinder [3]

- The last step is to fill in the Morison equation. For each frequency step, the drag and inertia force are calculated per slice. The total drag and inertia force that acts at the monopile are calculated by adding the the forces per slice. For each wave condition, the inertia force is indeed much larger than the drag force. Still, the combined drag and inertia force is considered for calculating the data-points of the force RAO for surge. The RAO-values are calculated with equation 4-14, with a is the wave amplitude.

$$RAO_{surge} = \frac{\sqrt{F_{drag}^2 + F_{inertia}^2}}{a} \tag{4-14}$$

A single data-point of the force RAO for surge is determined for one particular wave frequency when all the steps are following once. A force RAO curve is made when these steps are executed multiple times for a varying frequency. The final result is compared with the force RAO calculated in Ansys AQWA, and this is shown in figure 4-20. The minor differences between the curves could arise due to a relative big wave frequency timestep of 0.1 rad/s or a relative big monopile slice height of 0.5 m. Another reason might be that the monopile could not be considered a slender structure for waves with a wave period of less than 5.5 seconds. Converted this wave period into a wave frequency, the monopile is not slender for wave frequencies larger than 1.1 rad/s. Therefore, the result of the Morison equation could be less accurate for frequencies larger than 1.1 rad/s. Overall, the force RAO's are very similar and thereby is the force RAO for surge calculated by Ansys AQWA verified. Since this part of the diffraction calculation is verified, it is assumed that the two full diffraction calculation for the monopile are correct.

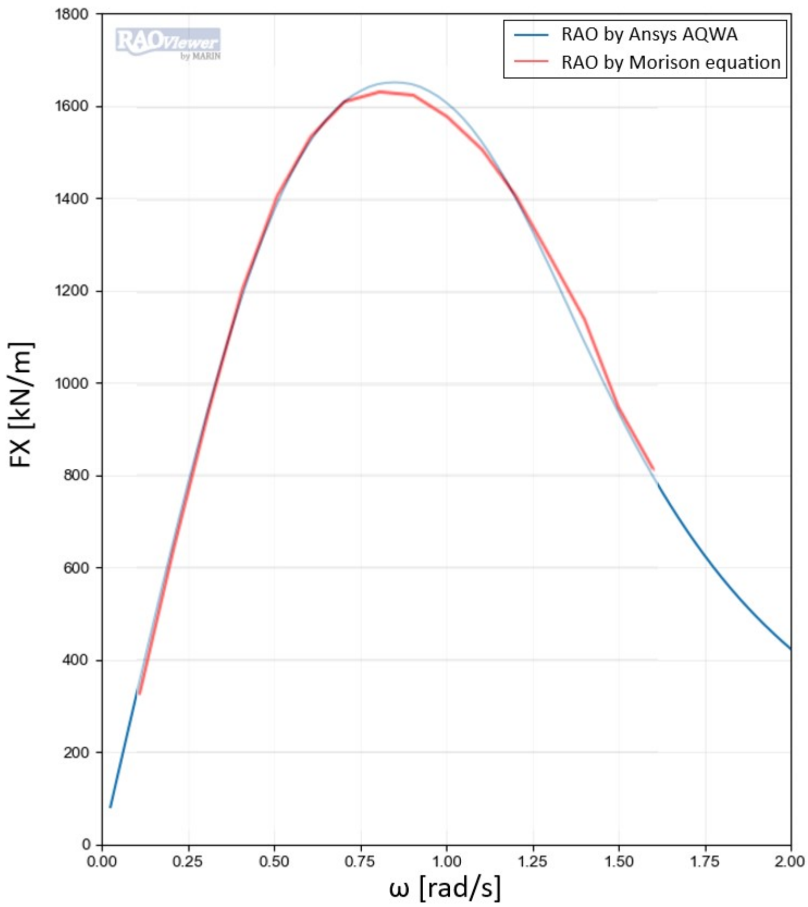

Figure 4-20: Force RAO's for surge, Morison equation vs Ansys AQWA calculation

Shielding effect In the last paragraph is concluded that the two diffraction calculations for the monopile are correct. The diffraction calculation that considers the shielding effect is implemented in the model, the calculation which does not consider the shielding effect is purely done to compare with. Comparing these diffraction calculations is done in this paragraph. Remember that the added mass and damping matrices are full of zeros because the monopile's motion is assumed to be frozen during the diffraction calculations. The contour plots of the force RAO's in x- and y-direction are shown in figure 4-21 and 4-22. A contour plot shows the RAO-values over varying wave frequency and incoming angle of attack. A clear overview of the incoming wave angle is shown in figure 2-3.

The contour plot for the monopile without the shielding effect is generated by doing a diffraction calculation for the solely monopile. This means that only a cylindrical structure is considered and that the ship is not included. The monopile is symmetric across the x- and y-axis. This means that the contour plot for x- and y-direction must be similar, only shifted 90 degrees. This is clearly visible in the left part of figures 4-21 and 4-22. The contour plots for x- and y-direction contain two oval-shaped contour peaks, which are shifted 90 degrees. The peaks are located at a frequency of 0.85 rad/s.

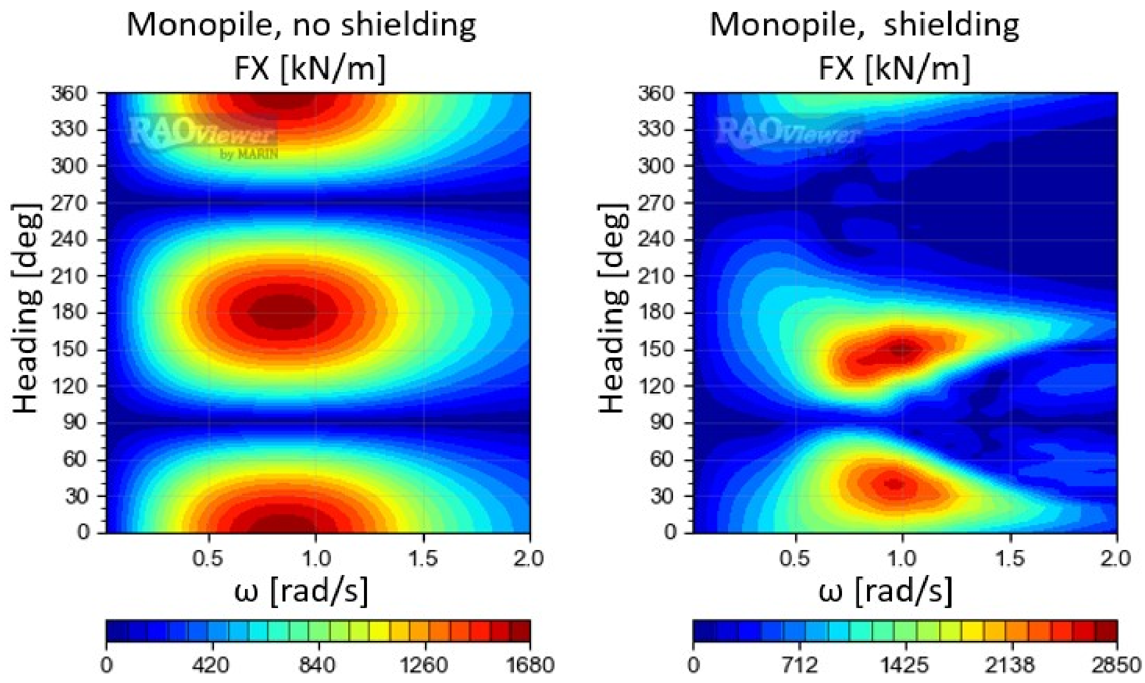

Figure 4-21: Contour plot of force RAO's in x-direction

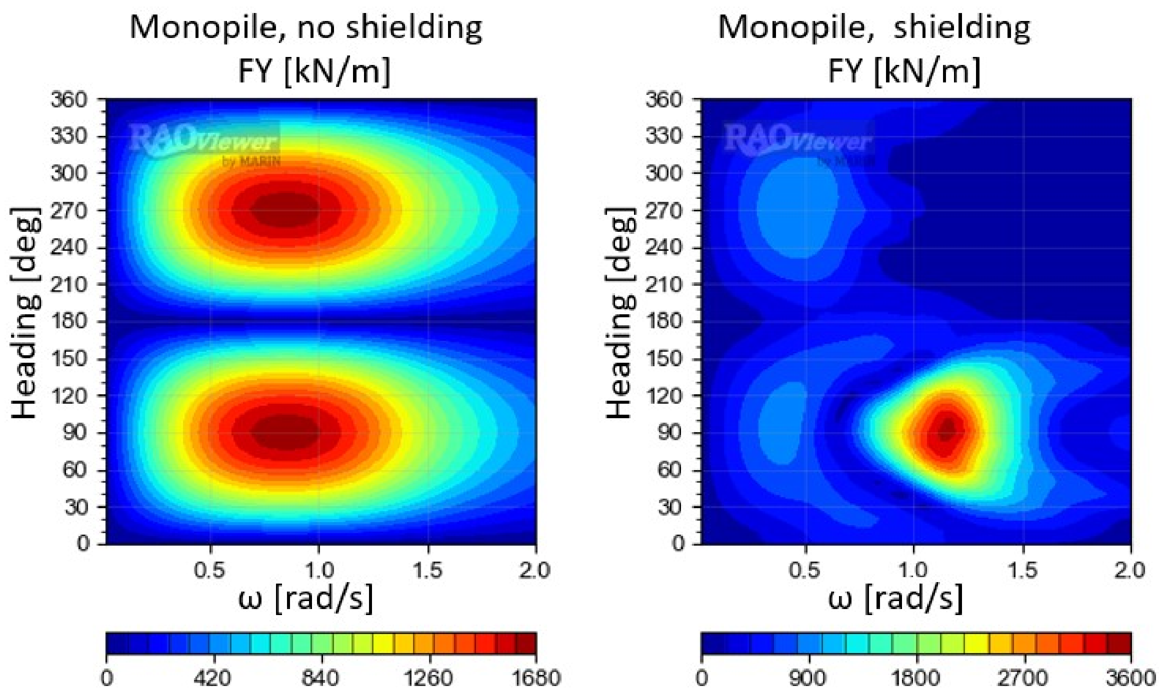

Figure 4-22: Contour plot of force RAO's in y-direction

The contour plots with shielding compared with the contour plots without shielding shows three important differences. The forces on the monopile for waves with incoming angles between 180-360 degrees are much lower for the plot that considers the shielding effect. This is obviously because the waves diffract at the vessel's hull and will never hit the monopile. The vessel protects the monopile by diffracting the waves. Another difference is that the wave forces with an incoming angle between 0-180 degrees are much higher when the shielding effect is considered. This is due to the waves that hit the monopile directly, without having the vessel in front of it, and due to the diffracted waves of the vessel that hit the monopile too. The last difference is that the contour peak shifts to a slightly higher frequency for waves with an incoming angle between 0-180 degrees. Probably, this is because the waves that hit directly the monopile and the diffracted waves that hit the monopile add up for frequencies near the 1.0 rad/s.

For the calculation of the shielding factor for a particular incoming angle, the maximum combined force RAO for x- and y-direction on the monopile is calculated. This is done by taking the root of the summed squares of the RAO-values. This is calculated for the RAO's with and without the shielding effect. Dividing the maximum combined RAO-value with shielding by the maximum combined RAO-value without shielding gives the shielding factor. The shielding factor is calculated for each incoming angle of attack, and the results are shown in figure 4-23. It shows that the shielding factor is minimal for waves with incoming angles between 210-310 degrees. Thus, the monopile is protected maximally by the vessel for those incoming angles. If the governing limitation of the model is related to the force on the monopile, the preferable incoming angle would be between 210-310 degrees. In section 5-2-3 is explained what the governing limitation is and why the preferable angle is 180 degrees, although the shielding factor is not minimal with this angle.

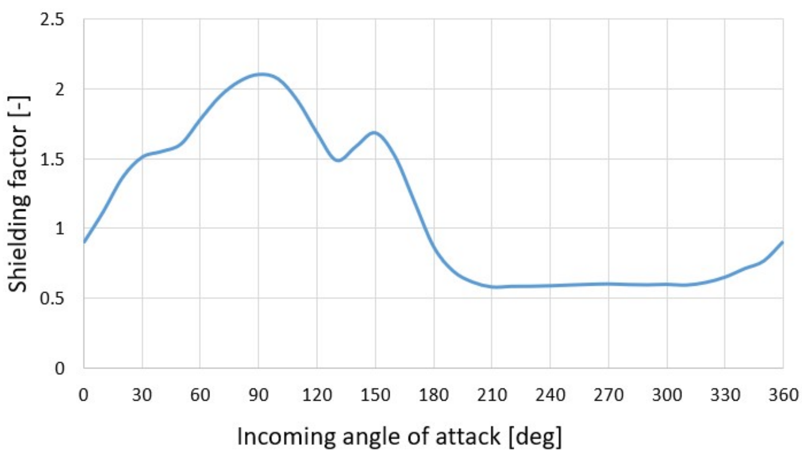

Figure 4-23: Shielding factor over incoming angle of attack

Wind and current forces Not only wave forces act on the monopile, but also wind and current forces. The wind and the current coefficient for the monopile are not tested in a wind tunnel or a water basin. Therefore, the maximum wind and current coefficient are determined with figure 4-18. For the calculation of the Reynolds number, sea conditions with a H_s of 3.0 m, a T_p of 9 s, and a U_{10} of 13.5 m/s are used. In section 4-3-4 is explained why the focus lies on these conditions. The maximum current and wind coefficients in a particular direction are respectively 0.68 and 0.70. A curve for the wind and current coefficients over the incoming angle is made with a sinus function, with the maximum coefficients used as amplitude. This curve shows how the wind coefficients are divided over x- and y-direction, in figure 4-24 is shown how this is done. The wind and current peaks in x- and y-direction are 90 degrees out of phase. The calculated wind and current coefficients for the monopile can be found in C-2. The moment around the z-axis due to the wind and the current is assumed to be zero.

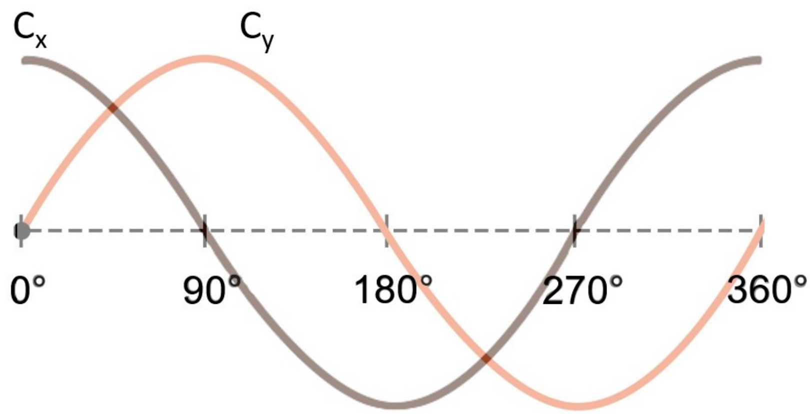

Figure 4-24: Sinus-function for determination of monopile's wind and current coefficient

Just as for the vessel, the current and wind forces on the monopile are measured in aNySIM and verified with equation 3-4. The results are identical and thereby verified. Notice that the shielding effect for the wind and current forces is not considered. Although it will not significantly influence the model, considering the shielding effect would be more accurate.

4-5 Motion-compensated pile gripper

The DP-system is the used station-keeping system during the installation activities. It tries to minimize the motion of the vessel, but small vessel motions will always be present. A motion-compensated pile gripper is needed to compensate for these motions and to keep the monopile vertical. As concluded in subsections 2-1-4 and 2-1-3, the maximum accepted inclination angle during installation depends on the monopile's penetration depth, and the maximum inclination angle at delivery depends on the transition piece connection. Just as in the research of [1], the maximum accepted inclination angle in this model is assumed to be 0.5 deg. The gripper contains two PID-controllers; one is used to determine the force to counter the vessel's motion, the other is used to determine the force to keep the monopile vertical. This section explains how the PID-controllers work, how the gripper is built step by step, and how is dealt with a numerical problem. At the end of the section, the limitations of the gripper's capabilities are discussed.

4-5-1 P(I)D-controllers

The two PID-controllers, which are used for the motion-compensated gripper, are used for different purposes, but they are built the same way. Each controller contains a proportional, an integral, and a derivative gain. A PID-controllers needs a goal as input, which is called the setpoint. For these PID-controllers, the setpoints are the desired position of the gripper and the monopile. For each simulation step, the current positions are sent from aNySIM to the PID-controller in Python. Each controller calculates an output value based on the current and previous error between the real position and the setpoint. For these PID-controllers, the output value is multiplied by a factor to calculate the required force. The factor is determined based on the mass that has to be displaced. The factor could be replaced by multiplying the gains of the PID-controller by this factor. The output value is calculated with equations 4-15 and 4-16.

$$P_{term} = error \qquad I_{term} += error \cdot \Delta t \qquad D_{term} = \frac{\Delta error}{\Delta t} \tag{4-15}$$

$$Output = P_{gain} \cdot P_{term} + I_{gain} \cdot I_{term} + D_{gain} \cdot D_{term} \tag{4-16}$$

The proportional term is the error between the setpoint and the measured position. The goal of the proportional term is to give a response linear to the error, to avoid large offsets between the desired and the current position. The integral term is the accumulation of all the previous errors. The goal of the integral term is to keep the average value of the error close to zero. In the next section is explained that the setpoints of the PID-controllers change for each timestep, and therefore the integral term is of minor importance. The integral term is even set to zero, which results in that the controller should be called a Proportional Derivative (PD)-controller. The goal of the derivative term is to avoid a large overshoot. The derivative term does this by calculation the delta error, which is the difference between the last and the current error. Finally, the proportional, the integral, and the derivative terms are multiplied by their gains and added to give the output value. The PD-controllers are tuned based on an iterative way until they respond fast and accurately.

4-5-2 Model of the gripper and force equilibria

The motion-compensated gripper of Huisman Equipment B.V., shown in figure 4-25, will be installed at the Stella-Synergy. According to Huisman Equipment B.V., the gripper contains two parts. Both parts move for a translation in the x-direction, and only one part moves for a translation in the y-direction. The total weight of the gripper is approximately 1500 tonnes. This gripper is modelled as correctly as possible to give accurate results. Some limitations about the gripper are explained in subsection 4-5-4. This section explains how the gripper is built in Python and aNySIM step by step.

Figure 4-25: Motion-compensated pile gripper of Huisman Equipment B.V.

The steps below are taken to build the motion-compensated gripper. In these steps, the focus lies on the y-direction. All the steps are similar for the x-direction.

Step 1 Build a third body in aNySIM with a weight of 1500 tonnes, which represents the gripper. Although the real gripper consists of two different parts, the gripper in aNySIM consists of only one body: Body 3. In reality, the gripper is connected with the vessel, and hydraulic cylinders move the two parts. This is hard to model in aNySIM. Therefore the gripper is represented by a single body that is free to move relative to the vessel. The following steps explain how the gripper is modelled to respond similarly to the real gripper. It is assumed that Body 3 can translate in x- and y-direction. The other motions are neglected. The gripper is placed at an elevation of 11.468 m above sea level, and this is shown in figure 4-26.

Step 2 Measure the position of the center of the monopile at the gripper's elevation height. The monopile will move due to the environmental forces that act on it. The measured position will be controlled, depending on this position, the inclination angle of the monopile can be determined.

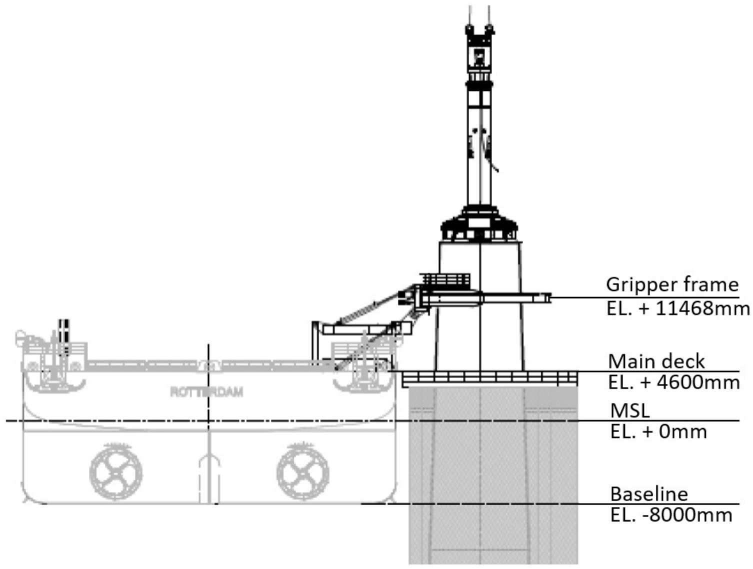

Figure 4-26: Gripper's elevation

Step 3 Use and tune a PD-controller to determine the force to keep the monopile as vertical as possible This force is called FY_{PD1}. The setpoint of the PD-controller is the position of the centre of the gripper. At this phase, it is also assumed that the gripper counters the vessel's motion perfectly and is positioned precisely at the desired location. The next steps explain how to calculate the gripper's location and that it is not constantly at the desired location. Although the gripper of Huisman Equipment B.V. has four contact points on the monopile, it is assumed that the gripper entirely acts the calculated force at the centre of the monopile. The force to keep the monopile vertical is shown in equation 4-17.

$$FY_{mono} = FY_{PD1} \tag{4-17}$$

Step 4 The gripper is attached to the vessel and moves along with it. At the same time, the hydraulic cylinders of the gripper move the centre of the gripper relative to the vessel and try to keep the centre of the gripper at the same position in the global reference system. In aNySIM, this is hard to model. When an extra body is added which is connected to the vessel, it cannot move it relative to the vessel. When an extra body is added which freely moves, it will not move along with the vessel. Therefore, a fourth body, which freely moves, is added in aNySIM. This body is purely build to do some calculation with, and it does not represent a specific element of the model. Just as Body 3, Body 4 weighs 1500 tonnes and can only translate in x- and y-direction. The position of this body is measured. In steps 5, 6, and 7 is explained how this body is used to model the gripper.

Step 5 Measure the position of the vessel at the gripper's location. It is essential to measure the position at this location instead of at the CoG of the vessel because the vessel's roll, pitch, and yaw motion will influence the position at the gripper's location.

Step 6 Use and tune a second PD-controller to determine the force to counter the vessel's motion at the gripper's location with Body 4. This means, for example, if the vessel moves 1 m in positive y-direction, the PD-controller determines the force to move Body 4 1 m in the negative y-direction. The setpoint of this controller is calculated by equation 4-18, and the calculated force to move Body 4 is shown in equation 4-19. The setpoint of the second controller is the original position of Body 4 minus the translation of the vessel at the gripper's location. Because the setpoint changes over time, the integral gain is set to zero. Therefore, the controller is called a PD-controller instead of a PID-controller.

$$SetpointY_{C2} = OriPosY_4 - (PosY_1 - OriPosY_1) \tag{4-18}$$

$$FY_{gripper} = FY_{PD2} \tag{4-19}$$

Step 7 Calculate the ability of Body 4 to counter the vessel's motion, and determine the gripper's location. How this is done is shown in equation 4-20. The summation of the vessel's offset to its original position and the offset of Body 4 to its original position plus the original position of Body 3 gives the position of Body 3. For example, if the vessel moves 1 m in positive y-direction, and Body 4 moves 0.9 m in the negative y-direction, the gripper moves 0.1 in the positive y-direction. For this example, this means that the gripper counters the vessel's motion by 90%. The inertia of mass of Body 4 is the main reason why the vessel's motion is not countered perfectly. Figure 4-27 shows an example of the y-position of the vessel, Body 4, and the gripper during the first 40 seconds of a simulation. The gripper's position still moves, but most of the vessel's motion is compensated.

$$PosY_3 = (PosY_1 - OriPosY_1) + (PosY_4 - OriPosY_4) + OriPosY_3 \tag{4-20}$$

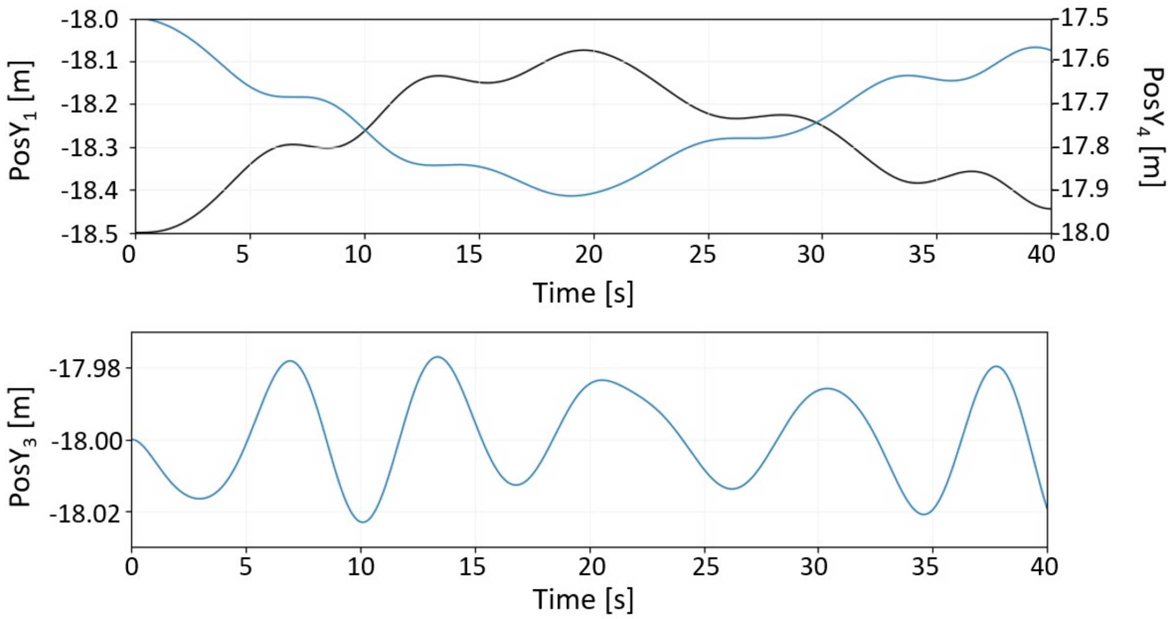

Figure 4-27: Upper: y-position of the vessel (blue) and Body 4 (black).
Lower: y-position of the gripper

Step 8 Use the gripper's location as a setpoint of the first PD-controller. The gripper tries to keep the monopile precisely in the centre of the moving gripper arms. Although this results in larger monopile's motions, it imitates the real gripper more accurate. Because the setpoint changes over time, the integral term is set to zero, and the controller is called a PD-controller. The setpoint of this controller is shown in equation 4-21.

$$SetpointY_{C1} = PosY_3 \tag{4-21}$$

Step 9 The force that the gripper acts at the monopile, FY_{mono}, also acts at the gripper in the opposite direction. This force is added to Body 4. This means, for example, if the gripper tries to move the monopile in the positive x-direction, the gripper will move unintentionally in the negative y-direction. To counter this, the force to move the gripper, $FY_{gripper}$, is raised with the force to move the gripper. This is shown in equation 4-22.

$$FY_{gripper} = FY_{PD2} + FY_{mono} \tag{4-22}$$

Step 10 Add the friction forces of the gripper. The friction forces of the gripper of Huisman Equipment B.V. in the x- and y-direction are respectively 120 mt and 100 mt. Since the gripper in aNySIM consists of only one body that moves in x- and y-direction, the gripper forces are assumed to be 120 mt in both directions. The static friction is assumed to be equal to the dynamic friction. The friction force acts in the opposite direction of the velocity of Body 4. When Body 4 is not moving, the friction force is equal to the opposite of the summed forces on Body 4, with 120 mt as maximum. Thus, the body starts to move only if the summed forces on Body 4 are larger than 120 mt. Again, this means that the required force to move Body 4, $FY_{gripper}$, is adapted. Multiple situations arise now. Depending on the sign of calculated force to move Body 4, FY_{PD2}, and the velocity direction of Body 4, the friction force is added to or subtracted from the calculated force to move Body 4, $FY_{gripper}$. In picture 4-28, for one situation, the forces are sketched. Remember that some of the force can change direction in other scenario's.

Step 11 The calculated forces to move the gripper and the monopile can vary enormously in a single timestep. If, for example, the force calculated by the second PD-controller, FY_{PD2}, changes direction, and the velocity of the gripper changes direction too, the force to move the gripper can change enormously in a single timestep. The hydraulic cylinders need some time to build up their force due to dynamic pressure build-up and cannot follow the desired force directly. Therefore, a maximum force build-up is modelled in Python. This is modelled by setting a maximum force increment and decrement between 2 timesteps for $FY_{gripper}$ and FY_{mono}. The hydraulic cylinders are assumed to go from 0 to maximum force in 1 second. Sometimes, this results in a difference between requested and delivered force.

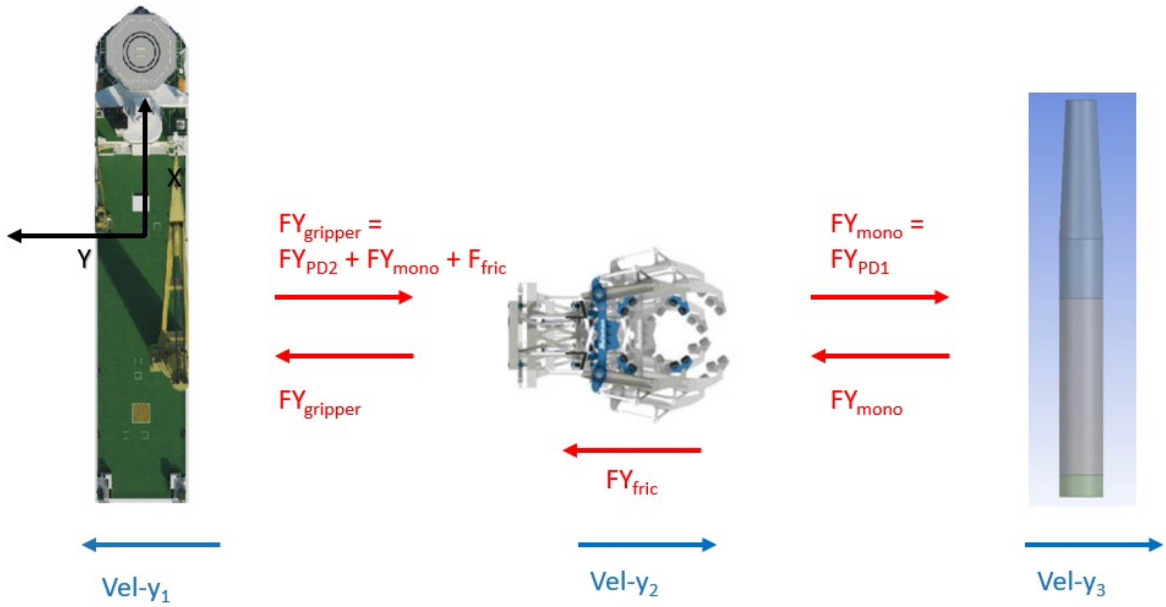

Figure 4-28: Forces overview on gripper in y-direction,
Situation: positive velocity-y vessel, negative velocity-y Body 4 and monopile, negative FY_{PD1} and FY_{PD2}

Step 12 Add the force of the gripper that acts on the vessel. As visualised in figure 4-28, the force to move the gripper acts in the opposite direction on the vessel. It is assumed that the location of the gripper does not influence the CoG of the vessel. Thus, force in z-direction due to the weight of the gripper is not considered. The roll, pitch, and yaw moments caused by $FY_{gripper}$ are considered. In section 5-2-5, is explained which influence the gripper has on the vessel's motion.

4-5-3 Numerical problem

The last subsection explained how the motion-compensated gripper is modelled in aNySIM and Python. Unfortunately, a numerical problem arose after the gripper is implemented. This section explains why this problem does not arise at the real gripper, what the numerical problem exactly is, and how is dealt with the problem.

Problem description When the control system of the real gripper decides that the gripper's velocity in x- or y-direction should change direction, the gripper decelerates until the gripper reaches zero velocity. Then the gripper accelerates in the other direction. This could take some time because the friction force changes direction too and should be overcome. The gripper starts to move only when the combined forces on the gripper are larger than the friction force. Before the gripper starts to move in the new direction, the gripper has automatically zero velocity for a short while. Keep in mind that the velocity here is the relative velocity to the vessel.

Unfortunately, in aNySIM, something different happens when the relative velocity to the vessel changes direction. When for example, the velocity in the y-direction is positive and decreases to almost zero, the velocity could be directly negative in the next timestep. It skips the zero velocity phase. In this phase, the force needs to be built up in the negative direction to overcome the friction force, which points now in the positive direction. In the next timestep, the gripper's velocity-y is negative, which results in a large friction force in the positive direction. The friction force causes a positive gripper's velocity again. Finally, this results in a situation where the friction force and gripper's velocity change direction every timestep, which is far from reality. The first 50 seconds of a simulation with this numerical problem is shown in figure 4-29.

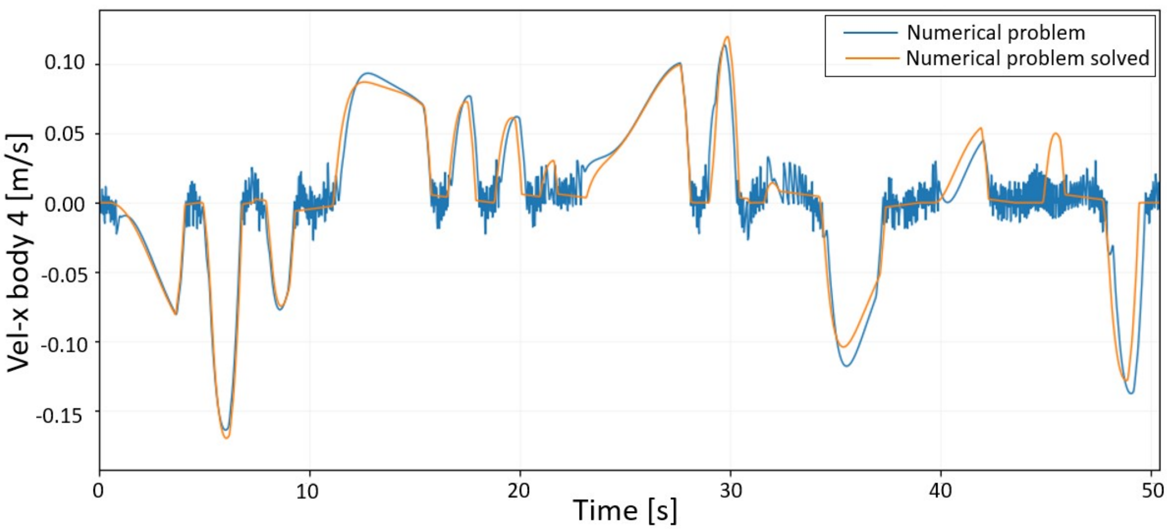

Figure 4-29: Numerical problem of gripper, shown for the velocity in x-direction of Body 4

The solution to the numerical problem An extra condition and an extra force for x- and y- direction are added to the gripper's model to solve this numerical problem. When the combined forces on the gripper are lower than the maximum friction force and the velocity of Body 4 is lower than a particular threshold value, Body 4 is forced to act like it has zero velocity. This is reached by bringing the total forces in equilibrium, and adding an extra force afterwards, FX_{zero} or FY_{zero}. The forces are in equilibrium by the friction force, which counters the other forces in this situation. This differs from the previous situation, where the friction force was always maximum when Body 4 has even the smallest velocity. The arbitrary chosen extra force will cause, slowly, a zero velocity for Body 4, while the other forces are in equilibrium. The velocity of Body 4 does not jump uncontrolled across the zero velocity line anymore, and the numerical problem is solved. The threshold velocity, Vel_{min}, is +/-0.009 m/s, which is 1.5% of the maximum allowed gripper's velocity for both directions. Using this value solves the numeric problem for all simulations. Due to the use of this trick to solve the numerical problem, the velocity of Body 4 is not modelled correctly when it is below the threshold value. But, simulations containing the numerical problem are even further from reality. Therefore, this trick to solve the numerical problem is used for all simulations. The difference between a simulation using this solution to the numerical problem and a simulation without using it is shown in figure 4-29.

$$
\begin{aligned}
if : abs(FX_{gripper} - FX_{mono}) < & FX_{fric\_max} \quad \text{and} \quad abs(VelX_4) < VelX_{min} : \\
& FX_{fric} = FX_{mono} - FX_{gripper} \\
& FX_{zero} = -/+3000 \quad [N]
\end{aligned} \tag{4-23}
$$

4-5-4 Gripper's limitations and capability

The gripper of Huisman Equipment B.V. has some limitations in terms of maximum forces and velocity. The maximum force to move the monopile is 4.91 MN, and the maximum forces to move the gripper in x- and y-direction are both 3.43 MN. These limits are considered in aNySIM and can not be exceeded. Another limitation of the gripper is the gripper's velocity relative to the vessel, which is maximum 0.6 m/s in both directions. This limit is not considered in the model, and when the maximum velocity is exceeded, the simulation is assumed to be not workable.

The results of simulations with a constant significant wave height and a varying wave peak period are compared to measure the motion-compensation capability of the gripper. The chosen significant wave height is 1.25 m, and the peak period varies from 3.5 s to 13.5 s. In section 5-2-2 will be concluded that all these conditions are workable for the Stella Synergy. For those simulations, the average offset of the vessel and gripper from their original positions are compared. The first 200 seconds are removed from the simulation to remove the start-up problems of the simulations. The gripper's average motion compensation in x- and y-direction are shown in figure 4-30 and 4-31. Additionally, the gripper's capability is tested for simulations with a constant wave peak period of 8.5 s and a varying significant wave height from 0.75 m to 4.75 m. Those results are shown in Appendix G.

A clear relation between the gripper's average offset and the vessel's average offset is shown in the graphs. Therefore, the percentage of motion compensation is also shown in figures 4-30, 4-31, G-1, and G-2. For all the tested simulations, the gripper compensates the vessel's motion for 65% to 95%. This range is substantial. Thus the gripper's ability to compensate the vessel's motions depends on the sea condition it is operating in. No direct relation between the vessel's average offset and the percentage of motion compensation is visible. Therefore, it can not be concluded if the gripper is operating better in low or high states in general. Still, zooming in into the high sea states is interesting. These sea conditions contain a large wave peak period or large significant wave height. The gripper is better capable of compensating the vessel's motion for waves with a large wave period than for waves with a large significant wave height. Probably, this is because waves with a large peak period will cause the vessel to move slowly, and there is enough time for the gripper to react. In contrast, there is less time to react for waves with a large significant wave height and a lower wave peak period.

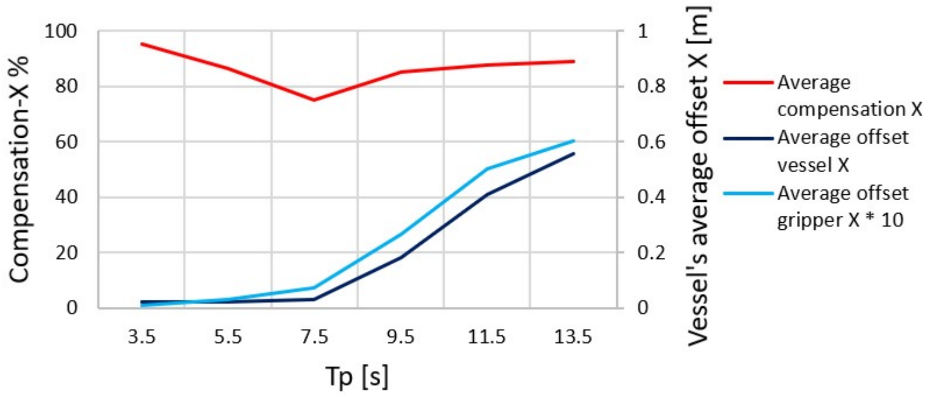

Figure 4-30: Gripper's motion compensation in x-direction with varying Tp for Hs=1.25 m

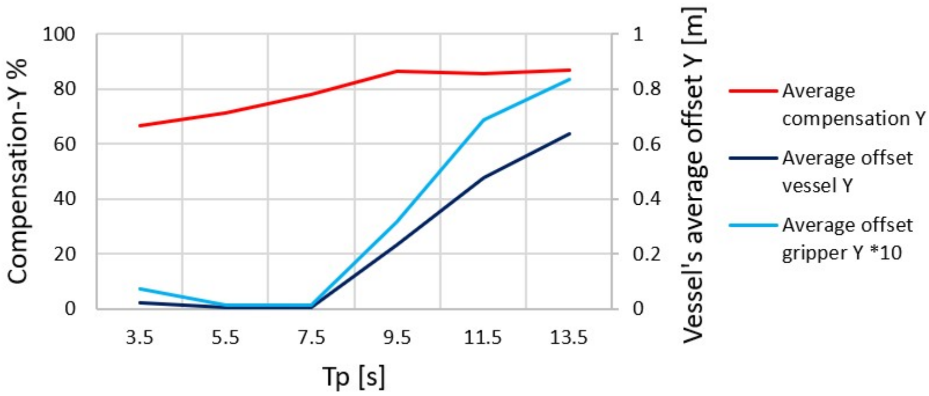

Figure 4-31: Gripper's motion compensation in y-direction with varying Tp for Hs=1.25 m

In the report of [19] it is concluded that their motion-compensated pile gripper is cable to compensate 95 % of vessel's motion up to a significant wave height of 2.5 m. Unfortunately, the gripper used in this model has a lower motion compensation percentage. Although the gripper's motion compensation percentage is lower, it can be concluded that the modelled gripper compensates most of the vessel's motion during all tested simulations. The influence the gripper and the monopile have on the vessel's motion is explained in section 5-2-5.

Chapter 5

Simulations and results

The previous chapter explains step by step how the model is built up and verified. The model contains a good representation of the vessel, the monopile, the gripper, and their environmental forces. After verification of every element of the model, simulations are run to generate results. This chapter explains the limitations of the model and how the workability of the vessel is calculated. Before calculating the workability, the preferable angle of attack of the environmental conditions is determined. Additionally, simulations are run for specific situations to investigate whether it is possible to increase the vessel's workability or reduce its footprint. Finally, the monopile's influence on the vessel's motion and the effect of the worst-case single on the vessel's workability is researched.

5-1 Limitations for the workability

The results of each simulation are checked to determine if the simulation is workable. There are several limitations for each simulation. When one or more limitations is exceeded during a simulation, the simulation is determined to be non-workable. The simulations are tested by six limitations, which are described in this section and are shown in table 5-1.

Vessel's footprint The gripper can compensate the vessel's motion for maximum +/- 3 m in x- and y-direction. Besides the vessel's translational motions, the rotational motions will also cause translational motions at the gripper's location. Therefore, the footprint of the vessel at the gripper's position is considered. At the gripper's position, the maximum allowed footprint is +/- 3 m in x- and y-direction.

Roll and pitch angle The first step of the early pile driving phase is to lift the vibro drill on top of the monopile. The weight of the vibro-drill is 2000 tonnes, which is just below the maximum crane capacity. During such a heavy lift operation, the roll and pitch motion of the vessel must not become too large to avoid a swinging motion of the vibro drill and maintain the maximum lifting capacity of the main crane. Therefore, the maximum allowed roll and pitch angle of the vessel is 1.5 degrees.

Monopile's inclination angle Plastic deformation of the soil near the monopile must be avoided during the installation of the monopile. The stability force to keep the monopile upright could be reduced when the soil near the monopile is plastically deformed. This could lead to an unstable situation during the lifetime of the monopile. Also, the inclination angle at delivery is limited to ensure the vertically of the transition piece and the tower. When the tower is inclined, a large moment could arise due to the gravitation force of the wind turbine. In this research, the maximum allowed inclination angle is 0.5 degrees.

Gripper's velocity The maximum velocity of the gripper produced by Huisman Equipment B.V. is 0.6 m/s in x- and y-direction. This limitation is not considered in the gripper's model, and therefore it is included as a limitation for the workability.

Table 5-1: Limitations of the model

Limitations:	Magnitude	Units
Footprint-x	3.0	m
Footprint-y	3.0	m
Roll angle	1.5	deg
Pitch angle	1.5	deg
Inclination angle	0.50	deg
Velocity gripper x/y	0.60	m/s

5-2 Simulations

Many simulations are run to generate results. The simulations should have a duration of at least of 3-hours [12] to achieve stationary irregular wave conditions. The start-up problems of a simulation could take approximately 200 seconds, and therefore the chosen duration of a simulation is 11000 seconds. In the simulations, the wind, the waves, and the current are assumed to be collinear, meaning that the environmental elements are coming from the same direction. This differs from reality, where the environmental elements could come from different directions. The worst-case scenario is achieved when collinear conditions are assumed. During the simulations, the wind and the current direction are assumed to vary not over time. During some simulations, wave spreading is added, else also the waves are coming from one single direction. To be sure that every simulation is valid, each simulation is checked on potential errors. Simulations that contain an error are not used to generate results.

5-2-1 Preferable incoming angle of attack

Before the workability of the vessel can be calculated, the preferable incoming angle of environmental conditions should be determined. The incoming angle greatly affects the motions, and thereby the workability of the vessel. The studies of, [21], and [25] consider also monopile installation activities from a floating vessel. The studies conclude that the preferable angle of attack during an installation is between 195 and 210 degrees. But, in the study of [1] the governing limitation for the monopile installation is the roll motion of the vessel, which is minimal for an incoming angle of attack of 180 degrees. Additionally, the environmental forces on the vessel are minimal for head waves due to the shape of the vessel. On the other hand, the shielding effect is present for waves with an incoming angle between 180 and 360 degrees. The shielding effect is optimal for waves with an incoming angle between 210 and 310 degrees, shown in figure 4-23. Head waves and the shielding effect are considered in the incoming angle range of 180 to 210 degrees. Thus, it is interesting to search for the preferable incoming angle in this range. In figure 2-3, an overview of the incoming angle of attack is given.

The focus lies on the sea condition with a significant wave height of 3.0 m a wave peak period of 9.0 s to determine the preferable incoming angle for installing a monopile with the Stella Synergy. According to 3-2, the current and wind velocities are respectively 0.75 m/s and 13.5 m/s for this wave condition. In subsection 4-3-4 is explained why the focus lies on this particular sea condition. This sea state is used to test the model based on the limitation criteria with a varying environmental incoming angle between 170-210 degrees, with steps of 5 degrees. Simulation with an incoming angle of 170 and 175 are added to prove that shielding could be important. For each simulation, the maximum absolute values of the limitation criteria are determined. The results are visualised in figures 5-1 to 5-5.

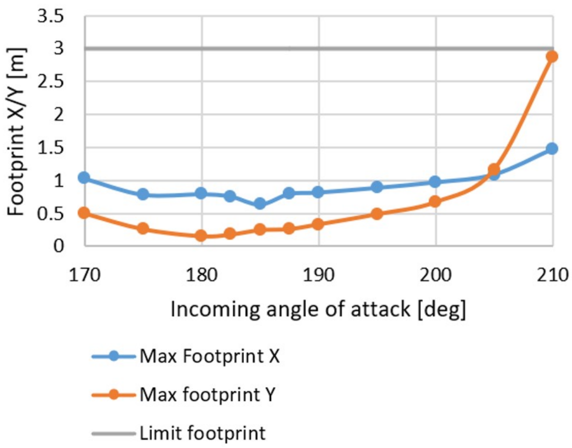

Figure 5-1: Maximum footprint over varying incoming angle. Sea condition: Hs=3.0 and Tp=9.0s

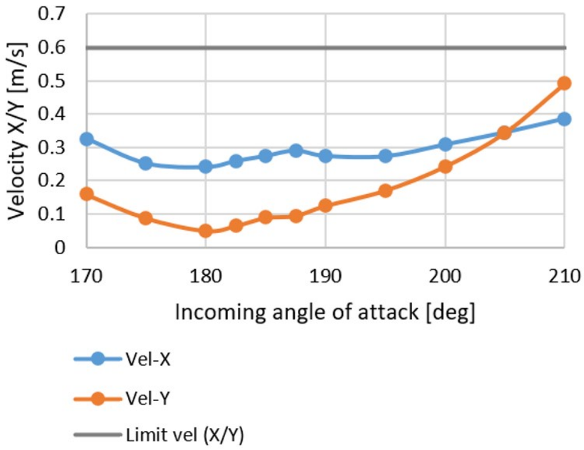

Figure 5-2: Maximum gripper velocity over varying incoming angle. Sea condition: Hs=3.0 and Tp=9.0s

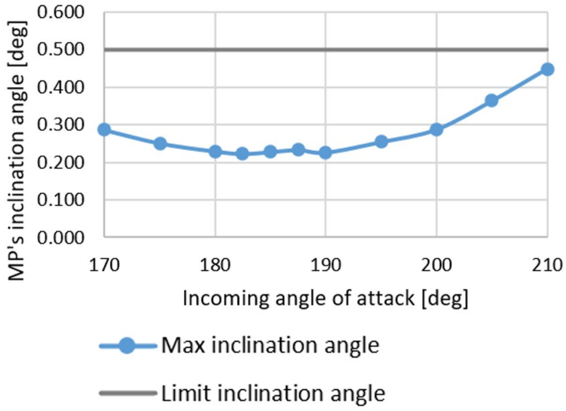

Figure 5-3: Maximum inclination angle over varying incoming angle. Sea condition: Hs=3.0 and Tp=9.0s

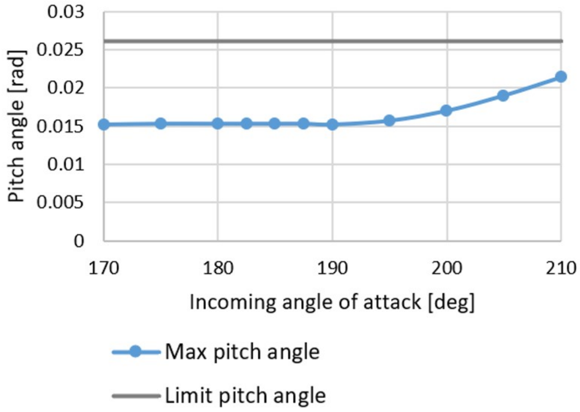

Figure 5-4: Maximum pitch angle over varying incoming angle. Sea condition: Hs=3.0 and Tp=9.0s

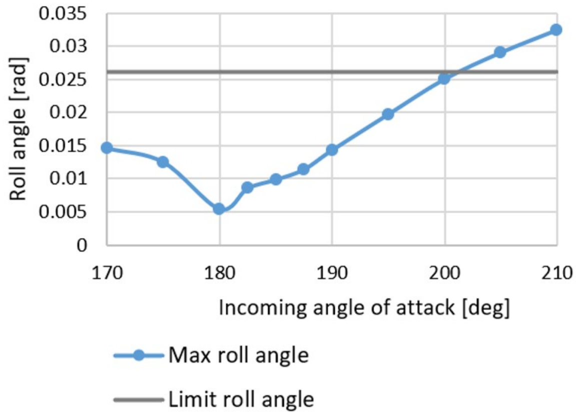

Figure 5-5: Maximum roll motion over varying incoming angle. Sea condition: Hs=3.0 and Tp=9.0s

The tested sea condition is not workable when the incoming angle is between 200 and 210 degrees due to a too large roll motion, as visible in the figure 5-5. The results for the other criteria also become worse for incoming angles larger than 200 degrees. Except for the roll-criterion, incoming angles in the range of 180 to 190 degrees are optimal, and no big differences in the maximum absolute values in this range are found. The maximum roll angle in a simulation is minimal for an incoming angle of 180 degrees and is increasing rapidly for increasing incoming angle. Since an incoming angle of 180 degrees is optimal for the roll-criterion and lies in the optimal range for the other criteria, it is concluded that the preferable incoming angle of environmental conditions is 180 degrees for this specific sea condition. Although it is known that the shielding effect is not optimal for an incoming angle of 180 degrees and the forces on the monopile are relatively large, the designed gripper can counter those forces for this sea condition. It is essential to note that this analysis is based on one single sea condition. During this analysis, the final governing limitation for installation monopiles with the Stella Synergy is unknown. At the end of subsection 5-2-3 is explained what the governing limitation is and why the preferable incoming angle is indeed 180 degrees.

It is interesting to zoom in into the incoming angle range of 170 to 190 degrees. Except for the pitch-criterion, all the results are worse for the incoming angle range of 170 to 180 degrees than for incoming angles of 180 to 190 degrees. This is the direct result of the shielding effect. The vessel partly protects the monopile for the incoming angle range of 180 to 190 degrees. On the other hand, the refracted waves on the vessel cause extra forces on the monopile for the incoming angle range of 170 to 180 degrees. The pitch motion of the vessel is practically constant for waves in the incoming angle range of 170 to 190 degrees. An enormous pitch moment is needed to affect the pitch motion of the vessel.

5-2-2 Workability

The last subsection concludes that the preferable angle of attack is 180 degrees for a sea condition with a significant wave height of 3.0 m and a wave peak period of 9.0 sec. Until the governing limitation for the workability is known, it is assumed that this is the preferable incoming angle for all sea conditions. Therefore, the workability is determined for an incoming angle of 180 degrees. This subsection shows how the workability is calculated and what the workability percentages for the separate limitations are. Finally, the governing limitation is determined, and it is verified if another incoming angle could result in a larger workability.

Total workability After doing some simulations for extreme conditions with and without considering wave spreading, it is concluded that the vessel is better capable of maintaining its position when wave spreading is considered. Adding wave spreading to the model results in significant decrements of the vessel's second-order wave force peaks. This probably causes the vessel to be better at keeping its position. Although adding wave spreading to the model gives a better representation of reality and gives better results, all the simulations are run without using wave spreading. This choice is made to reduce the simulation time. The simulation duration is approximately six times longer for a run that considers wave spreading.

For an incoming angle of 180 degrees and considering no wave spreading, simulations are run for all the sea conditions shown in Appendix D. For each simulation, the average significant wave height and wave peak period is chosen, meaning that the simulation for the upper-left sea condition of this scatter diagram has a Hs of 0.25 m and a Tp of 2.5 s. The wind and current velocities used during these simulations are read from table 3-2 and are shown at the bottom of figure 5-6. These simulations are tested based on the limitations described by 5-1. The gripper's velocity-x and velocity-y limitations are merged to one single limitation. When one or more limitations are exceeded, the sea condition is considered to be non-workable. The Dynamic Positioning (DP)-gains, which are optimised for Hs=3.0 m and Tp=9.0 s, are used for all these simulations.

After executing these simulations, the total workability is determined for an incoming angle of 180 degrees and considering no wave spreading. The simulations that are just non-workable are re-run while wave spreading is considered. The goal of these simulations with wave spreading is to determine if these sea conditions are workable when wave spreading is added. Except for roll and pitch criteria, the maximum values of tested criteria for the simulations considering wave spreading were all slightly lower than the simulation without wave spreading. Although all the results of the simulations with wave spreading were slightly better, only one sea condition, with Hs=4.75 m and Tp=8.5 s, is changed from non-workable to workable. This means that the other simulations with wave spreading are still not workable.

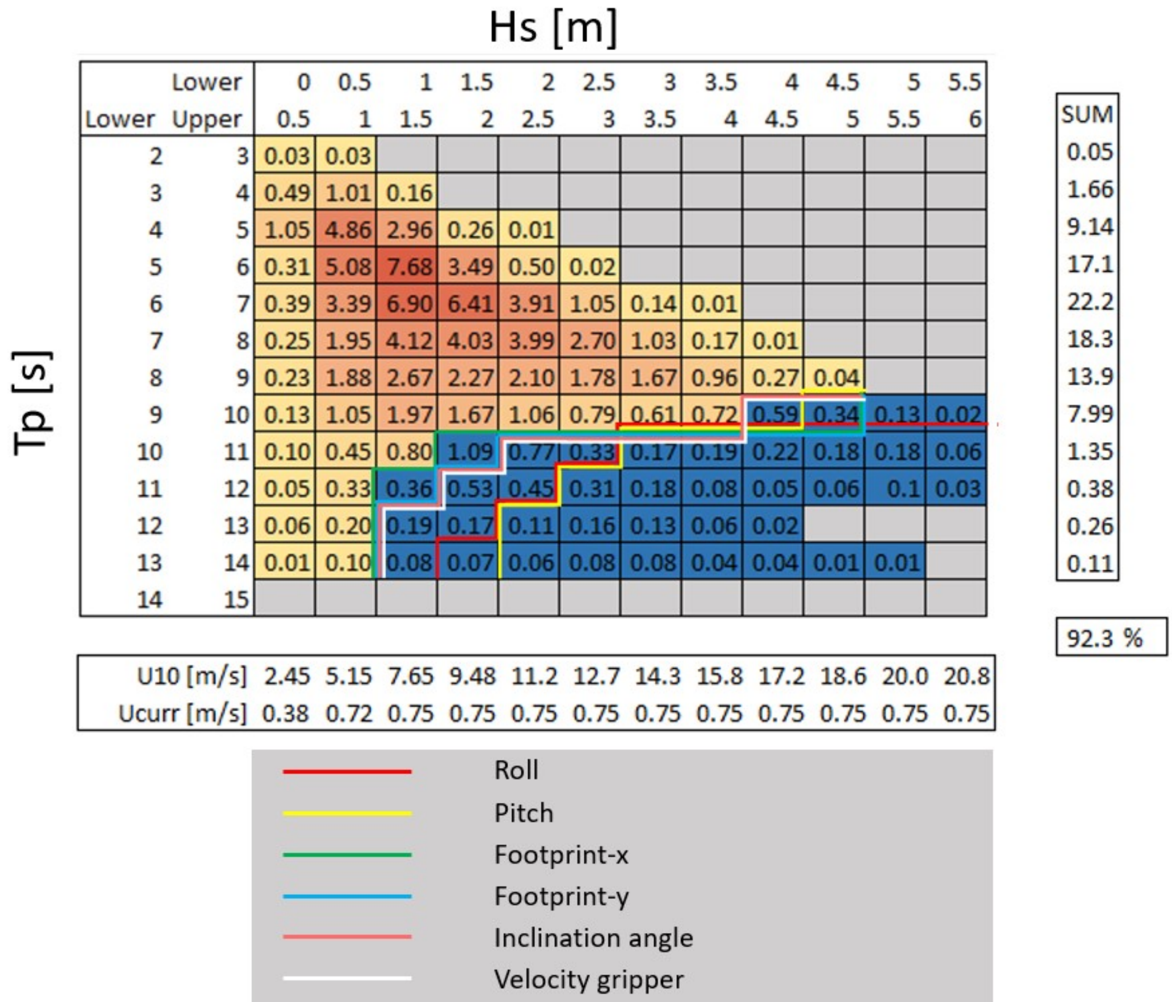

Tp Lower	Tp Upper	0–0.5	0.5–1	1–1.5	1.5–2	2–2.5	2.5–3	3–3.5	3.5–4	4–4.5	4.5–5	5–5.5	5.5–6	SUM
2	3	0.03	0.03											0.05
3	4	0.49	1.01	0.16										1.66
4	5	1.05	4.86	2.96	0.26	0.01								9.14
5	6	0.31	5.08	7.68	3.49	0.50	0.02							17.1
6	7	0.39	3.39	6.90	6.41	3.91	1.05	0.14	0.01					22.2
7	8	0.25	1.95	4.12	4.03	3.99	2.70	1.03	0.17	0.01				18.3
8	9	0.23	1.88	2.67	2.27	2.10	1.78	1.67	0.96	0.27	0.04			13.9
9	10	0.13	1.05	1.97	1.67	1.06	0.79	0.61	0.72	0.59	0.34	0.13	0.02	7.99
10	11	0.10	0.45	0.80	1.09	0.77	0.33	0.17	0.19	0.22	0.18	0.18	0.06	1.35
11	12	0.05	0.33	0.36	0.53	0.45	0.31	0.18	0.08	0.05	0.06	0.1	0.03	0.38
12	13	0.06	0.20	0.19	0.17	0.11	0.16	0.13	0.06	0.02				0.26
13	14	0.01	0.10	0.08	0.07	0.06	0.08	0.08	0.04	0.04	0.01	0.01		0.11
14	15													
														92.3 %
U10 [m/s]		2.45	5.15	7.65	9.48	11.2	12.7	14.3	15.8	17.2	18.6	20.0	20.8	
Ucurr [m/s]		0.38	0.72	0.75	0.75	0.75	0.75	0.75	0.75	0.75	0.75	0.75	0.75	

Figure 5-6: Total workability plot for an incoming angle of 180 deg and constant DP-gains

The scatter diagram that shows the total workability and the workability lines for the different limitations is shown in figure 5-6. The yellow-orange sea conditions are workable, and only these conditions contribute to the sum of the workability shown on the right side of the diagram. The blue conditions are non-workable because one or more of the limitations are exceeded. The coloured lines show the workability of the separate limitations. Every sea condition at the bottom-right of a limitation line means that the particular limitation is exceeded during this simulation.

The total workability for an incoming angle of 180 degrees and constant DP-gains is 92.3%, which is already relatively high. For comparison, the workability calculated in the study of [1] is 87%. This study also focuses on the workability of the Stella Synergy during monopile installation. However, in this study, a mooring system is used as a station-keeping system. Thus, the workability of the Stella Synergy operating on DP is higher than when it operates at its mooring system. The following subsection elaborates on the attempts to increase the total workability.

Interestingly, for waves with a peak period of 10.5 seconds, only sea conditions with a wave height lower than 1.5 m are workable. While, for example, the sea condition with Hs=3.75 m and Tp=9.5 s is workable. This dramatic decrement in workable sea conditions for Tp=10.5 s compared with Tp=9.5 s is mainly caused due to the footprint limitations.

Workability for separate limitation criteria The workability percentage for each limitation is calculated and shown in table 5-2. The footprint-x, footprint-y, inclination angle, and gripper's velocity workabilities are clearly lower than the roll and pitch workabilities. These four limitation criteria are all highly influenced by each other. When, for example, the vessel's footprint increases due to a relatively high vessel velocity, the gripper's velocity increases to counter the vessel's velocity. The gripper is only capable of countering a certain percentage of the vessel's motion, as shown in figures 4-30 and 4-31. Therefore, also the inclination angle increases when the vessel's velocity increases. The pitch and roll motion are far less influenced by the other criteria.

Table 5-2: Workability of separate limitations for an incoming angle of 180 deg and constant gains

Limitations:	Workability [%]
Footprint-x	93.3
Footprint-y	94.7
Roll	97.4
Pitch	97.0
Inclination angle	93.8
Velocity gripper	93.8
Total	92.3

The footprint-x criterion is governing for the workability with an incoming angle of 180 degrees and constant DP-gains. According to figure 5-1, the footprint-x is minimal for an incoming angle of 185 degrees. Although the difference with the footprint with an incoming angle of 180 degrees is small, and the roll motion increases significantly, the workability is also determined for an incoming angle of 185 degrees. The total workability and the workability for the separate limitation criteria are shown in figure H-1 and table H-1. The footprint-y, inclination angle and gripper's velocity workabilities slightly increase, but the roll workability decreases as expected. The reason to test the workability for an incoming angle is to increase the footprint-x workability. Unfortunately, it stays constant. The total workability decreases slightly, and therefore it is concluded that the preferable incoming angle of attack is indeed 180 degrees for this model.

5-2-3 Workability optimisation

The goal of this thesis is not only to determine the workability but also to increase the workability. A large number of factors influences the vessel's motion during a simulation. Changing one of these factors could result in a larger workability. As explained in the last section, the workable sea conditions decrease dramatically when the wave peak period increases from 9.5 s to 10.5 s. This decrement in workable sea conditions is unexpected, and so far, no reasoning about why this is happening is found. In the next three paragraphs of this subsection, some adaptations to the model are tested to possibly increase the workability of the model. First, fast-rotating thrusters are used, then the DP-gains are changed, and finally, it is verified if the vessel's pitch motion is minimal for an incoming angle of 180 deg.

Fast rotating thrusters In the model, thrusters are implemented that are able to change its angle maximum 12 deg/s. Some simulations that are just non-workable show large differences between the asked angle by the DP-system and the delivered angle by the thruster. This happens because the asked angle is changing faster than the maximum thruster's speed of rotation. Of course, this difference is only present for the azimuth thrusters. An example of this problem is shown in figure 5-7. The sea conditions in this simulation contain a significant wave height of 1.75 m and a peak wave period of 10.5 s. This is a sea condition that is just non-workable according to figure 5-6. Over a randomly chosen period of 500 seconds, the asked (blue) and delivered (black) angle of azimuth thruster is shown. The difference between the two lines is clearly visible. In this example, the asked and delivered angles sometimes jumps instantaneously from π rad to -π rad. In the simulation, this jump does not happen because an angle of π is equal to the angle of -π.

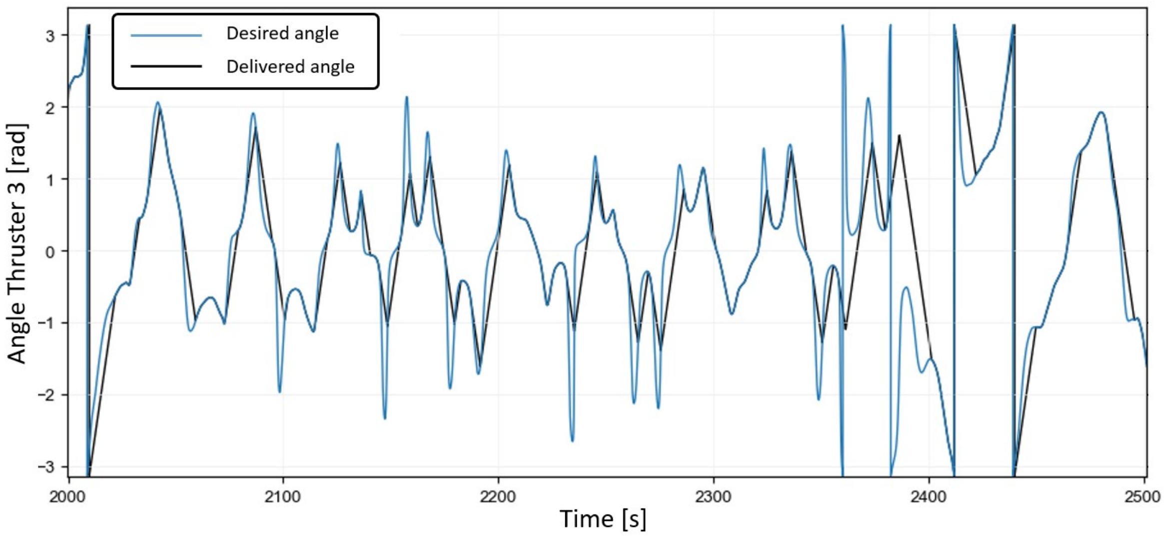

Figure 5-7: Desired and delivered angle for azimuth thruster 3, thruster rotational speed is 12 deg/s and standard DP-gains

It is interesting to see if the workability of the vessel increases when the thrusters are better capable of following the asked angle. Simulations for all the sea conditions which are non-workable are run, with thrusters with a maximum rotation speed of 24 deg/s to test if the workability increases. The tested azimuth thrusters rotate thus twice as fast. For the same sea condition as used for 5-7, figure 5-8 shows the difference between the asked and delivered angle for azimuth thruster 3 using the fast rotating thrusters.

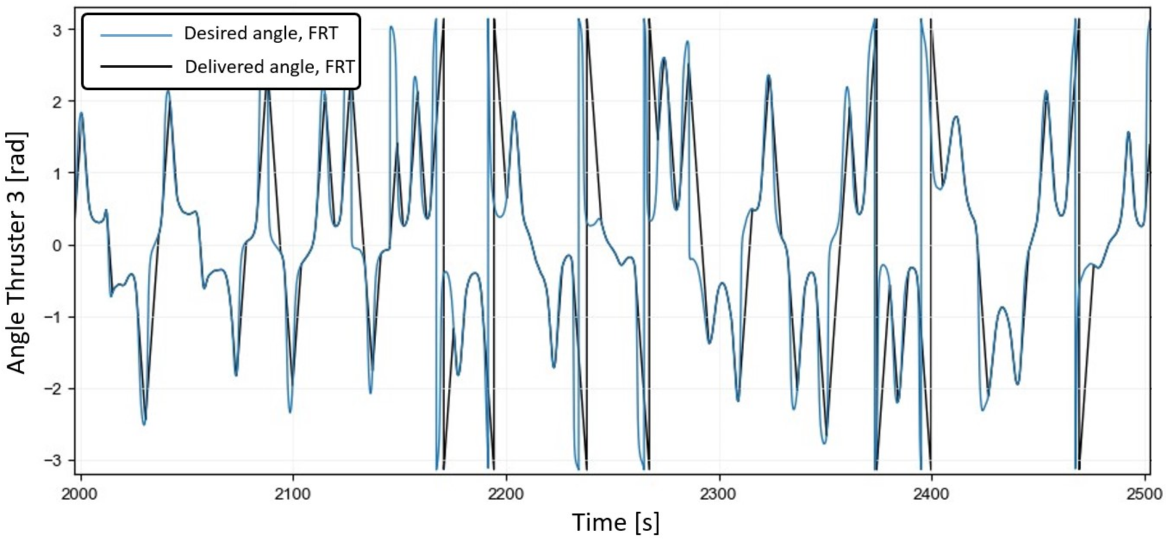

Figure 5-8: Desired and delivered angle for azimuth thruster 3, thruster rotational speed is 24 deg/s and standard DP-gains

Two differences are noticed when figures 5-7 and 5-8 are compared. Firstly, the azimuth thruster is changing its direction faster for fast-rotating thrusters. Secondly, the desired angle varies also faster over time. Therefore, it not possible to say if the thruster is better capable of following the desired angle. These differences are also found for azimuth thruster 4 and 5 and for all other tested sea conditions.

The workability plot for the vessel using fast rotating thrusters is shown in figure 5-9. Using fast-rotating thrusters increase the workability from 92.3% to 96.4%. Except for the pitch limitation workability, all the separate limitation workabilities percentages increase significantly. The governing limitation is shifted from footprint-x to the pitch, inclination angle, and gripper's velocity limitations. Especially, the pitch limitation is exceeded for most sea conditions which are just non-workable. But, the inclination angle and gripper's velocity limitations are exceeded for the sea conditions with Hs=4.25 m and Tp=9.5 s, which has a relatively high probability of occurrence. This sea condition is why the pitch limitations workability and the total workability are not the same. It could be that this sea condition would be workable if the Proportional Derivative (PD)-gains of the gripper are optimised for this specific sea condition. It is concluded that the workability of the Stella Synergy could be increased when fast-rotating thrusters will be installed, but it requires extra investment.

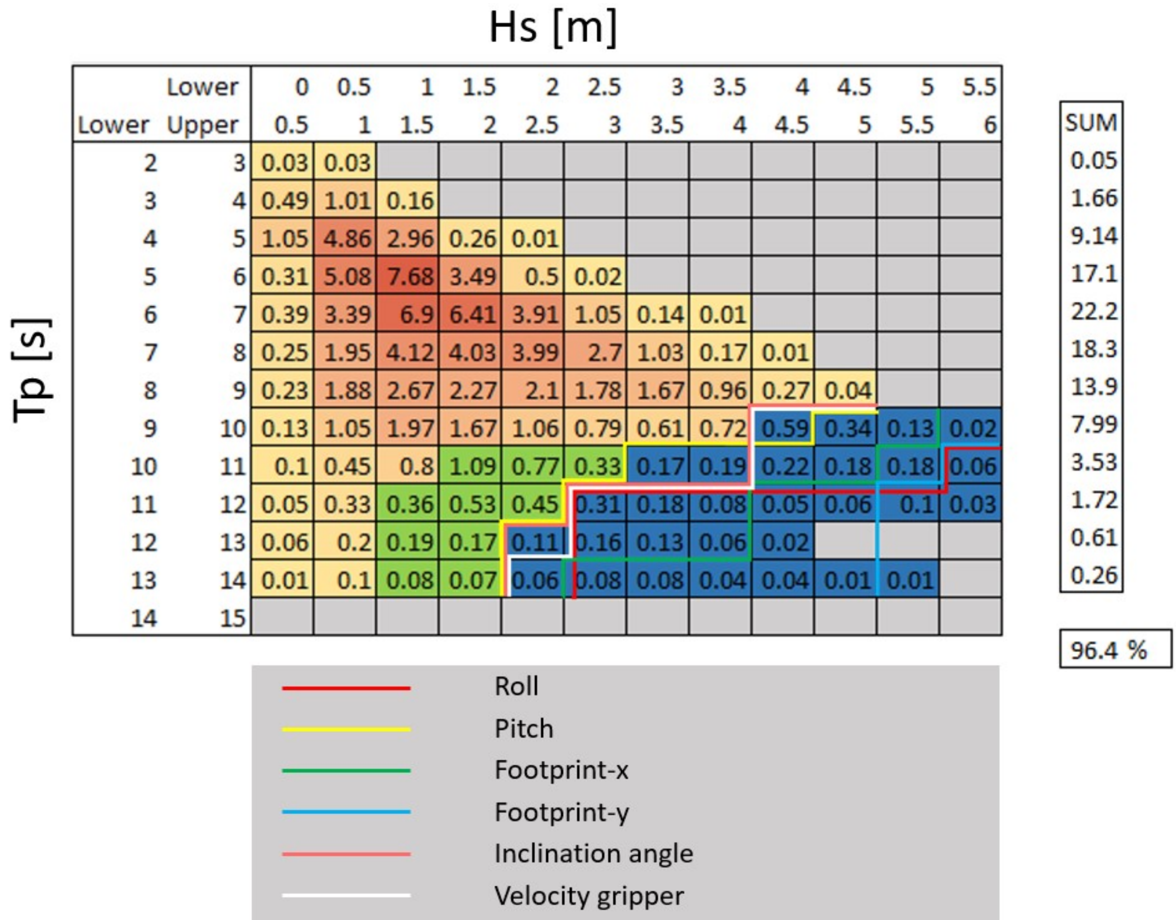

Tp Lower	Tp Upper	Hs 0–0.5	0.5–1	1–1.5	1.5–2	2–2.5	2.5–3	3–3.5	3.5–4	4–4.5	4.5–5	5–5.5	5.5–6	SUM
2	3	0.03	0.03											0.05
3	4	0.49	1.01	0.16										1.66
4	5	1.05	4.86	2.96	0.26	0.01								9.14
5	6	0.31	5.08	7.68	3.49	0.5	0.02							17.1
6	7	0.39	3.39	6.9	6.41	3.91	1.05	0.14	0.01					22.2
7	8	0.25	1.95	4.12	4.03	3.99	2.7	1.03	0.17	0.01				18.3
8	9	0.23	1.88	2.67	2.27	2.1	1.78	1.67	0.96	0.27	0.04			13.9
9	10	0.13	1.05	1.97	1.67	1.06	0.79	0.61	0.72	0.59	0.34	0.13	0.02	7.99
10	11	0.1	0.45	0.8	1.09	0.77	0.33	0.17	0.19	0.22	0.18	0.18	0.06	3.53
11	12	0.05	0.33	0.36	0.53	0.45	0.31	0.18	0.08	0.05	0.06	0.1	0.03	1.72
12	13	0.06	0.2	0.19	0.17	0.11	0.16	0.13	0.06	0.02				0.61
13	14	0.01	0.1	0.08	0.07	0.06	0.08	0.08	0.04	0.04	0.01	0.01		0.26
14	15													
														96.4 %

Figure 5-9: Total workability plot for an incoming angle of 180 degrees and using fast rotating thrusters. The sea conditions which are workable with fast rotating thrusters and were not workable and were not workable with original thrusters are shown in green.

Adapt gains In the last paragraph is concluded that the workability could be increased by investing in fast rotating thrusters. This paragraph describes a method to increase the workability without the need for investment.

Figure 5-7 shows the difference between the asked and delivered angle for azimuth thruster 3. It also shows that the asked angle by the DP-system varies rapidly over time, which is unexpected since the environmental conditions are assumed to be collinear. The thruster is even asked to circle multiple times during a simulation, which also holds for azimuth thruster 4 and 5. A comparison for the asked azimuth angle of thruster 3 for two different wave conditions is shown in figure 5-10. The only difference between the two sea conditions is the wave peak period; 9.5 s and 10.5 s. Clearly, the asked angle varies less for the sea conditions with Tp=9.5 s. The simulation with Tp=9.5 s is workable, and the vessel's motion is acceptable, while the simulation with Tp=10.5 s is not workable, and the vessel's motion is too large. It could be that the vessel's motion of the simulation with a Tp of 10.5 s is large, which results in rapidly changing desired angles of the azimuth thrusters. But it could also be the other way around that the DP-system determines rapidly changing desired angles for the azimuth thrusters, which results in large vessel motions.

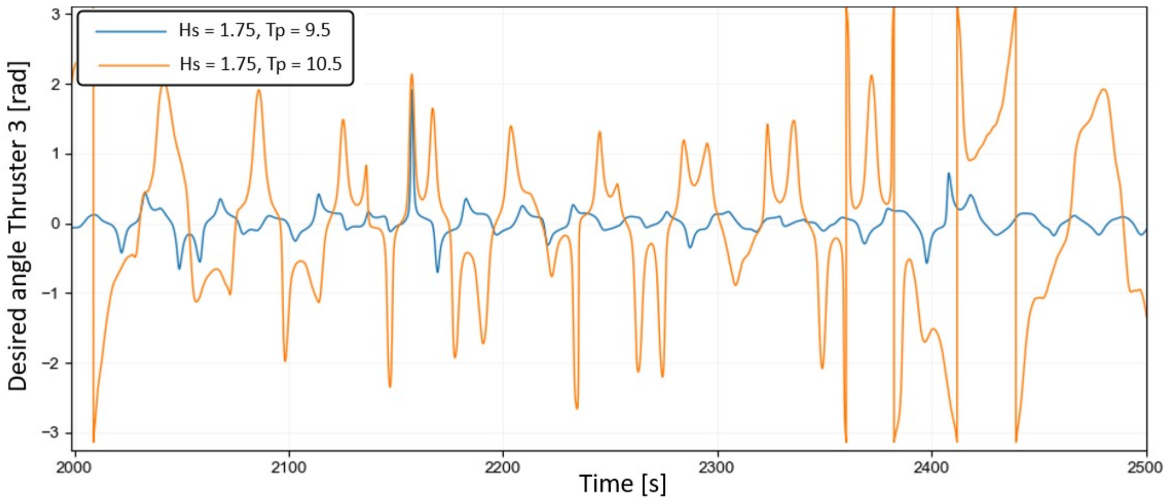

Figure 5-10: Desired angle for azimuth thruster 3,
two sea conditions with Hs=1.75 m and different Tp (9.5 and 10.5)

Multiple DP-gains are tested for the non-workable sea conditions shown in figure 5-6 to test this last phrased hypothesis. The ratio between the DP-gains is kept constant. As explained in section 4-3-4, the DP-gains are optimized for a sea condition with Hs=3.0 m and Tp=9.0 s. A larger wave peak period will cause the vessel to oscillate with a larger period. The higher the DP-gains are, the faster the system responds. Therefore, the DP-gains should be lower for sea conditions with a wave peak period larger than 9.0 s. After testing multiple DP-gains and varying wave peak periods, it is concluded that the vessel's motion decreases significantly for halved DP-gains when Tp>10 s. The vessel's motion increases when halved DP-gains are used for Tp<10 s. The halved DP-gains are shown in table E-2. A clear distinction is made for simulation with Tp<10 s and Tp>10 s.

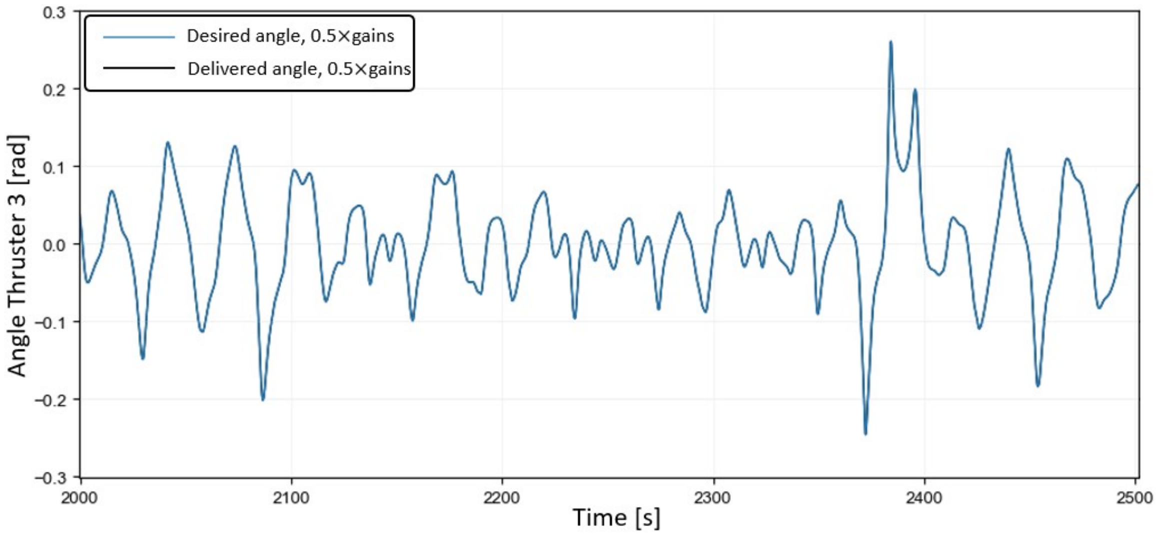

Figure 5-11: Desired and delivered angle for azimuth thruster 3,
thruster rotational speed is 12 deg/s and halved DP-gains

First, the behaviour of azimuth thruster 3 is tested with the same sea conditions as used in figure 5-7, this is visible in figure 5-11. Notice that the standard rotational speed of the azimuth thrusters is used. It is clearly visible that using halved DP-gains reduces the desired and delivered change of azimuth angle tremendously. The thruster does not circle anymore, and the delivered angle is following almost perfectly the desired angle. This behaviour is visible for all the azimuth thrusters and the entire simulation, not only these 500 seconds. The motions of the vessel decrease also tremendously. Therefore, it is concluded that the vessel's motion for sea conditions with Tp > 10 s could be reduced by using halved DP-gains. The lower gains give a better-controlled thruster behaviour.

The workability is determined using this distinction in DP-gains. The workability plot with half the DP-gains for all sea conditions with a larger Tp than 10 s is shown in figure 5-12. The sea conditions coloured in green were not workable with the original DP-gains, but are workable when halved DP-gains are used. The figure shows that the workability of the vessel increases when half of the DP-gains for Tp>10 s. The total workability increases from 92.3% to 96.4%.

Hs [m]

Tp [s]

	Lower	0	0.5	1	1.5	2	2.5	3	3.5	4	4.5	5	5.5	
Lower	Upper	0.5	1	1.5	2	2.5	3	3.5	4	4.5	5	5.5	6	SUM
2	3	0.03	0.03											0.05
3	4	0.49	1.01	0.16										1.66
4	5	1.05	4.86	2.96	0.26	0.01								9.14
5	6	0.31	5.08	7.68	3.49	0.5	0.02							17.1
6	7	0.39	3.39	6.9	6.41	3.91	1.05	0.14	0.01					22.2
7	8	0.25	1.95	4.12	4.03	3.99	2.7	1.03	0.17	0.01				18.3
8	9	0.23	1.88	2.67	2.27	2.1	1.78	1.67	0.96	0.27	0.04			13.9
9	10	0.13	1.05	1.97	1.67	1.06	0.79	0.61	0.72	0.59	0.34	0.13	0.02	7.99
10	11	0.1	0.45	0.8	1.09	0.77	0.33	0.17	0.19	0.22	0.18	0.18	0.06	3.53
11	12	0.05	0.33	0.36	0.53	0.45	0.31	0.18	0.08	0.05	0.06	0.1	0.03	1.72
12	13	0.06	0.2	0.19	0.17	0.11	0.16	0.13	0.06	0.02				0.61
13	14	0.01	0.1	0.08	0.07	0.06	0.08	0.08	0.04	0.04	0.01	0.01		0.26
14	15													

96.4 %

Roll
Pitch
Footprint-x
Footprint-y
Inclination angle
Velocity gripper

Figure 5-12: Total workability plot for an incoming angle of 180 degrees.
Half the DP-gains are used below the black line. The sea conditions which are workable now and were not workable for original DP-gains are shown in green.

Using the distinction in DP-gains, the workability percentage for each limitation is calculated and shown in table 5-3. Additionally, the workability percentages for each limitation using the standard DP-gains are shown to compare with. Except for the pitch-workability, all the separate workability percentages increase. The pitch motion is hardly affected by the DP-gains, and the workability percentage remains 97.0%. Due to the increase in workability of the other limitations, the pitch limitation is governing now. Although the DP-gains are not yet optimal for each simulation, optimising them could possibly increase the workability of multiple limitations, it will not increase the pitch workability. Since the pitch limitation is governing and is not affected by the DP-gains, and optimising the gains for each simulation is a very time-consuming process, no further research is done to optimise the gains further. It would be interesting to find a method the increase the pitch workability. The pitch motion is also not affected when wave spreading is added. Thus no extra simulations with wave spreading are run.

Table 5-3: Workability of separate limitations for 3 situations; Original DP-gains and thruster rotation speed, original DP-gains and fast rotating thrusters, half DP-gains for Tp>10s and original thruster rotation speed

Limitations:	Original workability [%]	Workability, fast rotating thrusters [%]	Workability, half DP-gains for Tp>10 s [%]
Footprint-x	93.3	99.3	98.6
Footprint-y	94.7	99.8	99.2
Roll	97.4	98.6	99.4
Pitch	97.0	97.0	97.0
Inclination angle	93.8	96.7	97.3
Velocity gripper	93.8	96.7	97.3
Total	92.3	96.4	96.4

Fast rotating thrusters vs adapting gains The total workability is the same when the DP-gains are changed as for when fast-rotating thrusters are used. Using fast rotational thrusters requires an extra investment while adapting the DP-gains does not. Using fast rotational thrusters and optimising the DP-gains will not increase the workability since it does not affect the governing pitch motion. Therefore, it is concluded that investing in fast-rotating thrusters to increase the workability is not recommended. But, it is recommended to optimise the DP-gains to maximise the workability. From now on, the distinction in DP-gains between sea conditions with a wave peak period larger than 10 s and smaller than 10 s is applied in the model. The model that uses this distinction is called the optimised model.

Figure 5-6 shows a large decrement in workable sea conditions for Tp=10.5 s compared with Tp=9.5 s. This decrement is reduced when fast-rotating thrusters or halved DP-gains are used. Therefore, it is concluded that this significant decrement is due to the combination of the thrusters slow rotational speed and the fast-changing desired azimuth angles due to too high DP-gains.

Table 5-4: Maximum footprint for workable sea conditions, 4 situations; Normal DP-gains and thruster rotation speed, normal DP-gains and fast rotating thrusters, halved DP-gains for Tp>10s and normal thruster rotation speed, and halved DP-gains for Tp>10s and fast rotating thrusters.

	Original model	Fast rotating thrusters	Halved DP-gains for Tp>10 s	Halved DP-gains for Tp> 10 s and fast rot. thrusters
Max offset-x [m]	2.95	1.77	1.95	1.77
Max offset-y [m]	2.05	1.31	1.14	1.00

Figure 5-11 shows that the azimuth thruster is able to deliver the desired angle. The same behaviour is found for the other thrusters and for all workable sea conditions. Still, it could be that when the optimised gains are combined with fast-rotating thrusters, it results in a lower vessel footprint. A motion-compensated gripper with a smaller envelope can be used when the vessel has a significantly lower footprint than +/- 3.0 m in x- and y-direction. This could lead to a cost reduction. Table 5-4 shows the maximum footprint of the vessel at the grippers location for four situations. When fast-rotating thrusters or halved DP-gains are used, it reduces the maximum footprint for the workable sea conditions significantly. When these methods are combined, it slightly reduces the maximum footprint for the workable sea conditions further. The currently used motion-compensated gripper has an envelope of +/- 3.0 m in x- and y-direction. A gripper with an envelope of +/- 2.0 m in the x-direction and +/- 1.2 in the y-direction will not decrease the workability of the vessel. Therefore, replacing the currently planned gripper with a gripper with a smaller envelope could be interesting. A gripper with a slightly smaller envelope can be used when fast-rotational thrusters are used. It requires some extra research to find out if it is worth investing in fast-rotating thrusters and replacing the gripper.

Decrease the pitch motion In the last paragraph is explained that the pitch motion is the governing limitation for the workability when the DP-gains are optimised. A decrease in the pitch motion of the vessel will increase the workability. According to [24], the pitch motion of a vessel could possibly decrease when the incoming angle of attack changes from 180 to 0 degrees. Unfortunately, figure 5-13 proves that the pitch motion of the vessel will slightly increase when an incoming angle of 0 deg is used. This picture shows the pitch moment Response Amplitude Operator (RAO)'s over a wave frequency range with an incoming angle of 0 and 180 deg. Over the entire frequency range, the pitch moment RAO for an incoming angle of 0 deg is slightly higher than for an incoming angle of 180 deg. Some simulations with sea conditions that are just non-workable according to 5-12 are run with the reversed vessel to verify if the pitch moment indeed slightly increase. These sea conditions contain a wave peak period between 9.5 and 13.5 s. Translating these wave period range into wave frequencies gives a wave frequency range between 0.46 and 0.66 rad/s. Although the differences in moment RAO's is minimal for this frequency range, a slight increase of the vessel's maximum pitch motion is visible for the simulations with an incoming angle of 0 deg.

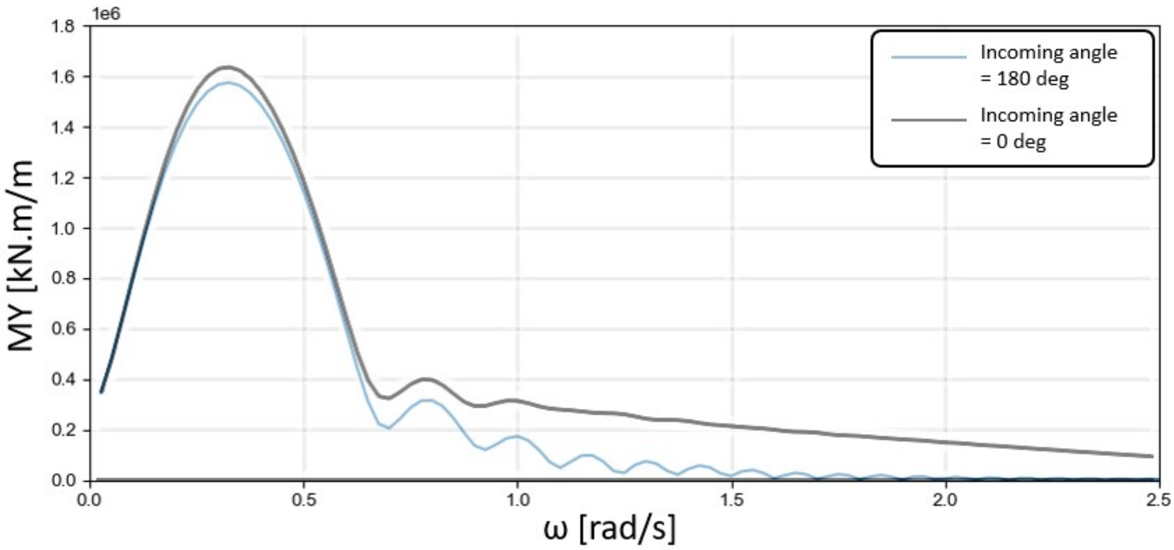

Figure 5-13: Pitch moment RAO's for head and stern waves over varying wave frequency

Additionally, it is verified if the pitch motion is minimal for an incoming angle of 180 degrees in the incoming angle range of 180 to 210 degrees. Figure 5-14 shows the pitch moment RAO contour plot over a wave frequency range of 0.46 to 0.66 rad/s. The incoming angle range of 170 to 180 deg is also shown in this figure to visualise that the pitch moment RAO increases for a smaller angle than 180 deg. Although the differences are minimal in the range of 170 to 190 deg, the figure shows that the pitch moment RAO for the vessel is indeed minimal for an incoming angle of 180 deg over the full critical frequency range. Notice that the pitch motion will decrease significantly when the vessel operates in beam waves. Unfortunately, sea conditions with beam waves cause large roll motion and are thus unfavourable.

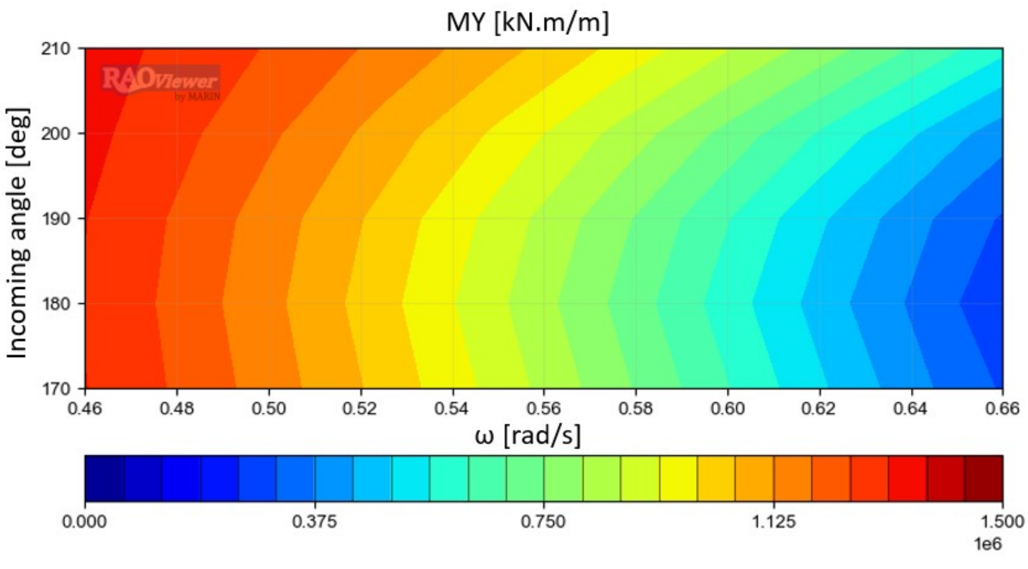

Figure 5-14: Pitch moment RAO contour plot over a wave frequency range of 0.46 to 0.66 rad/s

The pitch motion could be reduced by changing the hull shape. A hull with a fast increasing breath just above the waterline will give a pitch motion reduction. A pitch restoring moment will be caused by an increase in water displacement when the vessel pitches. Unfortunately, this hull shape is unfavourable when the vessel is sailing. Another method to reduce the pitch motion is to increase the length of the vessel. The Stella Synergy has an axe bow, which is already a pretty good shape to minimise the pitch motion according to [24].

5-2-4 Footprint reduction by adding mooring lines

Although the workability will not increase when the vessel's footprint decreases, it is still interesting to reduce the footprint. A smaller gripper could be used for installation monopiles when the vessel's footprint is reduced significantly for all workable situations.

Stiff mooring lines The study of [1] researched the workability of monopile installation with the Stella Synergy using only mooring lines as a station keeping system. This study uses the same maximum footprint limitation as used in this study, and it concludes that the workability for the footprint criterion is 94%. This relative high footprint workability percentage shows that using mooring lines is a suitable station keeping method. Using mooring lines in combination with the DP-system in heavy sea states might result in a reduced footprint. Therefore, simulations with sea conditions that are just workable according to figure 5-12 are run, using mooring lines and the DP-system as station-keeping systems. The simulated sea conditions are shown in 5-6. These sea conditions result in the largest footprint for all workable sea conditions. Thus it would be valuable to reduce the footprint for these sea conditions. The same mooring lines and mooring line configuration as described in subsection 4-3-2 are used, which are the same as used in the study of [1]. The same DP-gains, as used to determine the workability of figure 5-12, are used.

Table 5-5: Maximum footprint for workable sea conditions, 2 situations; Halved DP-gains for Tp>10 s and halved DP-gains for Tp>10 s and using mooring lines

	Halved DP-gains for Tp>10 s	Halved DP-gains for Tp>10 and using mooring lines
Max offset-x [m]	1.95	2.89
Max offset-y [m]	1.14	1.88

The maximum allowed tension in the used mooring lines is determined by the minimum breaking load divided by the safety factor. This limitation added for the simulations that contain mooring lines. The maximum allowed tension in the mooring lines is 1.18 MN. For the two simulations with the largest significant wave, this maximum mooring lines tension is exceeded. These simulations became non-workable due to the addition of the mooring lines. The maximum footprint in x- and y-direction of the other simulated sea conditions are determined and shown in table 5-5. The maximum footprint in x- and y-direction increase significantly when mooring lines are added to the model. The increase of footprint is even better visible in figure 5-15. This figure shows the vessel's position in x-direction near the gripper's location of two simulations, with and without using the mooring lines. The figure visualises the full 11000 s of the simulations for Hs=1.75 m and Tp=13.5 s. This sea condition and motion direction are chosen randomly. Similar results are found for the other simulations and in the y-direction.

Table 5-6: Just workable sea conditions according to figure 5-12

Sea condition	Hs [m]	Tp [s]
1	1.75	13.5
2	2.25	11.5
3	2.75	10.5
4	3.75	9.5
5	4.75	8.5

Table 5-5 and figure 5-15 show clearly that the vessel's footprint is increasing for the tested sea conditions when mooring lines are added to the model. Additionally, the yaw and roll motions increase significantly when mooring lines are added. The same simulations are re-run for halved DP-gains and without using the DP-system at all. The results of these simulations were even worse. Therefore, it is concluded that adding these mooring lines in this configuration to the model is not recommended.

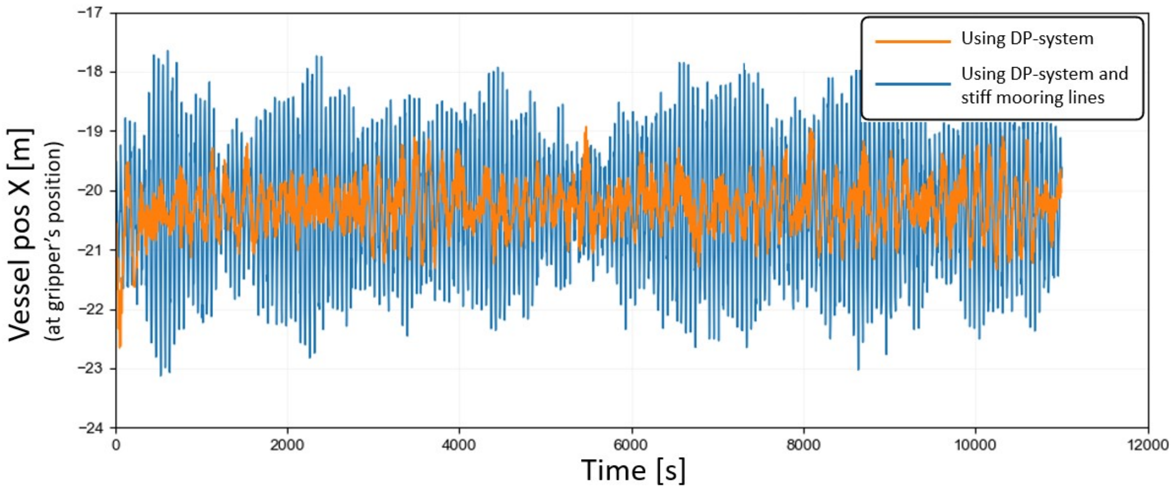

Figure 5-15: Vessel's x-position at grippers location, mooring vs no mooring lines. Original y-position = -20.24 m. Sea conditions: Hs=1.75 m and Tp=13.5 s.

Mooring lines with relative low axial stiffness It is counterintuitive that the vessel's footprint increases when mooring lines are added to the model. Some research is done to find out how this could happen. The vessel oscillates almost harmonically in the surge, sway, and yaw directions with the mooring lines active. The oscillation frequencies are not near the natural surge, sway, and yaw frequencies. Thus, the large vessel motions of the simulations could not be the results of oscillations in one of its natural frequencies. After analysing the simulations closely, it is concluded that thrusters are possibly not powerful enough to have a large impact on the vessel's motion when the mooring lines are active. The thrusters were operating frequently at maximum capacity to compensate for the large oscillations but were still not capable of taking over control.

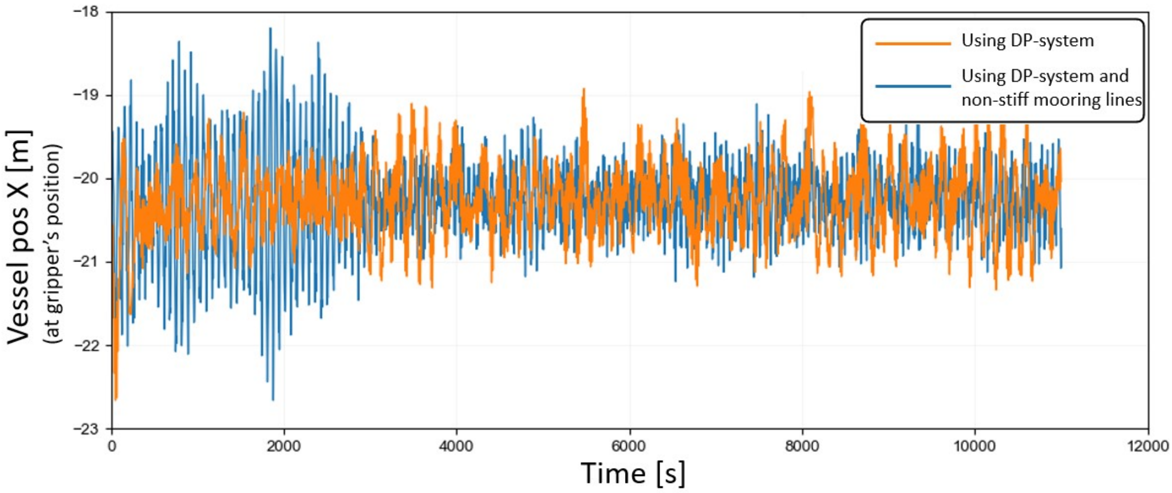

Figure 5-16: Vessel's x-position at grippers location, mooring lines with a relative low axial stiffness vs no mooring lines. Original x-position = -20.24 m. Sea conditions: Hs=1.75 m and Tp=13.5 s.

The same simulations are rerun with mooring lines with half of their original axial stiffness to test this hypothesis. The footprint of these simulations is reduced significantly compared to the footprint with the original axial stiffness, and the maximum tension in the mooring lines is not exceeded in any of the simulations. The footprint for sea conditions 3 and 5 of table 5-6 are even reduced significantly compared to the simulations without using the mooring system. For sea conditions 1 and 4, the footprint reduces for part of the simulation. In these simulations, it is good visible when the DP-system is capable of taking over control and use the mooring lines as assistance. The footprint for sea condition 2 increased significantly. Figure 5-16 shows the vessel's x-position at the gripper's location of 2 simulations in sea conditions 1. In one simulation, only the DP-system was working, and in the other, the mooring lines with a relatively low axial stiffness are used additionally. After approximately 3000 seconds, the DP-system is capable of reducing the vessel's motion significantly. From this point, the offset peaks are even slightly lower when the mooring lines are used. Thus, the footprint of the vessel could be reduced by adding mooring lines when the stiffness of the mooring lines is chosen wisely. Additional research should be done to find the optimal axial stiffness and determine if the reduction in footprint can be reached for each sea condition.

5-2-5 Monopile's influence on vessel's motion

The study of [1] concludes that the monopile has no significant influence on the vessel's motion, while the study of [16] contradicts this. This difference could occur due to a difference in the installation phase that is considered. It is interesting to research if the monopile influences the motion of the Stella Synergy. In this subsection is explained how this research is executed and what the result of the research is.

Simulations Five simulations with sea conditions that are just workable are run to test if the monopile influences the vessel's motion. The tested sea conditions are the same as in the previous section and are shown in table 5-6. The forces from the monopile that act at the vessel through the gripper are manually set to zero for these simulations. In figure 4-28, this force in y-direction is shown by $FY_{gripper}$. The vessel's surge, sway, roll, pitch, and yaw motions are tested in these simulations.

Results The maximum footprint in x- and y-direction and the maximum rotational angles from the original position of the vessel are shown in table 5-7. In this table, the results for the simulations with and without monopile's influence on the vessel are shown. Except for the maximum pitch motion angle, the maximum offsets for the other motions reduces significantly. Even the maximum roll angle of the vessel decreases by 12.1% when the monopile does not influence the vessel's motion. The monopile hardly influences the pitch motion of the vessel, and the maximum pitch angle is even precisely the same. The overall conclusion of the simulations is that the monopile significantly influences the vessel's motion. This influence could be reduced when the force on the vessel is fed-forwarded into the Kalman filter, so the vessel's DP-system can respond faster.

Table 5-7: Maximum vessel motions for all workable conditions, 2 situations: Optimised simulations and simulations with no influence of monopile on the vessel.

	Optimised model	No influence of monopile on vessel	Maximum motion reduction [%]
Max offset-x [m]	1.95	1.49	23.6
Max offset-y [m]	1.14	0.77	32.5
Max roll angle [deg]	0.596	0.524	12.1
Max pitch angle [deg]	1.47	1.47	0.0
Max yaw angle [deg]	2.32	1.28	44.8

Table 5-8 is made to verify if it is logical that the monopile has such a significant effect on the vessel's motion. This table shows the percentage of the average environmental force in x-direction on the vessel and the monopile for the five critical sea conditions. The average first-order wave forces, the average second-order wave forces, the average current forces and the average wind forces on the vessel and monopile are considered. Although the first-order wave force peaks on the vessel and monopile are relatively large, the average first-order wave forces are approximately zero. On average, the percentage of environmental forces in x-direction on the monopile is 38.1%. This relatively large percentage of environmental force acts partly at the vessel through the gripper and will cause the vessel's motion. Thus it is logical that the monopile influences the vessel's motion significantly. Notice that the soil counters the environmental force on the monopile partly because the monopile is modelled as an inverted pendulum.

Table 5-8: Percentage of average environmental forces in x-direction on vessel and monopile during 5 simulations.

Sea condition		Percentage	
Hs [m]	Tp [s]	Vessel	Monopile
1.75	13.5	47.5	52.5
2.25	11.5	56.3	43.7
2.75	10.5	62.3	37.7
3.75	9.5	69.7	30.3
4.75	8.5	73.7	26.3
Average		61.9	38.1

5-2-6 Workability for worst-case single failure

The vessel's DP-system is of class 2, which means that station-keeping capability for a particular sea condition will be achieved for a worst-case single component failure in a unidirectional environment. This subsection explains how this worst-case single failure is modelled and how it influences the workability of the vessel.

Worst-case single failure According to [24], the worst-case failure of the Stella Synergy is the loss of main switchboard 1. This could be caused, for example, by electric short-circuiting or the failure of the generators that provide the power for main switchboard 1. Tunnel thruster 1 and main azimuth thruster 4 are directly connected to main switchboard 1. Figure 4-4 shows the thrusters configuration. When switchboard 1 fails, tunnel thruster 1 and main azimuth thruster will also fail. This results in the loss of 41% of the maximum delivered thrust, mainly the loss of main azimuth thruster 4 has a large impact on the loss of the maximum delivered thrust. As explained in subsection 4-3-1, it is not possible to stop and start the engine of the thrusters unlimited. Therefore, the tunnel thrusters are modelled to deliver thrust in only one direction. The loss of tunnel thruster 1 results in the situation that the leftover tunnel thruster can only provide thrust in one single direction, without the other tunnel thruster active to deliver thrust in the other direction. Fortunately, Jumbo Maritime has built an azimuth thruster in the bow that can produce thrust in all directions. In aNySIM, this worst-case single failure is modelled by neglecting thruster 1 and 4 in the DP-system. During the simulations, the DP-system only considers thrusters 2, 3, and 5.

Workability determination and optimisation The sea conditions of the North Sea shown in figure D-1 are tested with a switchboard 1 failure to determine the workability and the workability limitation lines. The workability plot, shown in figure 5-17, requires some explanation. Just as for the workability plot shown in figure 5-12, halved DP-gains are used for the sea conditions with a wave peak period larger than 10 seconds. Without further adaptations of the gains, the brown and red coloured sea conditions became unworkable while they were workable without a single failure.

The significant reduction in workable sea conditions for a peak wave period of 9.5 s was unexpected. For most of these simulations, all the limitations are exceeded, except for the pitch limitation. After analysing the results of the simulations with these sea conditions, it is concluded that the DP-gains are probably too high. The fluctuation in asked power and thrust by the DP-system is relatively high, while 41% of the power is lost. The thrusters are not capable of dealing with this fast-changing thrust demand. Therefore, it would be interesting to lower the DP-gains for these sea conditions. Also, the same phenomenon as shown in figure 5-10 is found for these simulations. The asked angle for the resulting two azimuth thrusters fluctuates enormously for all simulations with a wave peak period of 9.5 s, while this was not visible for these simulations without the single failure. Earlier, these sea conditions were tested with halved DP-gains without applying a single failure. These simulations showed that the vessel's motion increased when halved DP-gains are used. This shows that the optimal DP-gains depend not only on the sea conditions the vessel is operating in but also on the available thrusters of the vessel. Again, this shows that it would be interesting to use lower DP-gains. Therefore, the unworkable sea conditions for a wave peak period of 9.5 s are re-run with halved DP-gains, and the results changed dramatically. Five unworkable sea conditions became workable due to the adaptation in DP-gains; these are shown in brown. The vessel's surge, sway, yaw, and roll motions decreased enormously using the halved DP-gains.

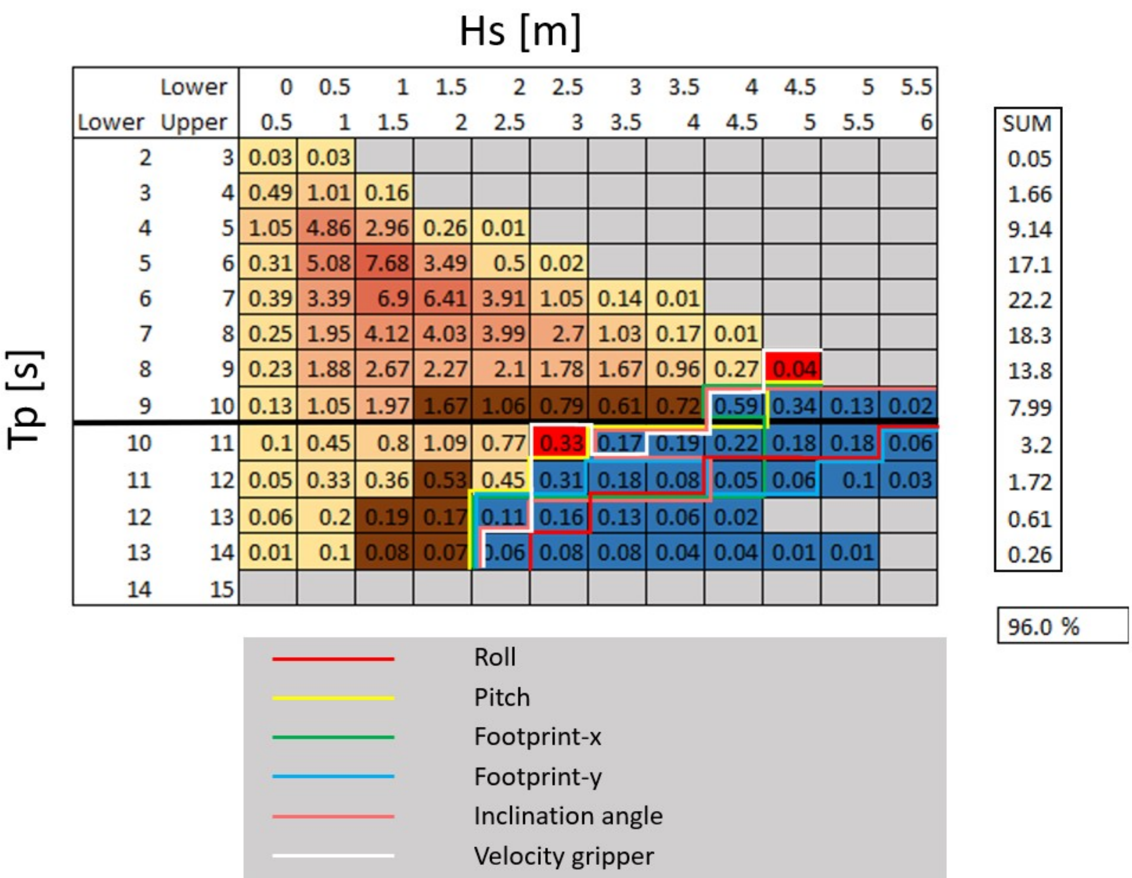

Tp Lower	Tp Upper	Hs 0–0.5	0.5–1	1–1.5	1.5–2	2–2.5	2.5–3	3–3.5	3.5–4	4–4.5	4.5–5	5–5.5	5.5–6	SUM
2	3	0.03	0.03											0.05
3	4	0.49	1.01	0.16										1.66
4	5	1.05	4.86	2.96	0.26	0.01								9.14
5	6	0.31	5.08	7.68	3.49	0.5	0.02							17.1
6	7	0.39	3.39	6.9	6.41	3.91	1.05	0.14	0.01					22.2
7	8	0.25	1.95	4.12	4.03	3.99	2.7	1.03	0.17	0.01				18.3
8	9	0.23	1.88	2.67	2.27	2.1	1.78	1.67	0.96	0.27	0.04			13.8
9	10	0.13	1.05	1.97	1.67	1.06	0.79	0.61	0.72	0.59	0.34	0.13	0.02	7.99
10	11	0.1	0.45	0.8	1.09	0.77	0.33	0.17	0.19	0.22	0.18	0.18	0.06	3.2
11	12	0.05	0.33	0.36	0.53	0.45	0.31	0.18	0.08	0.05	0.06	0.1	0.03	1.72
12	13	0.06	0.2	0.19	0.17	0.11	0.16	0.13	0.06	0.02				0.61
13	14	0.01	0.1	0.08	0.07	0.06	0.08	0.08	0.04	0.04	0.01	0.01		0.26
14	15													

96.0 %

Figure 5-17: Total workability plot for an incoming angle of 180 degrees and the failure of main switchboard 1. Half the DP-gains are used below the black line. The sea conditions that became unworkable due to the single failure are shown in green. The sea conditions that are only workable after optimising the gains are shown in brown.

For the other five brown coloured sea conditions, with relative high wave peak periods, the footprint limitations were exceeded. The surge and sway motions increase significantly when the worst-case single failure occurs. But, compared to similar simulations without a single failure, especially the yaw motion increases enormously. The yaw motion for two simulations, with and without the single failure, are shown in figure 5-18. Probably, this large yaw motion is mainly the result of the loss of tunnel thruster 1, which is a critical element to control the yaw motion of the vessel. The sea conditions might be workable for this single failure when the focus of the DP-gains shifts to the yaw-motion control.

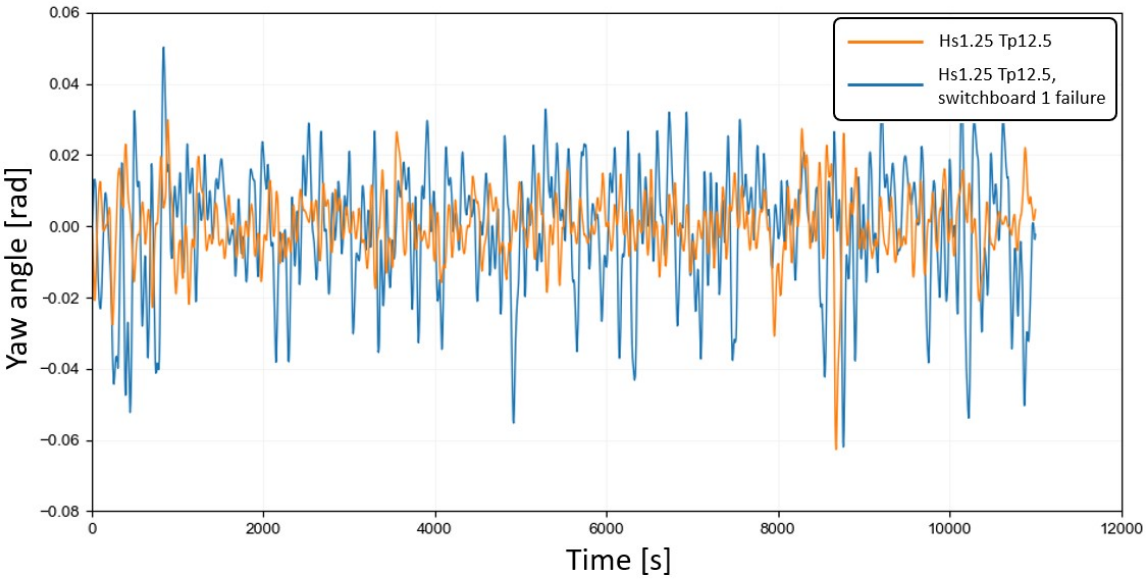

Figure 5-18: Yaw angle of the Stella Synergy of 2 simulations with Hs=1.25 m and Tp=12.5 s and halved DP-gains: One without a failure, one with the failure of main switchboard 1, which results in the loss of tunnel thruster 1 and main azimuth thruster 4.

This hypothesis is tested by simulating these five sea conditions with various DP-gains. The results are very promising when the surge and sway gains divided by 4 and the original yaw gains are used. The yaw-motion is reduced back to approximately the original simulation without the single failure, and the footprint limitations are not exceeded anymore. Using these DP-gains, the five sea conditions coloured brown in figure 5-17 with a relative high wave peak period are workable.

This little research about a single failure proves that optimising the DP-gains for each sea condition could improve the workability of the vessel. With two extra adaptations to the DP-gains, the workability for the failure of switchboard 1 increases to 96.0%, which differs only 0.4% from the original workability. The two sea conditions that became unworkable due to the failure might even be workable when the DP-gains are optimised for these conditions. Table 5-9 shows the workabilities for the separate limitations criteria for the failure of switchboard 1 and the situation with no failure. According to this table, the inclination angle limitation is governing. But, figure 5-17 shows that multiple limitations influence the final workability. The final workability with the failure of main switchboard 1 is determined to be 96.0%, which is quite high. If the failure of main switchboard 1 is indeed the worst case failure, the vessel's workability barely decreases for any single failure.

Table 5-9: Workability of separate limitations for 2 situations with an incoming angle of 180 deg; With no failure, and with main switchboard 1 failure and doing 2 adaptations in the DP-gains for some sea conditions.

Limitations:	Optimised workability [%]	Workability with worst-case single failure [%]
Footprint-x	98.3	97.6
Footprint-y	99.2	98.8
Roll	99.4	99.1
Pitch	97.0	97.0
Inclination angle	97.3	96.3
Velocity gripper	97.3	97.0
Total	96.4	96.0

Chapter 6

Conclusions and recommendations

This chapter discusses the conclusions of this thesis. A brief explanation about the model is given, and the results of the model are discussed. Afterwards, some recommendations to improve the model are proposed, and some recommendations for future research are given.

6-1 Conclusions

In this thesis project, a workability study and a workability optimisation study are done for XXL-monopile installation with the Stella Synergy. A complex model is built in the time domain simulation program aNySIM to calculate and optimise the workability. The vessel uses its Dynamic Positioning (DP)-system for station keeping and a motion-compensated pile gripper to compensate the vessel's horizontal motion and keep the monopile vertical. The early pile driving phase is considered since this phase contains the highest risk. The model accurately describes the vessel's, gripper's, and monopile's motion, depending on the collinear environmental conditions. The influence of the environmental conditions on the vessel and monopile is described by added mass and added damping matrices, force Response Amplitude Operator (RAO)'s, and Quadratic transfer functions (QTF)'s, generated by diffraction calculations in Ansys AQWA. The gripper's motions and its influence on the vessel and monopile are modelled by two Proportional Derivative (PD)-controllers in Python. The model is used to determine the preferable angle of environmental conditions, the vessel's workability, and it is used to optimise the workability. Furthermore, it is researched if adding mooring lines to the model could reduce the vessel's footprint and the influence of the monopile on the vessel's motion. Additionally, the effect on the workability of the worst-case single failure is tested. The results of these researches are generated by doing multiple simulations with varying sea conditions tested by six limitations of the model. In this section, the conclusions of these researches are summed.

Preferable incoming angle of attack Research is done to find the preferable incoming angle of attack for monopile installation with the Stella Synergy. In this research, the incoming angle range of 180 to 210 degrees is tested for a specific critical sea condition. In this range, the shielding effect is present, and the vessel experiences relative low environmental forces. The simulations with varying incoming angles are tested by the six limitations of the model. Except for the roll-criterion, incoming angles in the range of 180 to 190 degrees are optimal for all criteria. These tested criteria are more or less constant and minimal in this range. The roll motion is minimal for an incoming angle of 180 degrees and is increasing rapidly for increasing incoming angle. Therefore, it is concluded that the optimal incoming angle of attack for this critical sea condition is 180 degrees. After calculating and optimizing the workability of the vessel, it is concluded that the vessel's pitch motion is the governing limitation of the model. The pitch moment is minimal for an incoming angle of 180 degrees in the considered incoming angle range, considering the critical frequency range. Therefore, it is concluded that the preferable incoming angle of attack of environmental conditions for the Stella Synergy during a monopile installation operation is 180 degrees. This means that the vessel operates optimally when the environmental conditions attack the vessel exactly from the front. The shielding effect is not optimal for this angle of attack, and relative large wave forces act at the monopile. But the motion-compensated gripper is capable of keeping the monopile vertical for most sea conditions. Notice that the pitch motion will reduce when the vessel operates in beam waves, but these waves are unfavourable due to the large roll motions of the vessel.

Workability determination and optimisation Simulations with varying sea conditions of the North Sea are run using the preferable angle of 180 deg. The DP-gains are optimised for one specific sea condition, and these gains are used for all sea conditions to calculate the workability. Before some methods are used to increase the workability, the workability of Stella Synergy is 92.3%. The non-workable sea conditions are re-run twice, once with an adaptation in the DP-gains depending on the wave peak period and once with the use of fast-rotating azimuth thrusters. Fast rotating thrusters are thrusters that can fast change their angle to their vertical axis. Both adaptations result in an increase of workability to 96.4%. Notice that a workability of 96.4% is relatively high compared to the workability of the Stella-Synergy using mooring lines, which is 87% [1]. The pitch motion of the vessel is the governing limitation. An investment is required to use fast-rotational azimuth thrusters while changing the DP-gains is for free. Therefore, it is recommended to optimise the DP-gains for each sea condition and to invest not in fast rotating thrusters.

Using the adapted DP-gains, which are not yet optimised for every single sea condition, results in a maximum footprint of the vessel at the gripper's position of 1.95 m by 1.14 m in x- and y-direction for all workable sea conditions. This means that the currently used motion-compensated pile gripper, which has an envelope of 3 m by 3 m in x- and y-direction, is over-dimensioned for installing XXL-monopiles with the Stella Synergy. Choosing a slightly smaller motion-compensated pile gripper could result in a cost reduction, while it won't affect the workability.

Reducing footprint by adding mooring lines Some simulations with mooring lines and an active DP-system are run to research if the footprint of the vessel decreases when mooring lines are added to the model. In these simulations, mooring lines with relatively high and relatively low axial stiffness are tested. Using mooring lines with a relatively high axial stiffness results in a significant footprint increment and are thus not recommended. Some simulations with added mooring lines with relatively low axial stiffness showed a reduced vessel's footprint. Probably, it is crucial that the DP-system stays in control and uses the mooring lines purely as assistance. Additional research is needed to test this hypothesis and find the optimal axial stiffness of the mooring lines for each sea condition. Before this additional research is done, it is not recommended to use mooring lines next to a good working DP-system. The benefits of adding mooring lines are unclear, and additionally, it is a very time-consuming process to put the mooring lines in place.

Monopile's influence on vessel's motion The environmental forces on the monopile are passed through the gripper to the vessel. Some simulations are run with a zero force of the monopile on the vessel. These simulations are compared with simulations that consider this force on the vessel to research the influence of this force on the vessel's motion. It is concluded that the monopile significantly increase the vessel's surge, sway, roll, and yaw motion. The monopile hardly influences the vessel's heave and pitch motions.

Workability for worst-case single failure The vessel DP-system is of class 2, which means that a single failure will not cause the whole system to fail. According to [24], the worst-case single failure of the Stella Synergy is the loss of main switchboard 1, which controls tunnel thruster 1 and main azimuth thruster 4. A failure in this switchboard means the loss of tunnel thruster 1 and main azimuth thruster 4, causing a loss of 41% of maximum delivered thrust. The workability of the vessel is calculated for this single failure. After optimising the DP-gains for two regions of sea conditions, the calculated workability is 96.0%. This is only 0.4% lower than the workability without a single failure. Assuming that the loss of main switchboard 1 is indeed the worst-case failure, the vessel will still have a large workability percentage for any single failure in the system.

Monopile installation with floating vessel In this thesis, it is researched if using a floating vessel operating on its DP-system for monopile installation is a good alternative for using a jack-up vessel, which is the currently used method. The floating heavy lift vessel Stella Synergy using a motion-compensated pile gripper is tested in the sea conditions of the North Sea. The vessel has a workability of 96.4%, which is very satisfactory. Notice that it is essential for the vessel to adapt its DP-system to the sea condition is it operating in. The relatively low downtime of the vessel in combination with the fast installation method the vessel uses makes it a very suitable vessel for XXL-monopile installation. The vessel is thus an impressive alternative for the currently used jack-up vessels.

6-2 Recommendations

In this section, some recommendations are made for future studies. First, some improvements for the model and afterwards some extra researches are proposed.

Model In the model, the wave shielding effect is considered. The shielding effect influences the wave forces on the monopile significantly. Although the wind and current forces are of minor importance, the model would be more accurate when the wind and current shielding effect is considered. Furthermore, it is assumed that the vessel's deck is empty, and possible wind forces on structures placed on the deck are thus not considered. This differs significantly from reality, where enormous structures such as a monopile are sometimes placed on the deck. It is advisable to consider the worst-case scenario of the wind forces on the structures placed on the deck of the Stella Synergy.

In this thesis, it is found that lower DP-gains should be used for waves with a large peak wave period. Therefore, a distinction in DP-gains is made between waves with a larger and lower wave peak period than 10 s. In reality, the staff of Kongsberg DP is present at the vessel to optimise the DP-system, depending on the sea conditions and the kind of operation of the vessel. It is advisable to optimise the DP-gains of the model for each sea condition. In the model, the DP-system uses a single accurate reference system for the determination of the vessel's location. In reality, the vessel's location is based on multiple noisy reference systems. It would be better to implement these inaccuracies into to model. Furthermore, the DP-system could be optimised when the forces that the monopile act at the vessel would be fed forwarded into the Kalman filter. The DP-system would be able to respond faster at these forces from the monopile, and the vessel might be better in station keeping. It is also advisable to add forbidden zones to the DP-system. Forbidden zones are typically added for thruster angles that result in a large thruster-thruster interaction. It would be better to implement the forbidden zones in the model.

A static diffraction calculation for the monopile is executed, which means that the monopile cannot move during the calculation. Therefore, the added mass and damping matrices are not calculated, and no added mass and damping for the monopile is assumed. Although this is an acceptable assumption since the monopile's velocity and acceleration are relatively low, it would be more accurate to consider added damping and mass. Furthermore, no monopile-soil interaction is assumed because significant inaccuracies occur in the calculation for the soil stability force. It is advisable to determine the minimal soil stability force and add this force to the model. Additionally, the monopile is assumed to be rigid while it could deform in reality. It would be interesting to know if the gripper deforms the monopile during the installation and which fatigue damage the monopile experiences due to the gripper forces.

The Stella Synergy will probably use the motion-compensated pile gripper fabricated by Huisman Equipment B.V. This gripper contains two parts. Both of them translate in surge direction, while only one part translates in sway direction. In the model, it is assumed that the gripper consists of one single part moving in surge and sway direction. In the model, a numerical problem was found and solved. The solution to the problem is acceptable, but it might results in inaccurate gripper velocities for absolute gripper velocities lower than 0.009 m/s in x- and y-direction. It is advisable to use a gripper that represents a real gripper more accurately. It would be better to build a gripper with multiple parts which represents the gripper's velocities accurately for all velocities. Additionally, some additional research is needed to model the hydraulic pressure built-up more accurately.

Extra research In this research, the focus lies on the early pile driving phase because this phase is governing in terms of risk. The forces on the vessel and monopile differ for the different installation phases. For example, it would be interesting to know if the vibrations of the vibro-drill or the soil-stability force for an increased monopile penetration depth will influence the vessel's motions or gripper's behaviour. Therefore, it would be interesting to research the workability of the vessel during other installation phases.

As additional research, it would be interesting to research if the generators are capable of dealing with the fast-changing power demand. Currently, it is assumed that the asked power by the DP-system is delivered immediately. In reality, the vessel contains six generators of two different types. These generators need some time to start and have a limited power build-up per second. This could result in a difference between asked power by the DP-system and the delivered power by the generators, which will influence the station keeping ability of the vessel.

The pitch motion of the vessel is the governing limitation for the workability. Reducing the pitch motion while motions in the other Degrees of Freedom (DoF) do not increase will result in higher workability of the vessel. Therefore, researching the possibilities to reduce the pitch motions could be valuable. For vessels that operate on low velocities, anti-roll tanks, flume stabilising systems, or movable weight systems are used to reduce the roll motions [47]. Although a much larger moment is needed to influence the pitch motions significantly, these or similar systems might reduce the pitch motion. The maximum pitch angle limitation is considered to avoid a large swinging motion of the relative heavy vibro drill. The period that this swinging motion could occur is when the vibro drill is being placed at or removed from the top of the monopile. During the pile driving phase, when the vibro drill is at the top of the monopile, the swinging motion can not occur. The period that the swinging could occur is thus relative short. Another method to increase the workability is by making short term predictions of the critical pitch response. These predictions can be used to determine time windows with relative low pitch motion in which the vibro drill can be moved [48]. A pitch angle limitation with a larger value could be used, or the maximum pitch angle limitation could even be removed when this method is used.

Appendix A

Environmental forces

In this appendix some extra theory is explained to derive the environmental forces. This appendix can be seen as additional information to chapter 3. The additional symbols used in this appendix are shown in table A-1

Table A-1: Description of symbols

Symbol	Units	Description
ζ	m	Water profile
ζ_a	m	Wave amplitude
u	m/s	Wave particle velocity in x direction
v	m/s	Wave particle velocity in y direction
w	m/s	Wave particle velocity in z direction
m	kg	Mass of the rigid body
I	kgm^2	Moment of inertia
S	m^2	Wet surface of hull

A-1 Wave forces

This section explains how the wave forces that act on a vessel can be calculated. Any irregular sea state can be build-up by the sum of many simple sine waves, as shown in figure A-1. A simplification can be made to wave theory if deep or shallow water conditions are present. The water is considered to be deep if the water depth is more than half the wavelength, and the water is considered to be shallow if the water depth is less than 0.05 times the wavelength. Unfortunately, the water conditions at the installation sites of the North Sea are not always deep or shallow. Thus simplifications can not be made. The wave forces are split up in different orders. The first order linear wave theory is first explained, followed by the second-order forces. The wave height, water depth, and wave period of a wave determine which wave theory should be used to calculate the wave forces. This is shown in figure A-2. Most of the theory discussed in this section derives from [4].

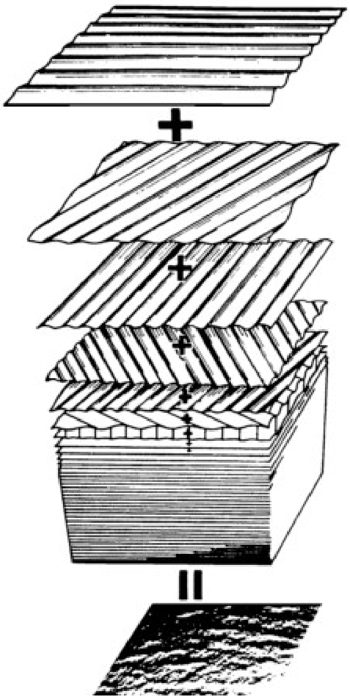

Figure A-1: An irregular sea is build up by many irregular sine waves [4]

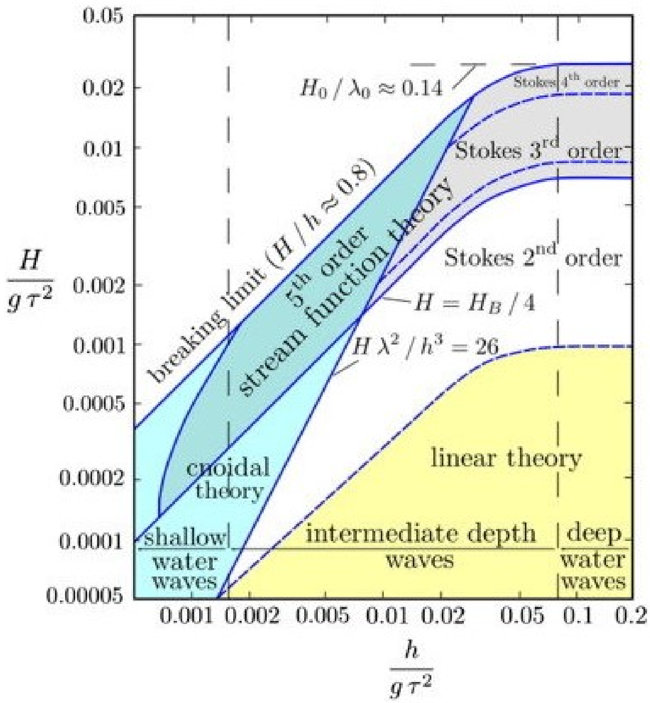

Figure A-2: Applicability of different wave theories

A-1-1 Wave potential of a regular wave

As explained in 3-1-1, in potential flow theory, a non-viscous model is used to describe the fluid dynamics [40]. In this theory it is assumed that the flow is homogeneous, irrotational, and incompressible. The water profile of a regular wave in the positive x-direction is described with equation A-1. This is the most basic way of describing a wave. Now, the potential flow of this wave is used, and boundary conditions are added to acquire the harmonic wave's velocity potential. The following four boundary conditions are applied.

$$\zeta = \zeta_a \cos(kx - \omega t) \tag{A-1}$$

Laplace equation Since the fluid is homogeneous and incompressible, the continuity equation A-2 holds. Equation A-3 describes that the spatial derivatives of the velocity potential equal the velocity components at a time and position [41]. If the velocity of water particles is inserted in the continuity equation, this results in the Laplace equation A-4. The Laplace equation must hold in any situation described by harmonic waves.

$$\frac{\partial u}{\partial x} + \frac{\partial v}{\partial y} + \frac{\partial w}{\partial z} = 0 \tag{A-2}$$

$$u = v_x = \frac{\partial \Phi_w}{\partial x} \quad v = v_y = \frac{\partial \Phi_w}{\partial y} \quad w = v_z = \frac{\partial \Phi_w}{\partial z} \tag{A-3}$$

$$\frac{\partial^2 \Phi}{\partial x^2} + \frac{\partial^2 \Phi}{\partial y^2} + \frac{\partial^2 \Phi}{\partial z^2} = 0 \tag{A-4}$$

Sea bed boundary condition The water depth is assumed to be limited, and water can not penetrate the sea bed. The second boundary condition states that the vertical velocity of water particles at the sea bed is zero, shown in equation A-5. This is also called a no-leak condition.

$$\frac{\partial \Phi_w}{\partial z} = 0 \quad \text{for: } z = -h \tag{A-5}$$

Free surface dynamic boundary condition The third boundary condition states that the pressure of the fluid at the free surface, p, is equal to the atmospheric pressure, p_0. This is shown in equation A-6. Assuming a non-stationary and irrotational flow, and applying the Bernoulli equation, results in the boundary condition of equation A-7. See section 5.2 of [4] for a more extensive explanation.

$$\mathrm{p} = \mathrm{p}_0 \text{ for } z = \zeta \tag{A-6}$$

$$\frac{\partial \Phi_w}{\partial t} + g\zeta = 0 \quad \text{for: } z = 0 \tag{A-7}$$

Free surface kinematic boundary condition The fourth boundary condition states that the vertical velocity of a water particle at the fluid's free surface is exactly the same as the vertical velocity of the free surface itself. This kinematic boundary condition is also called a no-leak condition. Using this condition and assuming small wave steepness results, which is always assumed in linear wave theory, results in equation A-8.

$$\frac{\partial z}{\partial t} + \frac{1}{g} \cdot \frac{\partial^2 \Phi_w}{\partial t^2} = 0 \quad \text{for: } z = 0 \tag{A-8}$$

Using equation A-1, applying the four boundary conditions and using potential theory, results in the velocity potential of a harmonic wave in the x-direction, this is shown in equation A-9. Of course, this potential can be rotated in other directions when the waves are comes from another direction.

$$\Phi_w = \frac{\zeta_a g}{\omega} \cdot \frac{\cosh k(h+z)}{\cosh kh} \cdot \sin(kx - \omega t) \tag{A-9}$$

A-1-2 Wave potentials for a vessel in waves

In this subsection, the wave potentials that influence a vessel floating in water are described by linear wave theory.

First order wave potentials To determine the three potentials which influence the vessel's motion, two extra boundary conditions are present. These additional boundary conditions are associated with the floating rigid body, which is now present.

$$\Phi(x, y, z; t) = \Phi_r + \Phi_w + \Phi_d \tag{A-10}$$

Radiation condition The radiation boundary condition states that very far away from the vessel, at a distance R, the radiation potential is zero. This means that the radiation waves will be damped out over a large distance. The radiation boundary condition is shown in equation A-11.

$$\lim_{R\to\infty} \Phi_r = 0 \tag{A-11}$$

Symmetric condition The second additional boundary condition states that the vessel that is considered is symmetric with its middle line plane. Most vessels have a symmetric hull shape. Thus this is a valid condition. This results in a simplification of potential equations, which is visible in equation A-12.

$$\begin{aligned} \Phi_2(-x, y) &= -\Phi_2(+x, y) \quad \text{for sway} \\ \Phi_3(-x, y) &= +\Phi_3(+x, y) \quad \text{for heave} \\ \Phi_4(-x, y) &= -\Phi_4(+x, y) \quad \text{for roll} \end{aligned} \tag{A-12}$$

Radiation potential The radiation potential is caused by an oscillating body in a sea without waves. This potential depends on the shape of the hull and the oscillation of the vessel. It can be written as the linear superposition of potentials in the six degrees of freedom. This is shown in equation A-13. The vessel's goal during the installation of a monopile is to reduce the vessel's motion as much as possible. This leads to small oscillation and a smaller radiation potential.

$$\Phi_r = \sum_{j=1}^{6} \Phi_{rj} \tag{A-13}$$

Undisturbed wave potential vs diffracted wave potential The undisturbed wave potential is shown in equation A-9. The kinematic boundary condition can also be used at the wet surface of the vessel's hull. The velocity of a water particle at the wet surface must be the same as the velocity of the wet surface itself. The velocity of the vessel is assumed to be zero for the undisturbed and diffracted wave potential. Thus the undisturbed and diffracted wave potential summed up is zero at the wet surface of the vessel's hull. This is shown in equation A-14 and A-15.

$$\frac{\partial \Phi_w}{\partial n} + \frac{\partial \Phi_d}{\partial n} = 0 \tag{A-14}$$

$$\frac{\partial \Phi_w}{\partial n} = -\frac{\partial \Phi_d}{\partial n} \tag{A-15}$$

A-1-3 First order wave forces and moments on a vessel

Using the linear wave theory and the known wave potentials, the linear first-order wave forces that act on a vessel can be calculated. The forces and moments can be calculated by integrating the pressure, p, over the wet surface, S, of the vessel. This is shown in equation A-16.

$$\begin{aligned} \vec{F} &= -\iint_S (p \cdot \vec{n}) \cdot dS \\ \vec{M} &= -\iint_S p \cdot (\vec{r} \times \vec{n}) \cdot dS \end{aligned} \tag{A-16}$$

Here $\vec{n}$ is the normal vector on the surface dS pointed in the direction of the water, and $\vec{r}$ is the position vector of the surface dS pointed from the point of rotation of the vessel. The pressure p is calculated with the linearized Bernoulli equation, shown in equation A-17. Here the velocity potential is inserted.

$$\begin{aligned} p &= -\rho \frac{\partial \Phi}{\partial t} - \rho g z \\ &= -\rho \left(\frac{\partial \Phi_r}{\partial t} + \frac{\partial \Phi_w}{\partial t} + \frac{\partial \Phi_d}{\partial t} \right) - \rho g z \end{aligned} \tag{A-17}$$

Now, the Bernoulli equation is inserted in the equation A-16. This results in equations A-18 and A-19, both have four different parts to calculate the forces and moments on the rigid body. Due to linearity, the radiation forces, the undisturbed wave forces, the diffracted forces, and the hydrostatic buoyancy forces can be calculated separately added to give the total hydrodynamic forces and moments [49]. The integrals are quite large and require much computational effort. A function called the Green's function G is developed to transform the large integral into a much easier to handle integral [41]. Understanding and explaining Green's function requires mathematical skills that are far beyond the scope of this master thesis. The total linear hydrodynamic forces and moments calculated by the Green's function cause the vessel to translate and rotate.

$$\vec{F} = \rho \iint_S \left(\frac{\partial \Phi_r}{\partial t} + \frac{\partial \Phi_w}{\partial t} + \frac{\partial \Phi_d}{\partial t} + gz \right) \vec{n} \cdot dS \tag{A-18}$$

$$\vec{M} = \rho \iint_S \left(\frac{\partial \Phi_r}{\partial t} + \frac{\partial \Phi_w}{\partial t} + \frac{\partial \Phi_d}{\partial t} + gz \right) (\vec{r} \times \vec{n}) \cdot dS \tag{A-19}$$

A-1-4 Non linear forces on the ship's hull

Dynamic Positioning (DP) systems filter the slow varying second order wave forces. Only the second order wave forces will be countered by the DP system. All the equations in this section come from [4], otherwise it will be indicated. Linear wave theory can not be used to calculate second order forces. In this section the forces at a point on the hull will be determined based on the direct integration method. Using this method forces on the vessel of the 0th, 1st and 2nd order are derived.

Pressures at the ship's hull Let's start with the non-linearized Bernoulli equation, shown in equation A-20. This is the fluid pressure at a single hull point. The subscript 3 for X means that this is the displacement in the heave direction. The equation can be solved if the velocity potential Φ is known.

$$p = -\rho g X_3 - \rho \frac{\partial \Phi}{\partial t} - \frac{1}{2}\rho(\vec{\nabla}\Phi)^2 \tag{A-20}$$

Assuming small first-order wave frequency motions $\vec{X}^{(1)}$ about a mean position $\vec{X}^{(0)}$, and applying a Taylor expansion, the pressure equation A-20 can be divided in the zero-order, first-order and second-order pressures. These can be found in equations A-21, A-22 and A-23. Here, the term order means that the wave amplitude is to the power of that order in that equation.

$$p^{(0)} = -\rho g X_3^{(0)} \tag{A-21}$$

$$p^{(1)} = -\rho g X_3^{(1)} - \rho \frac{\partial \Phi^{(1)}}{\partial t} \tag{A-22}$$

$$p^{(2)} = -\frac{1}{2}\rho\left(\vec{\nabla}\Phi^{(1)}\right)^2 - \rho\frac{\partial^2 \Phi^{(2)}}{\partial t^2} - \rho\left(\bar{X}^{(1)} \cdot \vec{\nabla}\frac{\partial \Phi^{(1)}}{\partial t}\right) \tag{A-23}$$

Using these different order pressures multiplied by the instantaneous normal vector $\vec{N}$ and integrated over the instantaneous wetted surface S, the fluid force on the ship's hull can be calculated. This integral is found in equation A-24. Here is the instantaneous wetted surface part S divided into a constant part S_0 and an oscillating part s. The fluid force will be divided into three parts; A hydrodynamic force $\vec{F}^{(0)}$, a first-order force $\vec{F}^{(1)}$ and a second-order force $\vec{F}^{(2)}$

$$\vec{F} = -\iint_S p \cdot \vec{N} \cdot dS \tag{A-24}$$

Hydrostatic fluid force The hydrostatic fluid force can be calculated by integrating the hydrostatic pressure over the mean wetted surface S_0. This is shown in equation A-25. $\vec{n}$ is the outwards pointing normal vector at the hull point.

$$\vec{F}^{(0)} = -\iint_{S_0}\left(p^{(0)} \cdot \vec{n}\right) \cdot dS \quad = (0, 0, \rho g \nabla) \tag{A-25}$$

First order force The first order force is shown in equation A-26. It contains three integrals; The hydrostatic pressure integrated over the constant part of the wet surface, the first order pressure integrated over the constant part of the wet surface and the hydrostatic pressure integrated over the oscillating part of the wet surface. $R^{(1)}$ is the linearized rotation transformation matrix and is shown in equation A-27. Here the subscripts 4, 5, and 6 stand for the roll, pitch, and yaw direction. More detailed steps on how to derive the second part of equation A-26 is found in Ch.9 of [4].

$$\begin{aligned}\vec{F}^{(1)} &= -\iint_{S_0}\left(p^{(0)}\cdot\vec{N}^{(1)}\right)\cdot dS - \iint_{S_0}\left(p^{(1)}\cdot\vec{n}\right)\cdot dS - \iint_{s}\left(p^{(0)}\cdot\vec{n}\right)\cdot dS \\ \vec{F}^{(1)} &= R^{(1)}\cdot(0,0,\rho g\delta)dS - \iint_{S_0}\left(p^{(1)}\cdot\vec{n}\right)\cdot dS\end{aligned} \tag{A-26}$$

$$R^{(1)} = \begin{bmatrix} 0 & -x_6^{(1)} & +x_5^{(1)} \\ +x_6^{(1)} & 0 & -x_4^{(1)} \\ -x_5^{(1)} & +x_4^{(1)} & 0 \end{bmatrix} \tag{A-27}$$

Second order force The second-order drift force is shown in equation A-28. It contains four integrals; the first order pressure integrated over the constant part of the wetted surface, the second-order pressure integrated over the constant part of the wetted surface, the hydrostatic pressure integrated over the oscillating part of the wetted surface, which results in zero, and the first-order pressure integrated over the oscillating part of the wetted surface. Substituting equation A-21, A-22 and A-23 in equation A-28 and using equation A-29 results in equation A-30.

$$\begin{aligned}\vec{F}^{(2)} = &-\iint_{S_0}\left(p^{(1)}\cdot\vec{N}^{(1)}\right)\cdot dS - \iint_{S_0}\left(p^{(2)}\cdot\vec{n}\right)\cdot dS \\ &-\iint_{s}\left(p^{(0)}\cdot\vec{N}^{(1)}\right)\cdot dS - \iint_{s}\left(p^{(1)}\cdot\vec{n}\right)\cdot dS\end{aligned} \tag{A-28}$$

$$\vec{F}^{(1)} - R^{(1)}\cdot(0,0,\rho g\nabla) = m\cdot\vec{X}_G^{(1)} \tag{A-29}$$

$$\begin{aligned}\vec{F}^{(2)} = &\, m\cdot R^{(1)}\cdot\ddot{X}_G^{(1)} \\ &+\iint_{S_0}\left\{\frac{1}{2}\rho\left(\vec{\nabla}\Phi^{(1)}\right)^2 + \rho\frac{\partial\Phi^{(2)}}{\partial t} + \rho\bar{X}^{(1)}\cdot\vec{\nabla}\frac{\partial\Phi^{(1)}}{\partial t}\right\}\cdot\vec{n}\cdot dS \\ &-\oint_{wl}\frac{1}{2}\rho g\left(\zeta_r^{(1)}\right)^2\cdot\vec{n}\cdot dl\end{aligned} \tag{A-30}$$

In a similar way, the second-order wave moment is determined. The result is also obtained by four integrals and is shown in equation A-31.

$$\begin{aligned}\vec{M}^{(2)} = &\, I\cdot R^{(1)}\cdot\ddot{X}_G^{(1)} \\ &+\iint_{S_0}\left\{\frac{1}{2}\rho\left(\vec{\nabla}\Phi^{(1)}\right)^2 + \rho\frac{\partial\Phi^{(2)}}{\partial t} + \rho\cdot\vec{X}^{(1)}\cdot\vec{\nabla}\frac{\partial\Phi^{(1)}}{\partial t}\right\}\cdot(\vec{x}\times\vec{n})\cdot dS \\ &-\oint_{wl}\frac{1}{2}\rho g\left(\zeta_r^{(1)}\right)^2\cdot(\vec{x}\times\vec{n})\cdot dl\end{aligned} \tag{A-31}$$

The expressions for the second-order drift forces and moments, equations A-30 and A-31 are evaluated at MARIN. Computations for multiple cases are performed, and the results have been compared with analytical solutions and the results of model tests. It is concluded that the computations give quite good results and are comparable with the analytical solutions and the results of model tests [4].

Quadratic transfer functions As long as long-crested irregular waves are considered, the second-order force can be calculated with time-invariant Quadratic transfer functions (QTF) [42]. With equations A-30 and A-31 as input, QTF's for the mean and low-frequency drift forces can be formed. These low-frequency forces are mainly formed by the difference of frequency pairs ω_i and ω_j, which are called difference frequencies. The low-frequency second-order wave force is described by equation A-32. Here $\tilde{\varepsilon}_i$ and $\tilde{\varepsilon}_j$ are the phase shifts due to the difference frequencies.

$$\begin{aligned} F_1^{(2)}(t) = &\sum_{i=1}^{N}\sum_{j=1}^{N} \zeta_i^{(1)}\zeta_j^{(1)} P_{ij} \cdot \cos\left\{(\omega_i - \omega_j)\, t + (\tilde{\varepsilon}_i - \tilde{\varepsilon}_j)\right\} \\ &+ \sum_{i=1}^{N}\sum_{j=1}^{N} \zeta_i^{(1)}\zeta_j^{(1)} Q_{ij} \cdot \sin\left\{(\omega_i - \omega_j)\, t + (\tilde{\varepsilon}_i - \tilde{\varepsilon}_j)\right\} \end{aligned} \tag{A-32}$$

In this equation, P_{ij} and Q_{ij} are the QTF's, which are in-phase and out-of-phase of the low-frequency part of the square of the incident waves. If all the QTF's which contribute to the second-order drift force are considered, the total second-order wave drift force can be calculated with equation A-32. More explanation about the formation of this equation and an example of how to calculate a QTF can be found in Ch.9 of [4]. The absolute QTF value can be calculated with A-33. Some software programs, for example ANSYS AQWA, make use of the approximations by Newman to reduce the computations effort of calculating the second-order forces with QTF's [42]. The approximations by Newman can be found in equations A-34 and A-35. These approximations give satisfactory results because P_{ij}^{-} and P_{ji}^{-} generally do not change very much with frequency, and the most interesting results of these QTF's are present when ω_i is close to ω_j [49].

$$|T_{ij}| = \sqrt{P_{ij}^2 + Q_{ij}^2} \tag{A-33}$$

$$Q_{ij} = Q_{ji} = 0 \tag{A-34}$$

$$P_{ij}^{-} = P_{ji}^{-} = 0.5\left(P_{ii}^{-} + P_{jj}^{-}\right) \tag{A-35}$$

A-1-5 Directional spreading

There are multiple methods to account for directional spreading. The cosine-squared rule is shown in equation A-36 [4]. Here the chosen wave spectrum $S_\zeta(\omega)$ is spread out over a directional range. The $\bar{\mu}$ represents the dominant wave direction. This method is used in the study of [16].

$$
\begin{aligned}
S_\zeta(\omega,\mu) &= \left\{\frac{2}{\pi}\cdot\cos^2(\mu-\bar{\mu})\right\}\cdot S_\zeta(\omega) \\
\text{with :} \qquad & -\frac{\pi}{2} \leq (\mu-\bar{\mu}) \leq +\frac{\pi}{2}
\end{aligned}
\tag{A-36}
$$

Another method to distribute the energy of a wave spectrum is to use equation A-37 [22]. Here again, a wave spectrum $S_\zeta(\omega)$ is spread out due to the directional spreading $D(\mu,\omega)$, shown in equation A-38. Equation A-39 ensures that the waves can come from all angles. Here $N(s)$, calculated by A-40, ensures that the integral of D stays 1, s describes how much the waves are spread out over the directions. For a larger s, the waves will become more concentrated in a single direction.

$$E(\mu,\omega) = S_\zeta(\omega)D(\mu,\omega) \tag{A-37}$$

$$D(\theta,\omega) = N(s)\cos^{2s}\left(\frac{\theta-\theta_1}{2}\right) \tag{A-38}$$

$$\int_{\mu=0}^{2\pi} D(\mu,\omega)d\mu = 1 \tag{A-39}$$

$$N(s) = \frac{1}{\pi}2^{2s-1}\frac{\Gamma^2(s+1)}{\Gamma(2s+1)} \tag{A-40}$$

Another method to account for directional spreading is shown in the study of [1]. Here the choice is made to shift the two most critical environmental conditions 15 degrees and used those in the simulations. This results in less critical environmental situations.

A-2 Wind forces

Unless indicated otherwise, equation A-41 can be used to calculate the average wind speed U with the average wind period, T, at a height z above the sea level [12].

$$U(T,z) = U_{10}\cdot\left(1+0.137\ln\left(\frac{z}{H}\right)-0.047\ln\left(\frac{T}{T_{10}}\right)\right) \tag{A-41}$$

With the following parameters:

$T_{10} = 10$ minutes

$h = 10$ m

$U_{10} = 10$ minutes mean wind speed at height h

The wind speed variation in time is generally represented by the standard deviation σ_U. The spectral density of the wind speed is frequently represented by the Kaimal spectrum, which is shown in equation A-42 [12]. The standard deviation is of great importance in this spectrum. In this equation, f is the wind frequency, and the integral scale parameter L_k needs to be taken as indicated in equation A-43. Another frequently used wind spectrum is the NPD spectrum, which is shown in equation A-44 [33]. Here n is 0.468 and t is defined in A-45.

$$S_{U_{Kaimal}}(f) = \sigma_U^2 \frac{4\frac{L_k}{U_{wind}}}{\left(1 + 6\frac{fL_k}{U_{wind}}\right)^{5/3}} \tag{A-42}$$

$$L_k = \begin{cases} 5.67z & \text{for } z < 60 \text{ m} \\ 340.2 \text{ m} & \text{for } z \geq 60 \text{ m} \end{cases} \tag{A-43}$$

$$S_{U_{NPD}}(f) = \frac{320}{2\pi}\left(\frac{U_{10}}{10}\right)^2 \frac{1}{(1+t^n)^{5/3n}} \tag{A-44}$$

$$t = 172f\left(\frac{U_{10}}{10}\right)^{-0.75} \tag{A-45}$$

Equation 3-4 shows how to calculate the wind and current forces on the monopile and vessel. Another way of calculating the wind forces on the monopile is shown in equation A-46, here the variation on wind speed over height is considered as well. The smaller the vertical integration step is taken, the more accurate the wind load force is calculated.

$$F_w = 0.5 * \rho_{air} * C_D * D * dz * U(T,z)^2 \tag{A-46}$$

With the following parameters:

D = Diameter of the monopile

C_D = Wind coefficient of monopile

dz = Vertical integration step

A-3 Current forces

The current speed consist of a wind-generated current and a tidal current [12], see equation A-47. The wind-generated current and tidal current can be calculated with equations A-49 and A-48. They both vary over the depth z.

$$v(z) = v_{\text{tide}}(z) + v_{\text{wind}}(z) \tag{A-47}$$

$$v_{tide}(z) = v_{tide0}\left(\frac{h+z}{h}\right)^{1/7} \quad \text{for } z \leq 0 \tag{A-48}$$

$$v_{\text{wind}}\ (z) = v_{\text{wind } 0} \cdot \left(\frac{h_0 + z}{h_0}\right) \text{ for } -h_0 \leq z \leq 0 \tag{A-49}$$

With the following parameters:

$v(z)$ = total current velocity

z = vertical coordinate

v_{tide0} = tidal current at still water line

v_{wind0} = wind-generated current at still water line

h = water depth

$h_0 = 0$ = reference depth for wind generated currents

The tidal current speed at the still water line is entirely dependent on the location. Before starting the installation operation, the tidal velocity on the installation site must be checked, and the wind-generated current should be estimated. Unless data indicate otherwise, the wind-generated current at still water level may be estimated by equation A-50 [12].

$$v_{\text{wind } 0} = k \cdot U_0 \tag{A-50}$$

With the following parameters:

$k = 0.015$ to 0.03

U_0 = 1-hour mean wind speed at 10 m height

Appendix B

Motions of the vessel

Chapter 3 explains how the environmental forces on a vessel can be determined. In this chapter, these forces are used to explain how the vessel responds. The vessel's response can be determined motion Response Amplitude Operator (RAO)'s. The motion RAO's differ for each degree of freedom and for each wave frequency.

B-1 Newton's second law

Newton's second law can be used to determine the vessel's motions, which is shown in equation B-1. As shown in section 3-1-1, the wave forces are split up into three parts, the radiation force, incoming wave force, and the diffraction force. Next to these wave forces, the hydrostatic buoyancy force must be added here [22]. The summation of forces is shown in equation B-2.

$$\sum F = m \cdot a \tag{B-1}$$

$$\sum F = F_r + F_w + F_d + F_s \tag{B-2}$$

With:

F_r = Radiation forces

F_w = Incoming undisturbed wave forces

F_d = Diffraction forces

F_s = Hydrostatic buoyancy forces

Mass matrix The vessel consists of six degrees of freedom, thus the mass matrix is a 6x6 matrix shown in equation B-3. Here m is the mass of the vessel and I_{xx}, I_{yy} and I_{zz} are the moments of inertia, which is calculated with equation B-4. Here k_{xx}, k_{yy} and k_{zz} are the radii of inertia of the vessel.

$$\boldsymbol{m} = \begin{bmatrix} m & 0 & 0 & 0 & 0 & 0 \\ 0 & m & 0 & 0 & 0 & 0 \\ 0 & 0 & m & 0 & 0 & 0 \\ 0 & 0 & 0 & I_{xx} & 0 & 0 \\ 0 & 0 & 0 & 0 & I_{yy} & 0 \\ 0 & 0 & 0 & 0 & 0 & I_{zz} \end{bmatrix} \tag{B-3}$$

$$I_{xx} = k_{xx}^2 \cdot \rho\nabla; \qquad I_{yy} = k_{yy}^2 \cdot \rho\nabla; \qquad I_{zz} = k_{zz}^2 \cdot \rho\nabla \tag{B-4}$$

Added mass and hydrodynamical damping When the vessel moves, the water around the vessel moves with it. The water accelerates due to the vessel's radiation force. Due to the acceleration of water around the hull, added mass, and hydrodynamic damping needs to be added in equation B-1, the result is shown in equation B-5 [22]. The added mass and hydrodynamical damping are dependent on the motion frequency. Thus this equation is written in the frequency domain. This means that the frequencies of the vessel's motions, which are continuous, needs to be split up in small discrete frequency steps. For each frequency, the added mass and hydrodynamical damping need to be determined.

$$\begin{aligned} \{-\omega^2 & \begin{vmatrix} m+a_{11} & a_{12} & a_{13} & a_{14} & a_{15} & a_{16} \\ a_{21} & m+a_{22} & a_{23} & a_{24} & a_{25} & a_{26} \\ a_{31} & a_{32} & m+a_{33} & a_{34} & a_{35} & a_{36} \\ a_{41} & a_{42} & a_{43} & I_{xx}+a_{44} & a_{45} & a_{46} \\ a_{51} & a_{52} & a_{53} & a_{54} & I_{yy}+a_{55} & a_{56} \\ a_{61} & a_{62} & a_{63} & a_{64} & a_{65} & I_{zz}+a_{66} \end{vmatrix} \\ +i\omega & \begin{vmatrix} B11_{add}+b_{11} & b_{12} & b_{13} & b_{14} & b_{15} & b_{16} \\ b_{21} & B22_{add}+b_{22} & b_{23} & b_{24} & b_{25} & b_{26} \\ b_{31} & b_{32} & b_{33} & b_{34} & b_{35} & b_{36} \\ b_{41} & b_{42} & b_{43} & B44_{add}+b_{44} & b_{45} & b_{46} \\ b_{51} & b_{52} & b_{53} & b_{54} & b_{55} & b_{56} \\ b_{61} & b_{62} & b_{63} & b_{64} & b_{65} & B66_{add}+b_{66} \end{vmatrix} \\ + & \begin{vmatrix} c_{11} & c_{12} & c_{13} & c_{14} & c_{15} & c_{16} \\ c_{21} & c_{22} & c_{23} & c_{24} & c_{25} & c_{26} \\ c_{31} & c_{32} & c_{33} & c_{34} & c_{35} & c_{36} \\ c_{41} & c_{42} & c_{43} & c_{44} & c_{45} & c_{46} \\ c_{51} & c_{52} & c_{53} & c_{54} & c_{55} & c_{56} \\ c_{61} & c_{62} & c_{63} & c_{64} & c_{65} & c_{66} \end{vmatrix} \} \cdot \begin{vmatrix} x \\ y \\ z \\ \phi \\ \theta \\ \psi \end{vmatrix} = \begin{vmatrix} F_x \\ F_y \\ F_z \\ M_x \\ M_y \\ M_z \end{vmatrix} \end{aligned} \tag{B-5}$$

Viscous damping The vessel motion damping, as explained before, is damping caused by the radiation waves. These waves dissipate energy from the moving vessel. The viscous damping effect is neglected so far in this chapter. The major part of damping is caused by the radiation waves. Thus for most directions, the viscous damping could indeed be neglected. But, the viscous damping plays a significant role in the total roll damping [1], [22]. This is because the roll radiation damping could be very small itself [4]. The overall radiation roll damping mainly depends on the breadth-draught ratio of a vessel. When this ratio is close to 2.5, the radiation roll damping is relatively small; see figure B-1a. This is because the hull of a vessel with such a ratio has a 'more or less' circular cross-section; see figure B-1b. The viscous roll damping could consist of bilge keel damping, lift damping, eddy making damping, friction damping, and wave damping [4]. The viscous roll damping, B_{44}, should be estimated for the vessel and inserted in the equation of motion, this is done in equation B-5.

In this model, some extra viscous damping is added in surge, sway and yaw direction. Quadratic viscous damping is non-linear with velocity and amplitude, and should be added to equation B-5 [45].

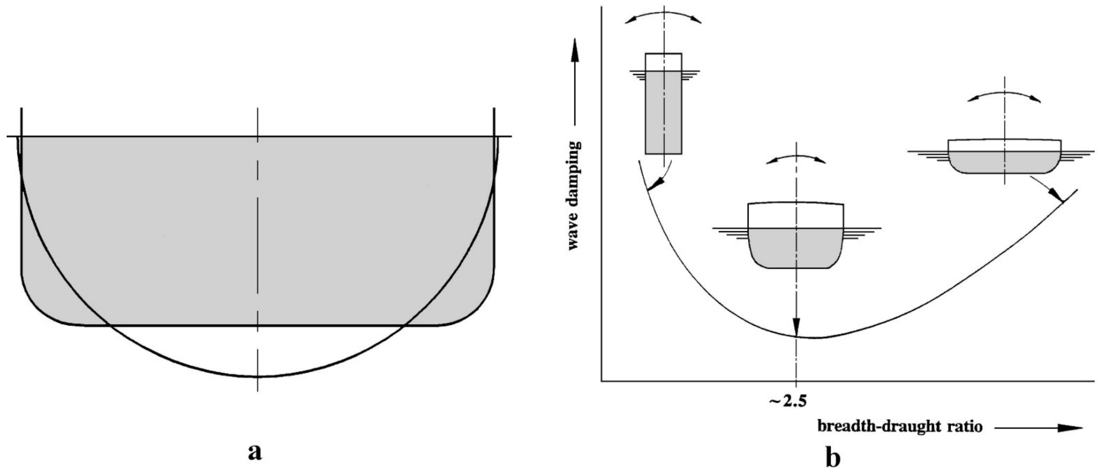

Figure B-1: Radiation roll damping as function of breadth-draught ratio

B-2 Motion RAO's

When the added mass, the hydrodynamic damping, and the viscous damping are known, the equation of motion is filled in completely, see equation B-5. The simplified version of this equation is found in equation B-6. Now the transfer function between the forces shown on the right side of this equation and the wave amplitude is formed. This transfer function is shown in equation B-7 [22], it differs for every frequency and incoming wave direction.

$$\left(-\omega^2(\boldsymbol{m}+\boldsymbol{A})+i\omega\left(\boldsymbol{B}+\boldsymbol{B_{add}}\right)+\boldsymbol{C}\right)\boldsymbol{X}=\boldsymbol{F}_W+\boldsymbol{F_D} \tag{B-6}$$

$$H_{fz}(\omega,\mu)=\frac{F_D+F_W}{\zeta_a} \tag{B-7}$$

With the help of this transfer function, the motion RAO's can be calculated. The motion RAO, which contains the transfer function in all six degrees of freedom, is shown in equation

B-8. Each RAO contains a real and an imaginary part. In equations B-9 and B-10 is shown how the amplitude and the phase angles of the RAO's can be calculated. Due to the large matrices that the RAO of equation B-8 contains, it is hard to work with.

$$RAO(\omega,\mu) = \frac{H_{fz}(\omega,\mu)}{-\omega^2(m + A(\omega)) + i\omega\left(B(\omega) + B_{add}\right) + C} \tag{B-8}$$

$$RAO_a = \sqrt{\mathrm{Re}(RAO)^2 + \mathrm{Im}(RAO)^2} \tag{B-9}$$

$$\epsilon = \arctan\left(\frac{\mathrm{Im}(RAO)}{\mathrm{Re}(RAO)}\right) \tag{B-10}$$

Appendix C

Current and wind coefficients

C-1 Stella Synergy's coefficients

$\theta[^\circ]$	C_x	C_y	C_ψ
0	1.013	-0.003	0.01
15	1.01	0.156	0.012
30	1.024	0.374	-0.007
45	0.902	0.596	-0.017
60	0.595	0.795	-0.009
75	0.168	0.921	0.005
90	-0.118	0.985	0.029
105	-0.295	0.993	0.052
120	-0.459	0.932	0.071
135	-0.49	0.823	0.089
150	-0.661	0.596	0.079
165	-0.771	0.299	0.044
180	-0.732	0.032	-0.004
195	-0.758	-0.375	-0.065
210	-0.667	-0.671	-0.099
225	-0.543	-0.886	-0.106
240	-0.501	-0.979	-0.085
255	-0.325	-1.01	-0.054
270	-0.226	-1.01	-0.034
285	0.051	-0.939	-0.005
300	0.501	-0.823	0.019
315	0.862	-0.637	0.035
330	1.005	-0.423	0.033
345	1.03	-0.196	0.02

Table C-1: Wind coefficients for the Stella Synergy

$\theta[^\circ]$	C_x	C_y	C_ψ
000,	0.20	0.00	0.00
030,	0.28	0.23	-0.059
060,	0.23	0.54	-0.067
090,	-0.22	0.67	-0.16
120,	-0.03	0.54	0.045
150,	-0.022	0.20	0.045
180,	-0.20	0.00	0.00
210,	-0.022	-0.20	-0.045
240,	-0.03	-0.54	-0.045
270,	-0.22	-0.67	0.016
300,	0.23	-0.54	0.067
330,	0.28	-0.23	0.059

Table C-2: Current coefficients for the Stella Synergy

C-2 Monopile's coefficients

$\theta[°]$	C_x	C_y
0	0.700	0.000
15	0.676	0.181
30	0.606	0.350
45	0.495	0.495
60	0.350	0.606
75	0.181	0.676
90	0.000	0.700
105	-0.181	0.676
120	-0.350	0.606
135	-0.495	0.495
150	-0.606	0.350
165	-0.676	0.181
180	-0.700	0.000
195	-0.676	-0.181
210	-0.606	-0.350
225	-0.495	-0.495
240	-0.350	-0.606
255	-0.181	-0.676
270	0.000	-0.700
285	0.181	-0.676
300	0.350	-0.606
315	0.495	-0.495
330	0.606	-0.350
345	0.676	-0.181

Table C-3: Wind coefficients for the monopile

$\theta[°]$	C_x	C_y
0	0.680	0.000
15	0.657	0.176
30	0.589	0.340
45	0.481	0.481
60	0.340	0.589
75	0.176	0.657
90	0.000	0.680
105	-0.176	0.657
120	-0.340	0.589
135	-0.481	0.481
150	-0.589	0.340
165	-0.657	0.176
180	-0.680	0.000
195	-0.657	-0.176
210	-0.589	-0.340
225	-0.481	-0.481
240	-0.340	-0.589
255	-0.176	-0.657
270	0.000	-0.680
285	0.176	-0.657
300	0.340	-0.589
315	0.481	-0.481
330	0.589	-0.340
345	0.657	-0.176

Table C-4: Current coefficients for the monopile

Appendix D

North sea wave conditions

		Hs [m]											
		Lower	0	0.5	1	1.5	2	2.5	3	3.5	4	4.5	5	5.5
	Lower	Upper	0.5	1	1.5	2	2.5	3	3.5	4	4.5	5	5.5	6
	2	3	0.03	0.03										
	3	4	0.49	1.01	0.16									
	4	5	1.05	4.86	2.96	0.26	0.01							
	5	6	0.31	5.08	7.68	3.49	0.5	0.02						
Tp [s]	6	7	0.39	3.39	6.9	6.41	3.91	1.05	0.14	0.01				
	7	8	0.25	1.95	4.12	4.03	3.99	2.7	1.03	0.17	0.01			
	8	9	0.23	1.88	2.67	2.27	2.1	1.78	1.67	0.96	0.27	0.04		
	9	10	0.13	1.05	1.97	1.67	1.06	0.79	0.61	0.72	0.59	0.34	0.13	0.02
	10	11	0.1	0.45	0.8	1.09	0.77	0.33	0.17	0.19	0.22	0.18	0.18	0.06
	11	12	0.05	0.33	0.36	0.53	0.45	0.31	0.18	0.08	0.05	0.06	0.1	0.03
	12	13	0.06	0.2	0.19	0.17	0.11	0.16	0.13	0.06	0.02			
	13	14	0.01	0.1	0.08	0.07	0.06	0.08	0.08	0.04	0.04	0.01	0.01	
	14	15												

Figure D-1: Scatter diagram with the wave conditions of the North Sea

Appendix E

DP-gains

The original Dynamic Positioning (DP)-gains, which were optimised for Hs=3.0 m and Tp=9.0 s, are shown in table E-1.

Table E-1: Original DP-gains, optimised for Hs=3.0 m and Tp=9.0 s

	Surge gains	Sway gains	Yaw gains
Kp	520000 [N/m]	1174000 [N/m]	609000000 [N/rad]
Ki	4350 [N/ms]	1740 [N/ms]	2174000 [N/rads]
Kd	17400000 [Ns/m]	13900000 [Ns/m]	16520000000 [Ns/rad]

The halved DP-gains, used for sea conditions with a wave peak period larger than 10 s, are shown in table E-2.

Table E-2: Halved DP-gains, used for sea conditions with a wave peak period larger than 10 s.

	Surge gains	Sway gains	Yaw gains
Kp	260000 [N/m]	587000 [N/m]	304500000 [N/rad]
Ki	2175 [N/ms]	870 [N/ms]	1087000 [N/rads]
Kd	8700000 [Ns/m]	6950000 [Ns/m]	8260000000 [Ns/rad]

Appendix F

Viscous damping components

Here the results for the decay tests in surge, sway and yaw are given. The part between the two red lines is the decay test of Maritiem Research Instituut Nederland (MARIN). The part that fully covers the figure is the decay test in Anysim.

F-1 Surge decay

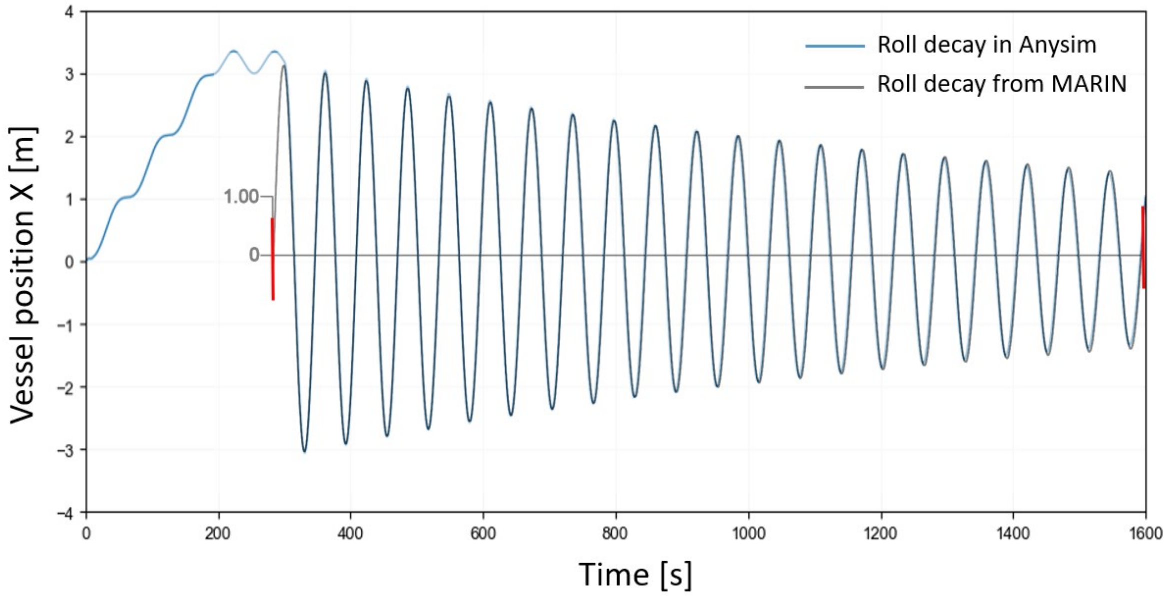

Figure F-1: Superimposition of two surge decay tests

F-2 Sway decay

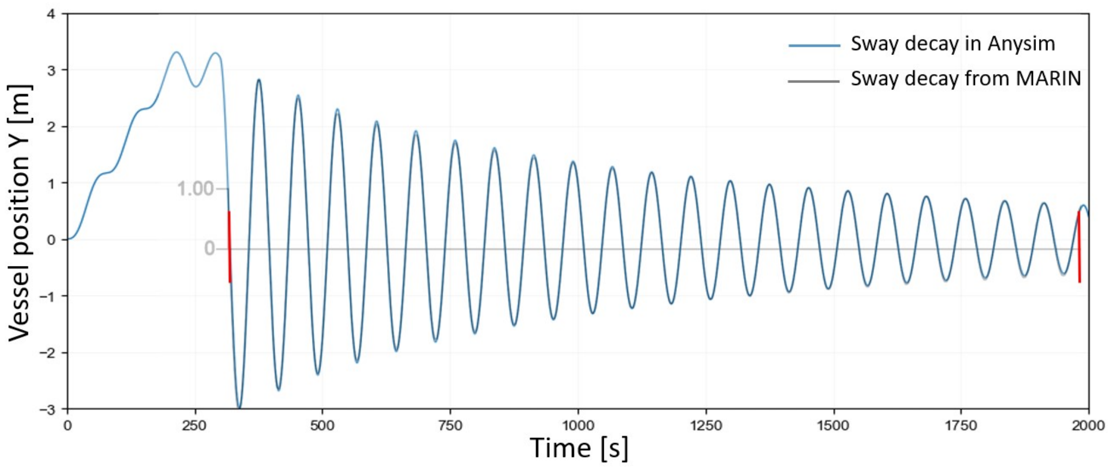

Figure F-2: Superimposition of two sway decay test

F-3 yaw decay

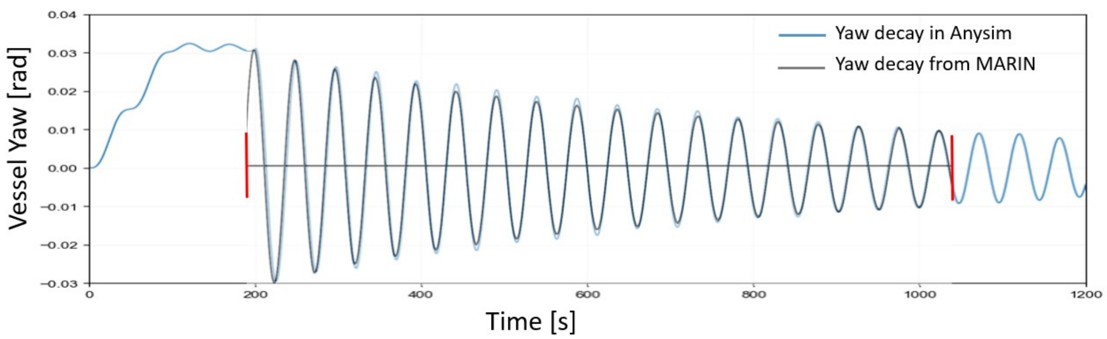

Figure F-3: Superimposition of two yaw decay test

F-4 Viscous damping components

Table F-1: Linear and quadratic viscous damping components

	Lin [kNs/m]	Qua [kNsm]
Surge (B_{11})	36	26
Sway (B_{22})	55	230
	Lin [kNs^2/m^2]	Qua [kNms^2]
Roll (B_{44})	90000	140000
Yaw (B_{66})	437420	250000

Appendix G

Gripper's capability

Here the gripper's capability is shown for simulation with a constant wave peak period of 8.5 s and varying significant wave height from 0.75 m to 4.75 m. All these runs are considered to be workable.

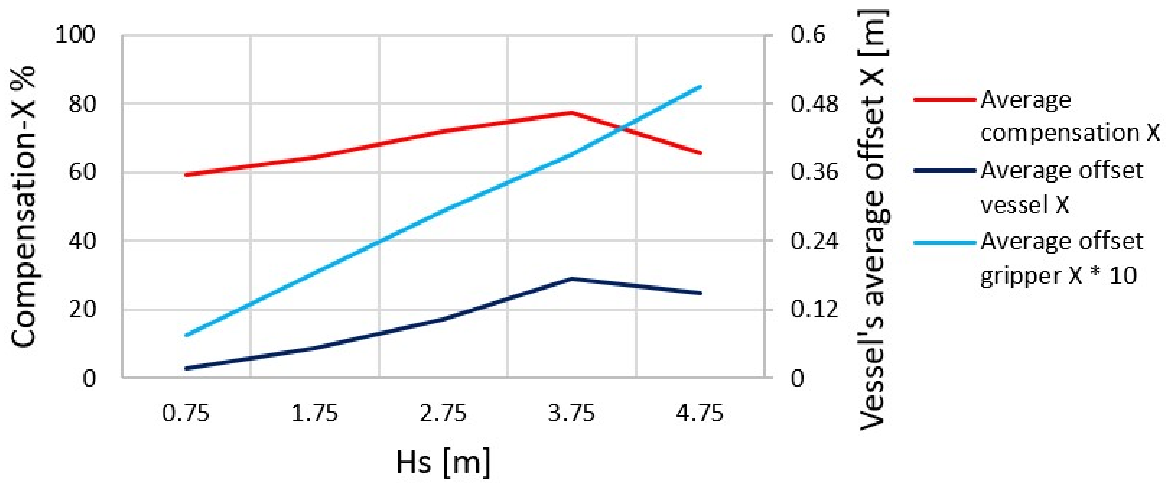

Figure G-1: Gripper's motion compensation in x-direction with varying Hs for Tp=8.5 s

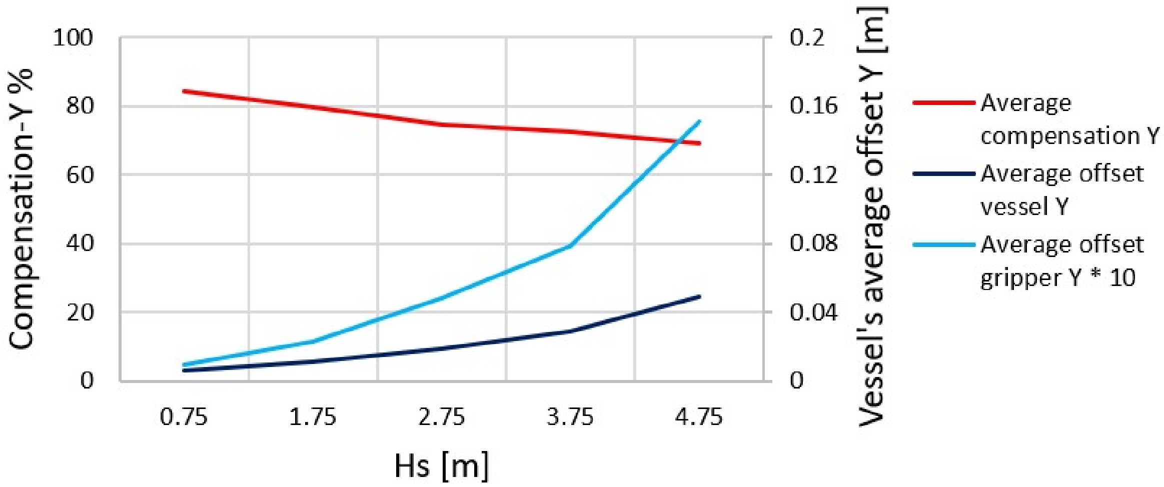

Figure G-2: Gripper's motion compensation in y-direction with varying Hs for Tp=8.5 s

Appendix H

Workability for an incoming angle of 185 degrees

The total workability for an incoming angle of 185 degrees is shown in figure H-1. The workability percentages for the separate limitation criteria are shown in table 5-2.

Hs [m]

Tp [s]

	Lower	0	0.5	1	1.5	2	2.5	3	3.5	4	4.5	5	5.5	
Lower	Upper	0.5	1	1.5	2	2.5	3	3.5	4	4.5	5	5.5	6	SUM
2	3	0.03	0.03											0.05
3	4	0.49	1.01	0.16										1.66
4	5	1.05	4.86	2.96	0.26	0.01								9.14
5	6	0.31	5.08	7.68	3.49	0.5	0.02							17.1
6	7	0.39	3.39	6.9	6.41	3.91	1.05	0.14	0.01					22.2
7	8	0.25	1.95	4.12	4.03	3.99	2.7	1.03	0.17	0.01				18.3
8	9	0.23	1.88	2.67	2.27	2.1	1.78	1.67	0.96	0.27	0.04			13.9
9	10	0.13	1.05	1.97	1.67	1.06	0.79	0.61	0.72	0.59	0.34	0.13	0.02	7.99
10	11	0.1	0.45	0.8	1.09	0.77	0.33	0.17	0.19	0.22	0.18	0.18	0.06	1.35
11	12	0.05	0.33	0.36	0.53	0.45	0.31	0.18	0.08	0.05	0.06	0.1	0.03	0.38
12	13	0.06	0.2	0.19	0.17	0.11	0.16	0.13	0.06	0.02				0.26
13	14	0.01	0.1	0.08	0.07	0.06	0.08	0.08	0.04	0.04	0.01	0.01		0.01
14	15													

92.2 %

Figure H-1: Scatter diagram for the workability for an incoming angle of 185 degrees
Yellow-orange = workable
Blue = non-workable
Red = non-workable, while it was workable for an incoming angle of 180 degrees

Table H-1: Workability of separate limitations for an incoming angle of 180 and 185 deg and constant gains

Limitations:	Workability 180 deg[%]	Workability 185 deg[%]
Footprint-x	93.3	93.3
Footprint-y	94.7	94.9
Roll	97.4	97.1
Pitch	97.0	97.0
Inclination angle	93.8	95.5
velocity gripper	93.8	94.2
Total	92.3	92.2

Bibliography

[1] J. Bottemanne, “Workability Analysis of a Floating XL-Monopile Installation A vessel motion study,” tech. rep., Thesis project at TU Delft, 2020.

[2] E. W. Weisstein, “Cylinder Drag – from Eric Weisstein’s World of Physics.”

[3] J. Velarde, “Design of Monopile Foundations to Support the DTU 10 MW Offshore Wind Turbine,” Tech. Rep. June, TU Delft, 2016.

[4] J. M. J. Journée and W. W. Massie, “OFFSHORE HYDROMECHANICS First Edition,” tech. rep., TU Delft, 2001.

[5] UNFCCC, “The Paris Agreement | UNFCCC,” 2018.

[6] M. Ortega-Izquierdo and P. Del Río, “Benefits and costs of renewable electricity in Europe,” aug 2016.

[7] Martha Ekkert, “Global energy transformation: a roadmap to 2050,” tech. rep., IRENA, 2018.

[8] M. D. Esteban, J. J. Diez, J. S. López, and V. Negro, “Why offshore wind energy?,” feb 2011.

[9] A. R. Henderson, C. Morgan, B. Smith, H. C. Sørensen, R. J. Barthelmie, and B. Boesmans, “Offshore wind energy in europe - A review of the state-of-the-art,” 2003.

[10] W. Musial and S. Butterfield, “Future for Offshore Wind Energy in the United States: Preprint,” tech. rep., National Renewable Energy Laboratory, 2004.

[11] G. B. Lizet Ramírez, Daniel Fraile, “Offshore Wind in Europe key trends and statistics 2019,” tech. rep., Wind Europe, 2020.

[12] DNV, “DNV-OS-J101 Design of Offshore Wind Turbine Structures,” Tech. Rep. May, DNVGL, 2014.

[13] V. Smil, "Wind Turbines Just Keep Getting Bigger, But There's a Limit - IEEE Spectrum," 2019.

[14] General Electric, "World's Most Powerful Offshore Wind Platform: Haliade-X | GE Renewable Energy," 2020.

[15] T. works design, "Offshore wind Installation Engineering of the future," tech. rep., Temporary works design, 2019.

[16] L. G. Buitendijk and S. A. Miedema, "Floating installation of offshore wind turbine foundations "An Engineering Assessment on Ship-Monopile Interaction during Pile Driving"A. Marchée Van Oord Dredging and Marine Contractors," tech. rep., Thesis project at TU Delft, 2016.

[17] C. Moné, A. Smith, B. Maples, and M. Hand, "2013 Cost of Wind Energy Review," tech. rep., National Renewable Energy Laboratory, 2013.

[18] E. A. Hansen, "Site Studies Wind Farm Zone Borssele," tech. rep., Netherlands Enterprise Agency, 2015.

[19] TWD, "Motion Compensated Pile Gripper," 2020.

[20] Seaway7, "WTG - Foundations," 2021.

[21] M. Wittingen -Bsc, "Offshore Wind Turbine Monopile Foun-dation Installation with a Dynamic Posi-tioned Vessel A feasibility study by modeling," tech. rep., TU Delft, 2018.

[22] G. A. Van Der Veen, "Monopile upend-ing workability and techniques," tech. rep., Thesis project at TU Delft, 2019.

[23] J. Crol, "Upending of a Monopile for an Offshore Wind Turbine Foundation," Tech. Rep. December, Tu Delft, 2015.

[24] K. van der Heiden, "Jumbo confidential information," tech. rep., Jumbo Maritime, 2021.

[25] L. Li, "Dynamic Analysis of the Installation of Monopiles for Offshore Wind Turbines," tech. rep., Faculty of Engineering Science and TechnologyDepartment of Marine Technology, Trondhein, 2016.

[26] L. Li, Z. Gao, T. Moan, and H. Ormberg, "Analysis of lifting operation of a monopile for an offshore wind turbine considering vessel shielding effects," *Marine Structures*, vol. 39, pp. 287–314, dec 2014.

[27] B. BJM Arntz, "Developing the Vibro-drill; A feasibility study into an improved installation method for offshore foundation piles," tech. rep., TU Delft, DELFT, 2018.

[28] A. J. Sorensen, "A survey of dynamic positioning control systems," *Annual Reviews in Control*, vol. 35, no. 1, pp. 123–136, 2011.

[29] M. Breivik, S. Kvaal, and P. Østby, "From Eureka to K-Pos: Dynamic Positioning as a Highly Successful and Important Marine Control Technology," *IFAC-PapersOnLine*, vol. 48, no. 16, pp. 313–323, 2015.

[30] O. Cadet, "Introduction to Kalman Filter and its Use in Dynamic Positioning Systems Introduction to Kalman Filter-Application to DP Dynamic Positioning Conference," tech. rep., Transocean Offshore Deepwater Drilling Inc., 2003.

[31] A. Witbeck, "Dynamic Positioning.," Tech. Rep. September, TU Delft, 2008.

[32] Jumbo, "Manoeuvring Equipment DP," 2019.

[33] MARIN, "Theory Documentation," tech. rep., MARIN, 2000.

[34] A. J. Sorensen, S. I. Sagatun, and T. I. Fossen, "DESIGN OF A DYNAMIC POSITIONING SYSTEM USING MODEL-BASED CONTROL," Tech. Rep. 3, The Norwegian Institute of Technology, 1996.

[35] H. Cozijn and E. Frickel, "(DP) SOFTWARE DESIGN & CONTROL SESSION Past, Present and Future of Hydrodynamic Research for DP Applications," tech. rep., Maritime Research Institute Netherlands (MARIN), 2015.

[36] F. C. Bakker, "A conceptual solution to in-stable dynamic positioning during offshore heavy lift operations Using computer simulation techniques," tech. rep., TU Delft, 2015.

[37] P. A. Figueiredo and F. M. Brójo, "Parametric study of multicomponent mooring lines at catenary form in terms of anchoring cost," *Energy Procedia*, vol. 136, pp. 456–462, 2017.

[38] Y. A. Hermawan and Y. Furukawa, "Coupled three-dimensional dynamics model of multi-component mooring line for motion analysis of floating offshore structure," *Ocean Engineering*, vol. 200, p. 106928, 2020.

[39] Y. Dalgic, I. Lazakis, and O. Turan, "Vessel charter rate estimation for offshore wind O&M activities," *Developments in Maritime Transportation and Exploitation of Sea Resources*, pp. 899–908, 2013.

[40] P. Naaijen, "course_notes_2020_2021 Motions and loadings," tech. rep., TU Delft, 2020.

[41] D. P. Wellens, "Floating stability Free surfaces in tanks," tech. rep., TU Delft, Delft, 2020.

[42] S. Uharek and M. S. Berlin, "Modelling of a crane vessel on dynamic positioning and assessment of its operational capability," tech. rep., Technische Universität Berlin, 2018.

[43] DNV GL, "DNVGL-ST-0111: Assessment of station keeping capability of dynamic positioning vessels," Tech. Rep. July, DNVGL, 2018.

[44] A. J. Häusler, A. Saccon, J. Hauser, A. M. Pascoal, and A. P. Aguiar, *Four-quadrant propeller modeling: A low-order harmonic approximation.* IFAC, 2013.

[45] W. Zhao, M. Efthymiou, F. McPhail, and S. Wille, "Nonlinear roll damping of a barge with and without liquid cargo in spherical tanks," *Journal of Ocean Engineering and Science*, vol. 1, no. 1, pp. 84–91, 2016.

[46] P. Sliggers, "Climate In this lecture we will focus only on wind , waves and current," 2019.

[47] J. Babicz, *Encyclopedia of Encyclopedia of.* WÄRTSILÄ CORPORATION, 1950.

[48] P. Naaijen, *Deterministic Prediction of Waves and Wave Induced Vessel Motions.* PhD thesis, TUDelft, 2017.

[49] O. M. Faltinsen, *Sea Loads on Ships and Offshore Structures Cambridge Ocean Technology Series Cambridge University Press 1993.* Cambridge University Press, 1990.

Glossary

List of Acronyms

TU Delft	Delft University of Technology
PID	Proportional Integral Derivative
PD	Proportional Derivative
TWD	Temporarily Work Design
ILT	Internal Lifting Tool
RAO	Response Amplitude Operator
DP	Dynamic Positioning
GPS	Global Positioning System
DGPS	Differential Global Positioning System
HPR	Hydro acoustic Position Reference
QTF	Quadratic transfer functions
JONSWAP	Joint Northsea Wave Project
UNFCCC	United Nations Framework Convention on Climate Change
RK2	Runge-Kutta2
GMt	Transverse metacentric height
RPM	Rounds Per Minute
MARIN	Maritiem Research Instituut Nederland
CoG	Centre of Gravity
KC	Keulegan-Carpenter
DoF	Degrees of Freedom